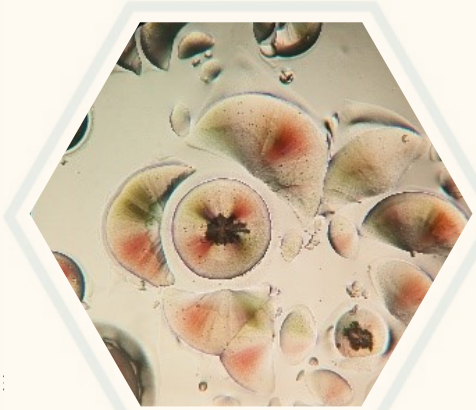
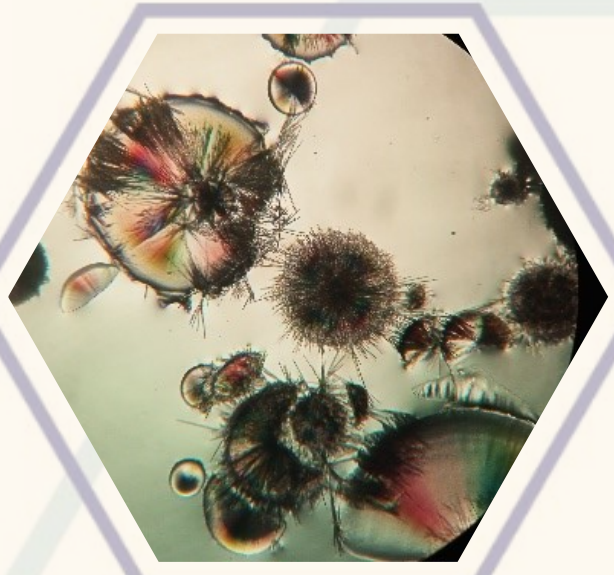
Vol 9, No 1, 2023

Journal of Biomedical Photonics & Engineering





Editor-in-Chief:
Valery Tuchin

©2023 J-BPE

Journal of Biomedical Photonics & Engineering

by Samara National Research University

Volume 9, Issue 1 (March 2023)

Editor-In-Chief

Valery V. Tuchin - Saratov National Research State University, Russian Federation;
Institute of Precision Mechanics and Control RAS, Russian Federation; a corr.-member of RAS

Deputy Editor-In-Chief

Valery P. Zakharov - Samara National Research University, Russian Federation

Postal address:
39B Lukacheva st., room #301
Samara 443086, Russian Federation

Used Figures from this issue on the Cover

Anna B. Shipovskaya et al. Features of L-Menthol Crystallization in Optically Active Medium Based on L- and D-Asparaginate Chitosan, 010305, Table 1.

© 2023 J-BPE

Contents

Articles

Optical Properties of Perfused Rat Liver Tissues 010301
Ksenia Kandurova, Alexander Palalov, Evgeniya Seryogina, Viktor Dremin, Andrey Dunaev, and Elena Potapova

Simulation of the First and the Second Waves of COVID-19 Spreading in Russian Federation Regions Using an Agent-Based Model 010302
Mikhail Kirillin, Aleksandr Khilov, Valeriya Perekatova, Ekaterina Sergeeva, Daria Kurakina, Ilya Fiks, Nikolay Saperkin, Ming Tang, Yong Zou, Elbert Macau, and Efim Pelinovsky

Concentration Dependence of Optical Transmission and Extinction of Different Diatom Cultures 010303
Julijana Cvjetinovic, Sergei Perkov, Maxim Kurochkin, Igor Sergeev, Sergei German, Yekaterina Bedoshvili, Nickolai Davidovich, Alexander Korsunsky, and Dmitry Gorin

Inhibition of Self-Assembling Peptide Fibrils Formation Using Thioflavin T as a Photosensitizer 010304
Tatiana N. Tikhonova, Anna A. Rubekina, Viktor A. Vorobev, Ekaterina A. Mefodeva, Eugene G. Maksimov, Yuri M. Efremov, Maxim E. Darvin, Peter S. Timashev, Peter V. Gorelkin, Alexander S. Erofeev, Nikolay N. Sysoev, and Evgeny A. Shirshin

Features of L-Menthol Crystallization in Optically Active Medium Based on L- and D-Asparaginate Chitosan 010305
Anna B. Shipovskaya, Natalia O. Gegel, and Xenia M. Shipenok

Multicentral Agent-Based Model of Four Waves of COVID-19 Spreading in Nizhny Novgorod Region of Russian Federation 010306
Mikhail Kirillin, Aleksandr Khilov, Valeriya Perekatova, Ekaterina Sergeeva, Daria Kurakina, Ilya Fiks, Nikolay Saperkin, Ming Tang, Yong Zou, Elbert Macau, and Efim Pelinovsky

Intraoperative Optical Diagnostics of Uterine Microcirculation during Myomectomy 010307
Elena Potapova, Nikolai Polenov, Karina Zakuraeva, Valentina Krutikova, Maria Yarmolinskaya, and Igor Kogan

Highly Stable 11-MUA Capped Gold Nanobipyramid for Refractive Index Sensing 010308
Prajna N. Deviprasada, and Rajeev K. Sinha

The Effect of Photobiostimulation by Light Waves in the Blue Range of the Spectrum on Microcirculation Parameters and the Activity of Oxidative Homeostasis Enzymes in the Skin 010309
Vadim V. Astashov, Valentin I. Kozlov, Vladimir A. Duvanskiy, Pavel V. Novokreshchenov, and Ilya M. Pushkar

 © 2023 J-BPE

Optical Properties of Perfused Rat Liver Tissues

Ksenia Kandurova, Alexander Palalov, Evgeniya Seryogina, Viktor Dremin, Andrey Dunaev, and Elena Potapova

Research and Development Center of Biomedical Photonics, Orel State University, 95 Komsomolskaya str., Orel 302026, Russia

*** e-mail:** kandkseniya@gmail.com

Abstract. In this work, we demonstrate the results of measuring the optical properties of rat liver tissue slices after the liver itself underwent the perfusion procedure with an isotonic solution. The approach is suggested as a means to attenuate the influence of blood absorption on recorded characteristics and demonstrates its effectiveness in changing the composition of recorded spectra in the visible range. The data obtained seem promising to be used to upgrade the proposed methodology and apply the results for the diagnosis and modeling of light-tissue interaction in liver under healthy and pathological conditions.
© 2022 Journal of Biomedical Photonics & Engineering.

Keywords: liver; perfusion; optical properties; spectrophotometry.

Paper #3561 received 28 Oct 2022; revised manuscript received 29 Nov 2022; accepted for publication 30 Nov 2022; published online 9 Dec 2022. doi: 10.18287/JBPE23.09.010301.

1 Introduction

Optical diagnostic methods remain a promising area of biotechnical research and continue to improve to find new applications in medicine [1–3], including surgery [4–8]. In turn, surgery tends to widely introduce less radical surgical procedures. This trend requires the development of technologies for an objective assessment of the functional state of organ tissues right in the course of surgery. A wide range of continuously evolving spectroscopy and imaging techniques based on various phenomena of light-tissue interaction can be used to obtain real-time diagnostic information [9, 10]. Research aimed at combining new optical methods with standard surgical equipment is of special relevance at present [11–14].

Developing and calibrating new optical diagnostic methods requires knowledge of tissue optical properties (absorption and scattering coefficients, anisotropy factor, refractive index, etc.). To date, many data have been accumulated on the optical characteristics of various tissues [15, 16] (e.g. skin and muscles [17, 18], liver [19, 20], pancreas [21], bones [22], blood [23], brain [24]), including pathological ones [25, 26].

A number of clinical studies in hepatology use liver optical properties to develop approaches for optimizing the treatment [27, 28] or for differentiating between healthy and tumor tissues [4, 29]. However, the fact that the liver is an organ with a high blood supply is not taken into account [20], and therefore it would be important to exclude or reduce the excessive influence of one of the strongest optical absorbers, blood, in some regions of the optical spectrum. Hemoglobin and its derivatives are chromophores that significantly absorb optical radiation in the visible range, affecting the results of measurements by various methods, including those based on excitation and registration of endogenous fluorescence spectra [30, 31].

To reduce the influence of the strong absorption properties of blood hemoglobin on the measured optical characteristics of the liver, it is possible to use a perfusion procedure to remove blood from the blood vessels of the liver using, for example, an isotonic solution (0.9% NaCl).

Organ perfusion is used in biomedical research for several purposes: as a model to study the effects of ischemia and reperfusion in transplantology [32], for preliminary preparation of the liver parenchyma before hepatocyte isolation [33–35], and for obtaining biomatrixes in tissue engineering [36].

Thus, the aim of this work was to measure the optical characteristics of the rat liver using the approach to reduce blood volume by perfusing the organ before preparing the acute slices used for spectrophotometric measurements.

2 Methods and Materials

The studies were approved by the Ethics Committee of Orel State University named after I. S. Turgenev (protocol No. 188 of 21.02.2020) and were carried out in accordance with the principles of Good Laboratory Practice [37].

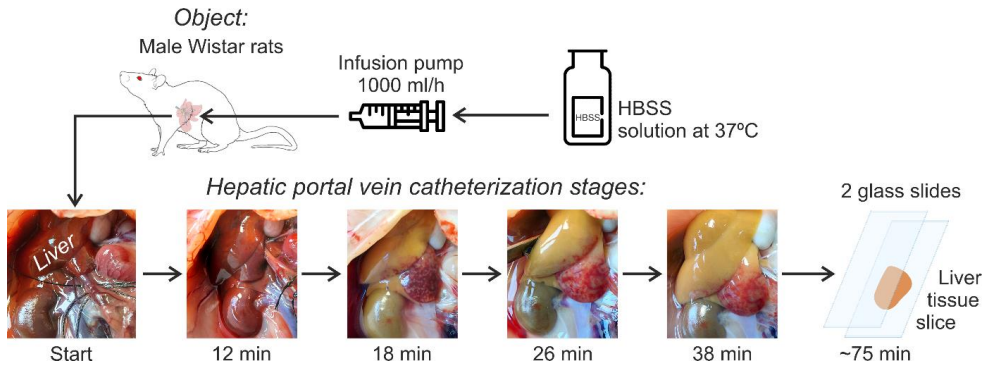


Fig. 1 Schematic of the rat liver perfusion procedure used to prepare tissue samples for optical measurements with an approximate time frame for observations of changes in the liver tissue.

In the study, male Wistar rats (n = 3 per experimental group and n = 3 per control group, age – 3 months, weight – 220–250 g) were used. The experimental studies included two stages: liver perfusion in laboratory animals to obtain liver tissue samples and following spectrophotometric measurements. To assess the efficiency of the perfusion procedure, the optical characteristics obtained were compared with those of the control group of rats, which were measured in fresh slices.

The perfusion procedure was performed under anesthesia. Zoletil 100 (Vibrac, France) and Xyla (Interchemie, The Netherlands) in standard doses were used to anesthetize the animal. The rat was fixed on a special platform in the supine position with a gauze holder. After the onset of deep anesthesia, a layer-by-layer dissection of the anterior abdominal wall along the median line was performed to provide access to the abdominal cavity. The portal vein of the liver was then isolated from the connective tissue space using soft forceps and isolated from the rest of the tissues. Ligatures were placed under the portal vein, one of them prevented blood flow. Subsequently, a vascular catheter (22 G) pre-filled with heparin solution (5000 i.u./ml) was inserted into the vein via a guide. The catheter was fixated with the remaining ligatures and connected by flexible tubes to an infusion system. Hank's Balanced Salt Solution (HBSS), pH=7.4, 37 °C, was injected into the vessel. The inferior vena cava was perforated to ensure fluid outflow. The flow rate of the solution was 1000 ml/h, the total volume of the solution was about 1.5–2.0 l. The important part of the procedure was to keep the rat's heart working, which accelerated the withdrawal of blood from the liver vessels. In some cases, rapid liver perfusion was performed to eliminate probable stasis in small vessels.

During perfusion (Fig. 1), there was a change in the color of the liver from red-brown to yellow-gray and the vascular pattern became visible on the surface of the organ. The degree of perfusion sufficient for optical measurements was determined by the color of the liver and the intensity of HBSS solution staining with blood washed out. At the end of the procedure, the catheter was carefully disconnected and the animal was removed from the experiment by euthanasia. The liver was isolated from the abdominal cavity and placed in a Petri dish with HBSS solution. The liver slices were made by hand and their thickness (0.9–1.0 mm) was calculated by taking into account the thickness of the glass slides measured by a micrometer MK 0–25 (measuring range 0–25 mm, measuring error 4 μm).

The obtained tissue slices (N = 8 samples in the study group and N = 11 in the control group) were placed between two standard 1-mm silicate glass slides. A fixed distance of 0.95 mm between the glasses was maintained. A Shimadzu UV-2600 dual-beam spectrophotometer (Shimadzu Corporation, Japan) with an ISR-2600Plus integrating sphere module was used to measure the characteristics of tissue samples. The sphere has a diameter of 60 mm with two detectors (photomultiplier and InGaAs detector) and allows recording spectra in the range of 220–1400 nm with a step of 1 nm. The arrangement of the samples relative to the sphere ports (S side – sample side and R side – reference side) is shown in Fig. 2.

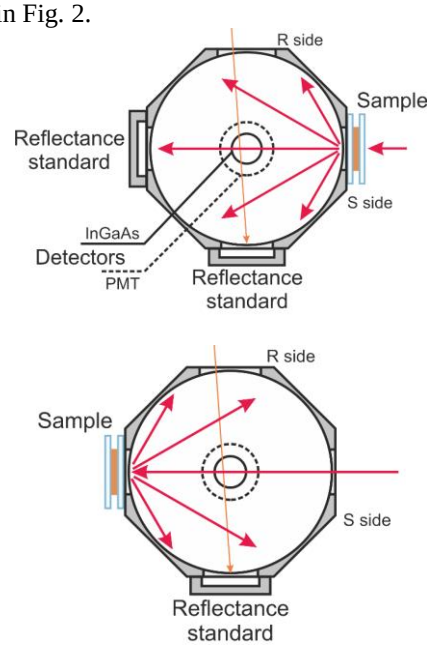


Fig. 2 Schematic of measurements of the optical characteristics of liver tissue samples using an integrating sphere with a double-beam system: (a) total transmittance T_t, (b) total reflectance R_t.

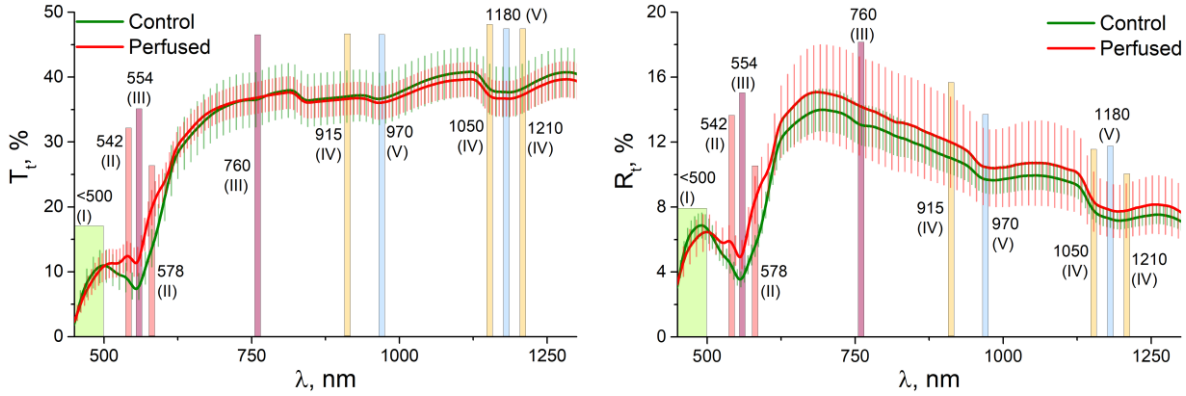


Fig. 3 Average (mean ± standard deviation) spectra of total transmittance T_t (a) and total reflection R_t (b) of rat liver tissue samples subjected (red line) and not subjected (green line) to the perfusion procedure along with typical wavelengths of light absorption by the main chromophores.

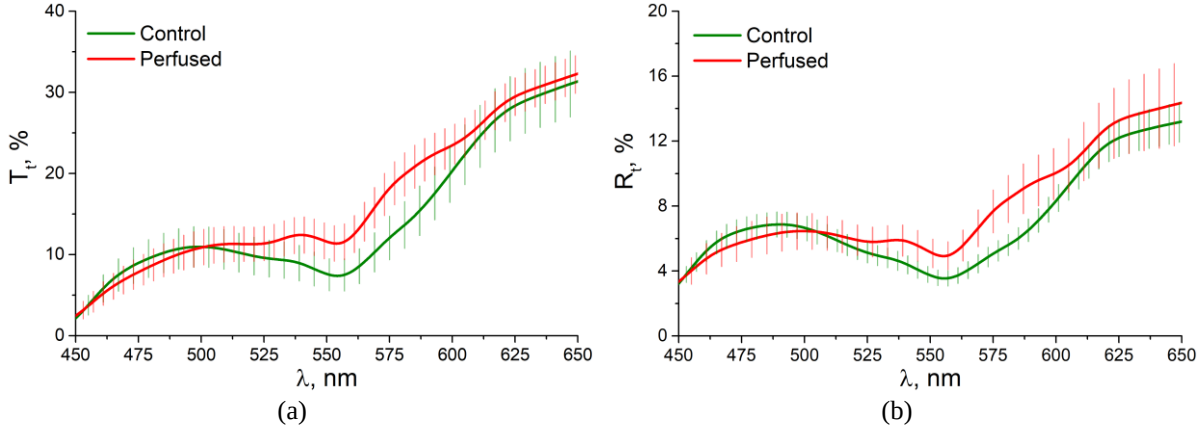


Fig. 4 Average (mean ± standard deviation) spectra of total transmittance T_t (a) and total reflection R_t (b) of rat liver tissue samples subjected (red line) and not subjected (green line) to the perfusion procedure: comparison of results in the 450–650 nm range.

The absorption coefficient μ_a and the reduced scattering coefficient μ_s' were calculated by the inverse adding-doubling method using the algorithm developed and described by S. Prahl [38]. For calculations, the value of the anisotropy factor g was assumed to be 0.7 according to data from the literature for liver tissue [4, 20, 39]. The algorithm used considers the interaction of radiation with the sample sandwiched between the slides. Thus, the calculation takes into account the specular reflectance from the air, glass and tissue borders.

3 Results and Discussion

The results of the spectral measurements obtained for all samples were averaged. Fig. 3 shows the mean and standard deviation of the total transmittance and reflectance values of the obtained rat liver tissue samples.

The spectra show an increase in total transmittance and reflectance with increasing wavelength, as well as a slight decrease in the 500–600 nm range. Regarding the visible range, the observed picture is mainly due to the presence of bilirubin pigment in the tissue (spectral range with the characteristic wavelength of light absorption is marked in Fig. 3 by number I (hereinafter the same for other chromophores)) – one of the main components of bile produced by hepatocytes [40–42] – as well as two forms of blood protein hemoglobin – oxygen-bound oxyhemoglobin (II) and unbound deoxyhemoglobin (III) [23, 40, 43]. In the near-infrared (NIR) region, the spectral profile of liver tissue is largely determined by the intersection of the lipid (IV) and water (V) absorption bands [43–45].

Highly oxygenated blood has two distinctive peaks in the absorption spectrum at 415 nm (Soret band) and at 542 and 578 nm (Q-bands); deoxygenated blood has these peaks at 425, 554 and 760 nm [46]. In the 500–600 nm range, all recorded spectra had a similar characteristic decrease in reflectance and transmittance due to the presence of hemoglobin. The analysis of the data obtained (Fig. 4) revealed that the liver slices of the control group had a typical absorption peak only at a

wavelength of 554 nm. There was also a characteristic decrease in transmittance and reflectance in the deoxyhemoglobin absorption band at 760 nm. The specific characteristic of the liver blood supply is the increase in venous blood content [47], which causes a higher intensity of light absorption by deoxyhemoglobin.

After perfusion was performed, the oxyhemoglobin absorption became dominant in liver slices, though there was a 15–20 nm blue-shift of this part of the spectrum. This can be caused by the influence of the spectral characteristics of bile, which has local absorption maxima at wavelengths of 409 and 605 nm. At the same time, the second absorption maximum of bile becomes well manifested in the spectrum of perfused liver tissue (Fig. 4).

Therefore, despite the performed perfusion and the visual control of the liver parenchyma during the procedure, a portion of the blood remained in the small vessels, but had a noticeably smaller effect on the results of the spectral characteristics study.

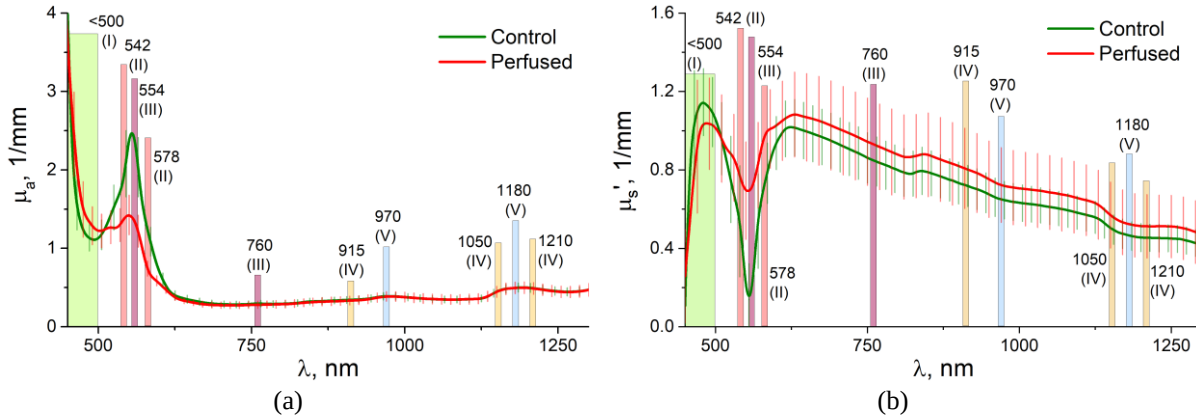
After perfusion, the total transmittance values slightly decreased in the NIR range, while the total reflectance increased. There were no changes in the shape of the spectra, which may indicate quantitative rather than qualitative changes that were observed in the oxy- and deoxyhemoglobin absorption ranges. The HBSS solution is aqueous, which played a role in these studies when it was used to displace blood in liver vessels. As stated above, the NIR range is informative for assessing changes in the water and lipid content. According to the presented results, there is a characteristic decrease at wavelengths around 970 and 1180–1190 nm in the perfused tissues due to water absorption [44, 48, 49].

Fig. 5 shows graphs of the calculated dependences of the absorption and scattering coefficients as a function of wavelength. The absorption coefficient showed greater reproducibility (less standard deviation) compared to the scattering coefficient and the expected ratios of values in the bands of different main chromophores [4, 20, 49, 50]. The values remained almost unchanged in the NIR range, while there was a twofold decrease at the band of 540–560 nm as a result of the perfusion procedure.

The results of the calculation of the reduced scattering coefficient dependence clearly demonstrate the intended effect of the proposed approach for wavelengths below 600 nm. Due to the high blood content and, therefore, the low values of total transmittance and reflectance within the hemoglobin absorption bands, the calculated scattering coefficient has critically low values, which are not observed after liver perfusion. In general, the dependence of the reduced scattering coefficient was as expected – it decreased when the wavelength increased [19, 20, 39].

The following limitations of the experimental study should be noted. Control of the perfusion level was provided only by visual inspection. Despite attempts to standardize the procedure (minimum volume of pumped liquid, perfusion rate, etc.), its result was determined, among other things, by individual peculiarities of the object (anatomy and viability of the rat). The liver slices were taken by the same lab technician, but manually according to a specially developed technique, which affects their thickness and area. Furthermore, the irregular structure of the biological tissue and the methodological difficulties of fixing the slices between the glass slides may have influenced the results of the study.

Thus, the proposed approach for preliminary perfusion of liver tissues to reduce the influence of blood on the optical characteristics of the liver demonstrated its effectiveness, which allowed it to significantly reduce the influence of oxy- and deoxyhemoglobin on spectra recording results.



(a) (b)

Fig. 5 Average dependences (mean ± standard deviation) of calculated absorption μ_a (a) and reduced scattering coefficient μ_s' (b) of rat liver tissue samples subjected (red line) and not subjected (green line) to the perfusion procedure along with typical wavelengths of light absorption by the main chromophores.

4 Conclusion

Currently, an important step in the development of biomedical optics is the transition from theoretical and preclinical research to the practical implementation of technologies in clinical practice. Adequate and effective application of optical methods in diagnostics, surgery and therapy requires reliable data on the optical properties of human tissues, including the liver. In this work, we considered, in particular, acquisition of optical properties of liver tissue along with the decreasing influence of optical characteristics of blood. This can be of importance when modeling spectral characteristics of the liver in diseases such as steatosis, cirrhosis, cancer, etc. The results presented in the work have shown that the preliminary perfusion of the liver allows one to reduce the influence of hemoglobin on the recorded and calculated optical parameters.

Disclosures

The authors declare no conflict of interest.

Acknowledgements

The authors acknowledge the support of the Russian Science Foundation under project No. 21-15-00325.

References

1. J. A. Kim, D. J. Wales, and G.-Z. Yang, "Optical spectroscopy for in vivo medical diagnosis—a review of the state of the art and future perspectives," Progress in Biomedical Engineering 2(4), 42001 (2020).
2. A. B. Shrirao, R. S. Schloss, Z. Fritz, M. V. Shrirao, R. Rosen, and M. L. Yarmush, "Autofluorescence of blood and its application in biomedical and clinical research," Biotechnology and Bioengineering 118(12), 4550–4576 (2021).
3. Z. He, P. Wang, and X. Ye, "Novel endoscopic optical diagnostic technologies in medical trial research: recent advancements and future prospects," BioMedical Engineering OnLine 20(1), 5 (2021).
4. V. Dremin, E. Potapova, E. Zherebtsov, K. Kandurova, V. Shupletsov, A. Alekseyev, A. Mamoshin, and A. Dunaev, "Optical percutaneous needle biopsy of the liver: A pilot animal and clinical study," Scientific Reports 10(1), 14200 (2020).
5. E. A. Zherebtsov, E. V. Potapova, A. V. Mamoshin, V. V. Shupletsov, K. Y. Kandurova, V. V. Dremin, A. Y. Abramov, and A. V. Dunaev, "Fluorescence lifetime needle optical biopsy discriminates hepatocellular carcinoma," Biomedical Optics Express 13(2), 633–646 (2022).
6. R. Alfano, Y. Pu, "Optical biopsy for cancer detection," Chapter 11 in Lasers for Medical Applications, H. Jelínková (ed.), Woodhead Publishing Limited, Cambridge, 325–367 (2013).
7. K. Kandurova, V. Dremin, E. Zherebtsov, E. Potapova, A. Alyanov, A. Mamoshin, Y. Ivanov, A. Borsukov, and A. Dunaev, "Fiber-Optic System for Intraoperative Study of Abdominal Organs during Minimally Invasive Surgical Interventions," Applied Sciences 9(2), 217 (2019).
8. E. Potapova, V. Dremin, E. Zherebtsov, A. Mamoshin, and A. Dunaev, "Multimodal Optical Diagnostic in Minimally Invasive Surgery," Chapter 11 in Multimodal Optical Diagnostics of Cancer, V. V. Tuchin, J. Popp, and V. Zakharov (eds.), Springer, Cham, Switzerland, 397–424 (2020).
9. V. V. Tuchin (ed.), Handbook of Optical Biomedical Diagnostics, vol. 1: Light-Tissue Interaction, 2nd ed., SPIE Press, Bellingham, USA (2016). ISBN: 9781628419092.
10. A. C. Croce, G. Bottiroli, "Autofluorescence spectroscopy and imaging: A tool for biomedical research and diagnosis," European Journal of Histochemistry 58(4), 320–337 (2014).
11. J. W. Spliethoff, L. L. de Boer, M. A. J. Meier, W. Prevoo, J. de Jong, K. Kuhlmann, T. M. Bydlon, H. J. C. M. Sterenborg, B. H. W. Hendriks, and T. J. M. Ruers, "In vivo characterization of colorectal metastases in human liver using diffuse reflectance spectroscopy: Toward guidance in oncological procedures," Journal of Biomedical Optics 21(9), 097004 (2016).
12. A. Litvinenko, M. Garazdyuk, V. Bachinsky, O. Vanchulyak, A. Ushenko, Yu. Ushenko, A. Dubolazov, P. Gorodensky, O. Yatsko, B. Lin, and Z. Chen, "Multiparametric polarization histology in the detection of traumatic changes in the optical anisotropy of biological tissues," Proceedings of SPIE 11510, 115102O (2020).
13. F. Braun, R. Schalk, M. Nachtmann, A. Hien, R. Frank, T. Beuermann, F.-J. Methner, B. Kränzlin, M. Rädle and N. Gretz, "A customized multispectral needle probe combined with a virtual photometric setup for in vivo detection of Lewis lung carcinoma in an animal model," Measurement Science and Technology 30(10), 104001 (2019).
14. E. V. Potapova, E. S. Seryogina, V. V. Dremin, D. D. Stavtsev, I. O. Kozlov, E. A. Zherebtsov, A. V. Mamoshin, Yu. V. Ivanov, and A. V. Dunaev, "Laser speckle contrast imaging of blood microcirculation in pancreatic tissues during laparoscopic interventions," Quantum Electronics 50(1), 33–40 (2020).
15. S. L. Jacques, "Optical properties of biological tissues: a review," Physics in Medicine & Biology 58(11), R37 (2013).
16. M. Mesradi, A. Genoux, V. Cuplov, D. Abi-Haidar, S. Jan, I. Buvat, and F. Pain, "Experimental and analytical comparative study of optical coefficient of fresh and frozen rat tissues," Journal of Biomedical Optics 18(11), 117010 (2013).

17. A. N. Bashkatov, E. A. Genina, and V. V. Tuchin, "Optical properties of skin, subcutaneous, and muscle tissues: a review," Journal of Innovative Optical Health Sciences 4(01), 9–38 (2011).
18. T. Lister, P. A. Wright, and P. H. Chappell, "Optical properties of human skin," Journal of Biomedical Optics 17(9), 090901 (2012).
19. J. Ritz, A. Roggan, C. Isbert, G. Müller, H. J. Buhr, and C.-T. Germer, "Optical properties of native and coagulated porcine liver tissue between 400 and 2400 nm," Lasers in Surgery and Medicine: The Official Journal of the American Society for Laser Medicine and Surgery 29(3), 205–212 (2001).
20. I. Carneiro, S. Carvalho, R. Henrique, L. Oliveira, and V. V. Tuchin, "Measuring optical properties of human liver between 400 and 1000 nm," Quantum Electronics 49(1), 13 (2019).
21. P. Lanka, L. Bianchi, A. Farina, M. De Landro, A. Pifferi, and P. Saccomandi, "Estimation of porcine pancreas optical properties in the 600–1100 nm wavelength range for light-based therapies," Scientific Reports 12(1), 14300 (2022).
22. H. Soleimanzad, H. Gurden, and F. Pain, "Optical properties of mice skull bone in the 455-to 705-nm range," Journal of Biomedical Optics 22(1), 010503 (2017).
23. N. Bosschaart, G. J. Edelman, M. C. G. Aalders, T. G. van Leeuwen, and D. J. Faber, "A literature review and novel theoretical approach on the optical properties of whole blood," Lasers in Medical Science 29(2), 453–479 (2014).
24. A. S. Shanshool, E. N. Lazareva, O. Hamdy, and V. V. Tuchin, "Optical Properties and Fluence Distribution in Rabbit Head Tissues at Selected Laser Wavelengths," Materials 15(16), 5696 (2022).
25. E. V. Salomatina, B. Jiang, J. Novak, and A. N. Yaroslavsky, "Optical properties of normal and cancerous human skin in the visible and near-infrared spectral range," Journal of Biomedical Optic 11(6), 064026 (2006).
26. A. N. Bashkatov, Br. Jiang, J. Novak, and A. N. Yaroslavsky, "Measurement of tissue optical properties in the context of tissue optical clearing," Journal of Biomedical Optics 23(9), 91416 (2018).
27. M. S. Enevoldsen, O. Skovgaard, and P. E. Andersen, "A combined mathematical-physical model of laser-induced thermotherapy (LITT)," in European Conference on Biomedical Optics, Optica Publishing Group, 7373_15 (2009).
28. C. Germer, A. Roggan, J. P. Ritz, C. Isbert, D. Albrecht, G. Müller, and H. J. Buhr, "Optical properties of native and coagulated human liver tissue and liver metastases in the near infrared range," Lasers in Surgery and Medicine: The Official Journal of the American Society for Laser Medicine and Surgery 23(4), 194–203 (1998).
29. R. Nachabé, D. J. Evers, B. H. W. Hendriks, G. W. Lucassen, M. van der Voort, J. Wesseling, and T. J. M. Ruers, "Effect of bile absorption coefficients on the estimation of liver tissue optical properties and related implications in discriminating healthy and tumorous samples," Biomedical Optics Express 2(3), 600–614 (2011).
30. E. A. Zherebtsov, K. Y. Kandurova, E. S. Seryogina, I. O. Kozlov, V. V. Dremin, A. I. Zherebtsova, A. V. Dunaev, and I. Meglinski, "The influence of local pressure on evaluation parameters of skin blood perfusion and fluorescence," Proceedings of SPIE 10336, 1033608 (2017).
31. V. V. Dremin, E. A. Zherebtsov, I. E. Rafailov, A. Y. Vinokurov, I. N. Novikova, A. I. Zherebtsova, K. S. Litvinova, and A. V. Dunaev, "The development of attenuation compensation models of fluorescence spectroscopy signals," Proceedings of SPIE 9917, 99170Y (2016).
32. M. Bessems, N. A. 't Hart, R. Tolba, B. M. Doorschodt, H. G. D. Leuvenink, R. J. Ploeg, T. Minor, and T. M. van Gulik, "The isolated perfused rat liver: standardization of a time-honoured model," Laboratory Animals 40(3), 236–246 (2006).
33. J. Aiken, L. Cima, B. Schloo, D. Mooney, L. Johnson, R. Langer, and J. P.Vacanti, "Studies in rat liver perfusion for optimal harvest of hepatocytes," Journal of Pediatric Surgery 25(1), 140–145 (1990).
34. M. Shulman, Y. Nahmias, "Long-term culture and coculture of primary rat and human hepatocytes," Chapter 17 in Epithelial Cell Culture Protocols, S. H. Randell, M. L. Fulcher (eds.), Humana Press, Totowa, USA, 287–302 (2012).
35. R. I. Freshney (ed.), Culture of Animal Cells: A Manual of Basic Technique and Specialized Applications, 7th ed., John Wiley & Sons, Hoboken, USA (2015). ISBN: 978-1-118-87364-9.
36. M. X. Pan, P. Y. Hu, Y. Cheng, L. Q. Cai, X. H. Rao, Y. Wang, and Y. Gao, "An efficient method for decellularization of the rat liver," Journal of the Formosan Medical Association 113(10), 680–687 (2014).
37. OECD Principles of Good Laboratory Practice, Council of the Organisation for Economic Co-operation and Development, Paris, 1998 (accessed 17 October 2022). [https://www.oecd.org/officialdocuments/publicdisplaydocumentpdf/?cote=env/mc/chem(98)17&doclanguage=en].
38. S. A. Prahl, M. J. C. van Gemert, and A. J. Welch, "Determining the optical properties of turbid media by using the adding–doubling method," Applied Optics 32(4), 559–568 (1993).
39. P. Parsa, S. L. Jacques, and N. S. Nishioka, "Optical properties of rat liver between 350 and 2200 nm," Applied Optics 28(12), 2325–2330 (1989).
40. D. J. Maitland, J. T. Walsh, and J. B. Prystowsky, "Optical properties of human gallbladder tissue and bile," Applied Optics 32(4), 586–591 (1993).
41. F. Baldini, P. Bechi, F. Cianchi, A. Falai, C. Fiorillo, and P. Nassi, "Analysis of the optical properties of bile," Journal of Biomedical Optics 5(3), 321–329 (2000).
42. A. C. Croce, A. Ferrigno, G. Santin, M. Vairetti, and G. Bottiroli, "Bilirubin: an autofluorescence bile biomarker for liver functionality monitoring," Journal of Biophotonics 7(10), 810–817 (2014).

43. S. A. Filatova, I. A. Shcherbakov, and V. B. Tsvetkov, "Optical properties of animal tissues in the wavelength range from 350 to 2600 nm," Journal of Biomedical Optics 22(3), 35009 (2017).
44. C.-L. Tsai, J.-C. Chen, and W.-J. Wang, "Near-infrared absorption property of biological soft tissue constituents," Journal of Medical and Biological Engineering 21(1), 7–14 (2001).
45. R. R. Anderson, W. Farinelli, H. Laubach, D. Manstein, A. N. Yaroslavsky, J. Gubeli III, K. Jordan, G. R. Neil, M. Shinn, W. Chandler, G. P. Williams, S. V. Benson, D. R. Douglas, and H. F. Dylla, "Selective photothermolysis of lipid-rich tissues: A free electron laser study," Lasers in Surgery and Medicine: The Official Journal of the American Society for Laser Medicine and Surgery 38(10), 913–919 (2006).
46. V. V. Tuchin (ed.), Tissue Optics: Light Scattering Methods and Instruments for Medical Diagnostics, 3rd ed., SPIE Press, Bellingham, USA (2015). ISBN: 9781628415179.
47. G. Naulaers, B. Meyns, M. Miserez, V. Leunens, S. Van Huffel, P. Casaer, and H. Devlieger, "Measurement of the liver tissue oxygenation by near-infrared spectroscopy," Intensive Care Medicine 31(1), 138–141 (2005).
48. J. A. Curcio, C. C. Petty, "The near infrared absorption spectrum of liquid water," Journal of the Optical Society of America 41(5), 302–304 (1951).
49. A. N. Bashkatov, E. A. Genina, V. I. Kochubey, and V. V. Tuchin, "Optical properties of human skin, subcutaneous and mucous tissues in the wavelength range from 400 to 2000 nm," Journal of Physics D: Applied Physics 38(15), 2543 (2005).
50. J. L. Sandell, T. C. Zhu, "A review of in-vivo optical properties of human tissues and its impact on PDT," Journal of Biophotonics 4(11–12), 773–787 (2011).

Simulation of the First and the Second Waves of COVID-19 Spreading in Russian Federation Regions Using an Agent-Based Model

Mikhail Kirillin[1*], Aleksandr Khilov[1+], Valeriya Perekatova[1], Ekaterina Sergeeva[1], Daria Kurakina[1], Ilya Fiks[1], Nikolay Saperkin[1,2], Ming Tang[3], Yong Zou[3], Elbert Macau[4], and Efim Pelinovsky[1,5]

[1] Institute of Applied Physics RAS, 46 Ul'yanov str., Nizhny Novgorod 603950, Russia

[2] Privolzhsky Research Medical University, 10/1, Minin and Pozharsky Sq., Nizhny Novgorod 603950, Russia

[3] School of Physics and Electronic Science, East China Normal University, 3663 N. Zhongshan Rd., Shanghai 200062, China

[4] Instituto de Ciências e Tecnologia, Universidade Federal de São Paulo, R. Sena Madureira, 1500 – Vila Clementino, São Paulo 04021-001, Brasil

[5] National Research University – Higher School of Economics, 25/12 Bolshaya Pecherskaya str., Nizhny Novgorod 603155, Russia

e-mail: *mkirillin@yandex.ru, +alhil@inbox.ru

Abstract. The COVID-19 pandemics remains one of the largest global challenges. Necessity of effective systemic aids for the minimization of losses leads to the requirement of adequate models allowing to predict the impact of different factors on the spread of the disease. Agent-based simulation models provide a suitable solution with the possibility to accurately account for such factors as age structure of a population, characteristics of isolation, self-isolation strategies and testing strategies, presence of super-spreaders etc. In this paper we report on the results of simulating the spread of COVID-19 in several representative regions of Russia using an agent-based model with a general pool combined with the simulation of population testing strategy. The model accounts for the following key epidemiologic characteristics: population age distribution, reproducibility rate, distributions of infectivity period, a period of clinical manifestation, and age-dependent probability of critical disease. It is demonstrated that the daily epidemiologic curves can be predicted well for different territories with the same model parameters, except for the initial number of infected agents and region-dependent testing as well as isolation strategies, which are considered to be tuning parameters of the model. The developed approach can be further expanded to other regions of different countries, while the determined model parameters could be used as starting values for such simulations. © 2023 Journal of Biomedical Photonics & Engineering.

Keywords: dynamics and control of epidemics; COVID-19; agent-based modeling.

Paper #3568 received 02 Dec 2022; revised manuscript received 21 Dec 2022; accepted for publication 21 Dec 2022; published online 13 Feb 2023. doi: 10.18287/JBPE23.09.010302.

1 Introduction

Prediction of further development of the COVID-19 pandemic and timely introduction of preventive measures require reliable tools for epidemic spread simulations. Several classes of models have been currently employed for forecasting the spread of infections. Even the simplest logistic model based on the first order ordinary differential equation has provided surprisingly reasonable accuracy in describing the first wave of COVID-19 in different countries [1–4]. Moreover,

employment of its predecessor, the Gompertz model, provides even better agreement of the predicted values with the official statistical data [5]. Regression models are known to provide us with rapid estimations of the spread of infections [6, 7]. Non-adaptive models allow obtaining the prognosis for any chosen period of time, however, they ignore local perturbations of epidemiologic characteristics, therefore they are not suitable for short-term prognosis. On the contrary, adaptive models are predominantly employed for short-term prognosis only. Autoregressive moving average models are applicable for short-term prognosis [8], while autoregressive integrated moving average model is applicable both for short-term and long-term prognosis [9]. Dynamic Bayesian networks are employed only for short-term prognosis and predominantly in the form of Markov models [10]. Neural networks and other machine learning based methods can be applied only for short-term prognosis. Furthermore, only feedforward neural networks and backpropagation algorithm can address the prognosis of infections spread [11].

Dynamic systems based on differential equations, which belong to a class of compartmental models, are employed for long-term prognosis. The pioneering work by Kermack and McKendrick [12] proposed SIR model, in which the population is divided into three groups – susceptible (*S*), infected (*I*), recovered (*R*) – and their interaction is described with non-linear differential equations. Modern compartmental models employ larger number of groups, accounting for exposed (*E*), hospitalized (*H*), critical (*C*), dead (*D*), and those in quarantine (*Q*) or isolation (*J*). Compartmental models are widely employed for the modeling of the spread of coronavirus infections (SARS, MERS, COVID-19). For example, SEIR (susceptible, exposed, infective, recovered) model has been applied for modeling of COVID-19 spread in African countries [13], Iran [14], Indonesia [15], Spain and Italy [16], India [17, 18]. The early COVID-19 spread and the efficacy of governmental measures are discussed in paper [19] also with regard to a SEIR model. Modified SEIR models may also account for vaccination process [18, 20]. Compartmental models are easy to construct, however, they do not capture random factors of the infections spreading nor individual characteristics of population members.

Individually-oriented models include so-called agent-based models, which can be applied both for short-term and long-term prognosis of the spread of infection. Every member of a population (referred to as an agent) is described by certain constant and variable characteristics, and the rules of interactions between the agents are determined. Agent-based models were proved to be effective in the description of the propagation of infections, such as Ebola virus disease [21] and influenza [22], regarding different sizes of population.

Agent-based models were also applied for the modeling of COVID-19 spread, for example, the modeling of the development and the regress of the infection in the various cities such as Helsinki [23], New York [24], and Singapore [25]. Certain agent-based models were based on previously developed models for the prediction of influenza pandemics, for example, the NotreDame-FRED model [26], the model of Ferguson's research group from Imperial College London [27], and the model for simulation of the COVID-19 pandemic in Australia [28].

A number of studies utilized agent-based models for assessing the impact of universal face mask wearing [29], digital contact tracking [30–32] and social distancing [32–34] as well as analyzing various intervention scenarios [24, 27, 32]. Other agent-based models were developed for modeling COVID-19 transmission in small communities such as a university [35], a supermarket [36], and a small town [37].

It is worth noting, that the validation strategy for a COVID-19 spread model should be based on the agreement with the official statistical data on daily new cases and daily deaths. These "measurement results" may have certain errors connected with the imperfection of the employed "measurement instrument", namely, a testing system. Building a model of a testing system is a particularly important task, since the simulated "measurement results" taken in consideration are actually the combined results of both the model of the disease spread and the model of testing system. Improper model of the testing system may result in incorrect results of the entire model, although the disease spread part can be valid. Moreover, this is the feedback system, since the test positive result affect the isolation strategy and, hence, further disease spread.

The aim of this paper is the development of an agent-based model capable of simulating the progress of the COVID-19 burst in different regions of the Russian Federation. Another important issue to be resolved in this study is the determination of the key model parameters that can provide the agreement of the simulated dynamics and actual statistics on daily new infection cases and deaths associated with COVID-19. The developed approach includes a testing strategy model based on official data concerning daily tests performed.

2 Materials and Methods

2.1 Agent-Based COVID-19 Spread Model

2.1.1 Single Agent States

The agent-based model operates on a set of elements $\mathfrak{N}$ where each element $a_n \in \mathfrak{N}$ is characterized by Boolean variables representing binary states α_n^j, where n is the element number, and j is the binary state. The elements are traditionally called agents and each of them represents a person in the considered population. The number of elements in $\mathfrak{N}$ usually attributed as cardinality $N = |\mathfrak{N}|$ is chosen in accordance with the population of the considered region. The agent-based model employed in this paper is a general pool model, which is schematically shown in Fig. 1. In the general pool model,

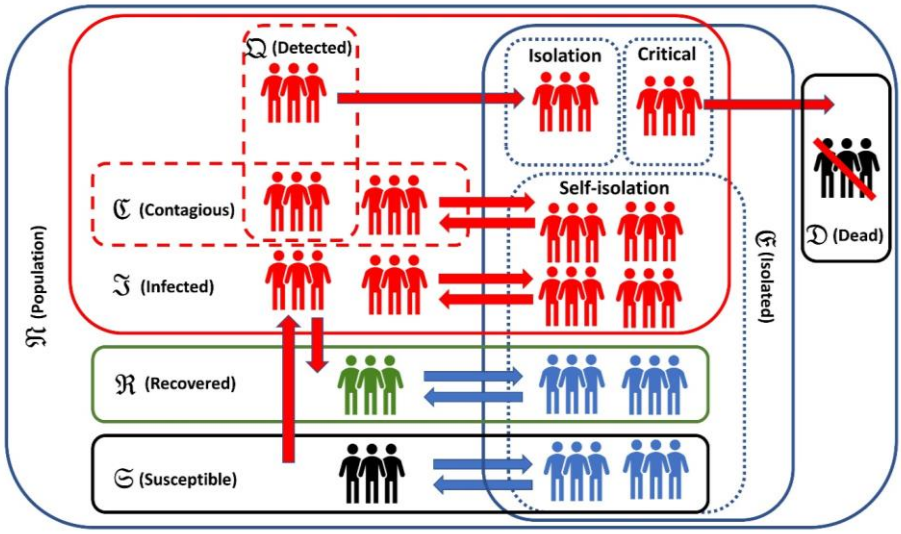


Fig. 1 Basic schematic of the employed agent-based model with a general pool.

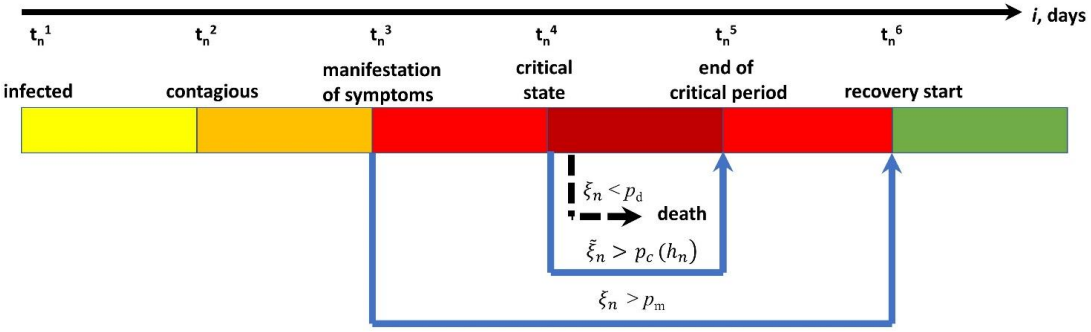


Fig. 2 Schematic of a general disease scenario.

all the agents that leave their homesteads on a particular day, interact with other agents, and have the equal probability to be infected. The latter is determined by the number of infected agents, that are not isolated and also go out to the "pool".

Each agent has basic properties (age h_n) and the following Boolean states: "infected" (α_n^1), "contagious" (α_n^2), "symptomatic" (α_n^3), "in critical state" (α_n^4), "dead" (α_n^5), "recovered" (α_n^6), "isolated" (α_n^7), "positive test" (α_n^8) that are set as 'false' (0) at the initialization of the simulation and are further governed by the Monte Carlo principle depending on a scenario. The basic properties of each agent are predefined randomly in accordance with the official statistical data on the population age structure.

If for an agent n the state "infected" becomes 'true' ($\alpha_n^1 = 1$) on day $i = t_n^1$, a specific random scenario for each infected person is generated based on the predefined probability density distributions $f_i(t)$.

The schematic of a general disease scenario is shown in Fig. 2. The probabilities of symptoms manifestation p_m and critical period $p_c(h_n)$ are defined separately, and the latter depends on an individual's age h_n. Any agent with the status "in critical state" ($\alpha_n^4 = 1$) has a chance to die on any day of critical period with the given death probability p_d. The following scenario time points (t_n^k) are determined in accordance with predefined probability density distributions $f_k(\tau)$ based on available statistical data on disease progression: day when person becomes contagious (t_n^2), symptoms manifestation day (t_n^3), critical state day (t_n^4), critical state overcome day (t_n^5), and recovery start day (t_n^6),

$$t_n^k = t_n^1 + F_k^{-1}(\xi_n),\ k = 2, 3; \quad (1)$$

$$t_n^k = t_n^{k-1} + F_k^{-1}(\xi_n),\ k = 4, 5; \quad (2)$$

$$t_n^6 = \begin{cases} t_n^1 + t_d \,|\, \tilde{\xi}_n > p_c(h_n) \\ t_n^1 + t_d + t_n^5 - t_n^4 \,|\, \tilde{\xi}_n < p_c(h_n) \end{cases}, \quad (3)$$

where t_d is the typical disease duration, ξ_n , $\tilde{\xi}_n$ are random numbers uniformly distributed on the interval [0, 1], $F_k(t)$ is the cumulative distribution function of corresponding parameter:

$$F_k(t) = \int_{t_n^1}^{t} f_k(\tau) d\tau, \quad (4)$$

and $F_k^{-1}(\xi_n)$ represents the inverse function. In turn, these parameters determine the corresponding time points of the status change:

$$\alpha_n^2 = 1 \mid i = t_n^2, \tag{5}$$

$$\alpha_n^3 = 1 \mid i = t_n^3, \xi_n < p_m, \tag{6}$$

$$\alpha_n^4 = \begin{cases} 1 \mid i = t_n^4, \xi_n < p_m, \tilde{\xi}_n < p_c(h_n) \\ 0 \mid i = t_n^5, \xi_n < p_m\ \tilde{\xi}_n < p_c(h_n) \end{cases} \tag{7}$$

where ξ_n , $\tilde{\xi}_n$ are random numbers uniformly distributed on the interval [0, 1], in here a single call for each random number value is supposed.

2.1.2 Implementation of the General Pool Concept

In each day the set of daily recovered agents is determined among those agents who reached the recovery start day in accordance with the rule:

$$\bar{\mathfrak{R}}: \{ a_n \mid i \geq t_n^6, \alpha_n^5 = 0, \xi_n < p_r\}, \tag{8}$$

$$\alpha_n^6 = 1, \alpha_n^2 = 0, \alpha_n^3 = 0, \alpha_n^7 = 0, \quad \alpha_n^8 = 0 \mid a_n \in \bar{\mathfrak{R}}. \tag{9}$$

The daily death probability p_d during the critical period is predefined but can vary with time reflecting the current situation with medical care: an overflow of the region hospitalization capacity may decrease in the quality of provided treatment therefore resulting in an increase in the probability of a death. The set of daily deaths $\bar{\mathfrak{D}}$ is determined in accordance with the following rule:

$$\bar{\mathfrak{D}}: \{ a_n \mid \alpha_n^4 = 1, \xi_n < p_d\}, \tag{10}$$

$$\alpha_n^5 = 1, \mid a_n \in \bar{\mathfrak{D}}. \tag{11}$$

where p_r is the daily recovery probability constructed in a similar way to the death probability. In contrast to SIR-like models [12–20], where the total numbers of susceptible, infected and recovered persons are governed by differential equations, in the agent-based model, we consider the evolutions of the sets of susceptible agents ($\mathfrak{S}$), infected agents ($\mathfrak{I}$), recovered agents ($\mathfrak{R}$), and dead agents ($\mathfrak{D}$) together with the set of contagious agents ($\mathfrak{C}$) that can transmit infection to other agents ($\mathfrak{C} \subseteq \mathfrak{I}$) as follows:

$$\mathfrak{D}: \{a_n \mid \alpha_n^5 = 1\}, \tag{12}$$

$$\mathfrak{S}: \{a_n \mid \alpha_n^1 = 0\} \setminus \mathfrak{D}, \tag{13}$$

$$\mathfrak{I}: \{a_n \mid \alpha_n^1 = 1\} \setminus \mathfrak{D}, \tag{14}$$

$$\mathfrak{R}: \{a_n \mid \alpha_n^6 = 1\} \setminus \mathfrak{D}, \tag{15}$$

$$\mathfrak{C}: \{a_n \mid \alpha_n^2 = 1\} \setminus \mathfrak{D}. \tag{16}$$

The isolation of agents in the developed model rests on two mechanisms: the first is the self-isolation, which means that the agent does not go out to the general pool on a particular day basing either on official governmental recommendations, or on early onset of a disease; the second mechanism implies forcing an agent to stay at home or hospitalization in the case of COVID-positive test result. As so, depending on the introduced anti-epidemic measures accounted in the simulation, agents also may get a binary status "isolated" ($\alpha_n^7 = 1$) if a positive COVID-19 test happens or due to self-isolation, if they fulfill the restrictive measures on a current day. Isolated agents do not interact with the general pool and cannot transmit infection. The developed simulation model accounts for the efficiency of the following restrictive measures with the employment of what is known as self-isolation index. This is an empirical value similar to one firstly introduced by Yandex (Russia) during the COVID-19 outbreak, which represents a cumulative parameter reflecting population social activity based on both traffic information and activities in different internet services. In the simulations, the self-isolation index (I_s) varies between 0 and 5. Day-scale time resolution allows us to account for the self-isolation index variations associated with vacations, New Year holidays etc. We introduce, and the quarantine quality κ which is assumed to be proportional to I_s and is, described by the empirical law:

$$\kappa = \frac{0.5 + 0.7 I_S}{5}. \tag{17}$$

This linear relation was constructed empirically in order to fit the official data. The set $\mathfrak{E}$ of isolated agents that obey restrictive rules and do not interact with the general pool on a current day is determined based on current κ value. Day-scale temporal resolution allows to account for self-isolation index variations associated with vacations, New Year holidays etc.

$$\mathfrak{E}: (\{a_n \mid \alpha_n^3 = 0 , \xi_n < \kappa\} \cup \{a_n \mid \alpha_n^3 = 1, \xi_n < p_e\} \cup \{a_n \mid \alpha_n^4 = 1\} \cup \{a_n \mid \alpha_n^8 = 1\}) \setminus \mathfrak{D}, \tag{18}$$

$$\alpha_n^7 = 1 \mid a_n \in \mathfrak{E}. \tag{19}$$

The disease transmission rate is governed by the parameter r that is defined as an average number of agents infected by a spreader in the population during one week given that no restrictions or isolation aids are imposed. Given that the probabilities to be infected from different agents are independent, the daily infection probability p_{is} for a given susceptible agent interacting with the general pool in a particular day i is calculated as:

$$p_{is} = (r\,|\mathfrak{C} \cap (\mathfrak{R} \setminus \mathfrak{E})|)/(7N). \tag{20}$$

The probability of being infected p_{is} is equal for all agents who visit the pool in the current day (those who are not isolated or self-isolated, the probability is determined in accordance with the current self-isolation index). Hence, the set of agents infected on a particular day i is determined as:

$$\bar{\mathfrak{I}}: \{a_n \mid a_n \in \mathfrak{S} \backslash \mathfrak{E}, \xi_n < p_{is}\}, \quad (21)$$

$$\alpha_n^1 = 1 \mid a_n \in \bar{\mathfrak{I}}, \quad (22)$$

where ξ_n is a random number uniformly distributed on the interval [0, 1].

2.1.3 Connection with SIRD-Like Models

The proposed approach can be directly related to the typical SIRD-like models. The variables considered in SIRD-like models could be derived as the cardinalities of the considered agent sets:

$$S = |\mathfrak{S}|, \quad (23)$$

$$I = |\mathfrak{I}|, \quad (24)$$

$$R = |\mathfrak{R}|, \quad (25)$$

$$D = |\mathfrak{D}|, \quad (26)$$

which dynamics can be evaluated from basic equations resembling the discrete form of the classical SIRD model:

$$I_i = I_{i-1} + \Delta I_i - \Delta R_i - \Delta D_i, \quad (27)$$

$$S_i = S_{i-1} - \Delta I_{i+1}, \quad (28)$$

$$R_i = R_{i-1} + \Delta R_i, \quad (29)$$

$$D_i = D_{i-1} + \Delta D_i, \quad (30)$$

where i denotes current day number, while

$$\Delta I_i = |\bar{\mathfrak{I}}|, \quad (31)$$

$$\Delta R_i = |\bar{\mathfrak{R}}|, \quad (32)$$

$$\Delta D_i = |\bar{\mathfrak{D}}|, \quad (33)$$

are the daily numbers of infected, recovered and dead agents, respectively.

2.1.4 Testing System Model

An important part of the simulation is the testing system, since the daily statistics on the number of incident cases and deaths of numerical simulations have to be compared to the real data. Obviously, these data depend on the region-specific testing strategies, which may significantly vary between different regions. In addition, they could serve as tuning parameters of the entire model. In the simulations the tested group $\bar{\mathfrak{X}}$ is determined each day and consists of three parts: agents with symptoms $\mathfrak{M}$, agents infected by the infected agents $\mathfrak{U}$ revealed on the previous day, and random agents $\mathfrak{Z}$ from the rest of population:

$$\bar{\mathfrak{X}} = \mathfrak{M} \cup \mathfrak{U} \cup \mathfrak{Z}, \quad (34)$$

$$\mathfrak{M}: R_p(|\mathfrak{M}|, \{a_n \mid \alpha_n^3 = 1\}), \quad (35)$$

$$\mathfrak{U}: R_p(|\mathfrak{U}|, \{a_n \mid \alpha_n^2 = 1\}), \quad (36)$$

$$\mathfrak{Z}: R_p(|\mathfrak{Z}|, (\mathfrak{S} \cup \mathfrak{I} \cup \mathfrak{R}) \backslash \{a_n \mid \alpha_n^4 = 1\}), \quad (37)$$

where $R_p(j, \mathfrak{A})$ is a random permutation of j elements from set $\mathfrak{A}$. The numbers of agents in each of subgroups $\mathfrak{M}$, $\mathfrak{U}$, $\mathfrak{Z}$ are defined in accordance with the following rules:

$$|\mathfrak{M}| = d\,|\{a_n \mid \alpha_n^3 = 1, \alpha_n^8 = 0\}|, \quad (38)$$

$$|\mathfrak{U}| = N_{cont}\,|\bar{\mathfrak{Q}}_{i-1}|, \quad (39)$$

$$|\mathfrak{Z}| = N_i^{test} - |\mathfrak{M}| - |\mathfrak{U}|, \quad (40)$$

where parameter d characterizes the fraction of the tested agents among all symptomatic agents that have no positive test results, and N_{cont} describes the average number of infected agents tested as contacts of the agents with positive tests $\bar{\mathfrak{Q}}_{i-1}$ revealed on the previous day i–1. These parameters may vary depending on testing capacity and psychological status of population. The total number of tests N_i^{test} taken at day i is a predefined parameter, which can be obtained from the official statistics data. The parameters d and N_{cont} are empirical and are chosen to satisfy the condition:

$$|\mathfrak{M}| + |\mathfrak{U}| < N_i^{test}. \quad (41)$$

The set of daily detected cases $\bar{\mathfrak{Q}}$ is determined based on the predefined test accuracy a_c:

$$\bar{\mathfrak{Q}}: \{a_n \mid a_n \in \bar{\mathfrak{X}}, \xi_n < a_c\}, \quad (42)$$

$$\alpha_n^8 = 1 \mid a_n \in \bar{\mathfrak{Q}}. \quad (43)$$

It is also assumed in the model that all the agents with positive test results are subject to isolation until their recovery:

$$\alpha_n^7 = 1 \mid a_n \in \bar{\mathfrak{Q}}. \quad (44)$$

The number of daily detected infected agents is the number of elements in $\bar{\mathfrak{Q}}$:

$$\Delta Q_i = |\bar{\mathfrak{Q}}|. \quad (45)$$

The dynamics $\Delta I_i(i)$, $\Delta D_i(i)$, $\Delta Q_i(i)$ are the major dependencies derived in simulations: $\Delta D_i(i)$, $\Delta Q_i(i)$ could be compared to the official statistical data, while $\Delta I_i(i)$ reveals the real progression of the epidemic.

2.2 Model Parameters Used in the Simulations

The probability distributions for different parameters of a disease scenario (Fig. 3) are based on the available statistical data on COVID-19 [38–41] and determine the probabilities and durations of each period of the disease: period before being contagious, incubation period, disease development period, critical period, and the probability of critical state occurrence depending on the agent's age. The simulations reported in this study consider only the first two waves of the pandemic (period from February 26th, 2020 to April 06th, 2021), at which the effect of vaccination omitted in the described model could be considered to be negligible. Moreover, it is assumed that the abovementioned parameters do not vary with time, since both these waves are caused by the COVID strains with similar contamination abilities, except death occurrence probability during the critical stage, since it also depends on the availability and quality of medical care.

These distributions were already used in our previous study [42] aiming at predicting the progression of the first pandemic wave. In this study, the simulations of the epidemic progress were performed for Moscow ($N = 11.4 \cdot 10^6$), Nizhny Novgorod region ($N = 3.3 \cdot 10^6$) and Novosibirsk region ($N = 2.7 \cdot 10^6$).

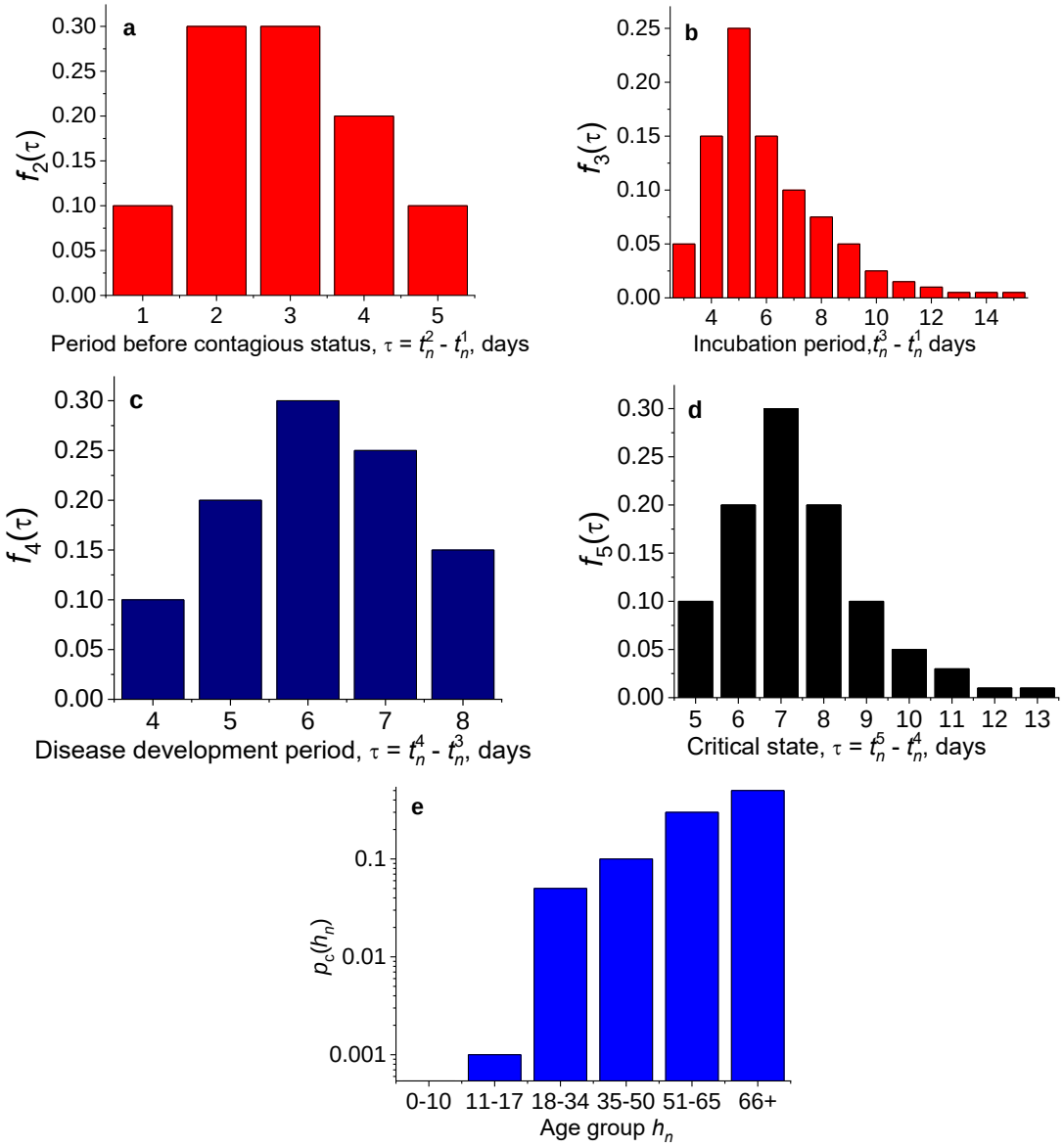


Fig. 3 Probability density distributions of the disease scenario parameters: period from infection to the contagious status $\tau = t_n^2 – t_n^1$ (a), incubation period $\tau = t_n^3 – t_n^1$ (b), period from the disease manifestation to the critical state $\tau = t_n^4 – t_n^3$ (c), critical state period $\tau = t_n^5 – t_n^4$ (d), and the age-dependent probability of critical state occurrence $p_c(h_n)$ (e) employed in simulations.

Table 1 Values of main parameters employed in simulations.

Parameter	Abbreviation	Value
Probability of symptoms manifestation	p_m	0.3
Daily death probability in critical state	p_d	0.04
Average weekly number of agents infested by a spreader	r	4.6
Probability of isolation decision for agents with symptoms manifestation	p_e	0.5

The reproducibility rate value was determined in the course of fitting the official statistics for the first wave only [42], resulting in the value of $r = 4.6$ for all the considered regions. The number of initial infected agents for all regions was the same as previously reported in Ref. [42].

It was assumed that both the first and the second wave were caused by the COVID strains with similar contamination abilities, so this parameter was kept constant in all the simulations. The same assumption concerns the probability of symptoms manifestation p_m which was predefined 0.3, which corresponds to 70% of silent (symptomless) cases typically reported in the beginning of the pandemic. Death probability p_d was considered to be time-independent for all the regions, but its value was different for different regions, which can be associated with difference of treatment quality. It is assumed that the statistics of new deaths strongly correlates with the statistics of new cases, and the p_d coefficient was determined by finding the best fits time series after the fit of the series for daily new cases for each region.

In order to fit the increase of COVID-19 associated lethal cases in Moscow in the period from 10 February 2021 to 06 April 2021 we increase the p_d value for Moscow within this period. This may originate from deficiency of bed capacity or increased fatality ratio due to virus mutations. The values of the key probabilistic parameters employed in simulations are summarized in Table 1.

In our simulations the testing model is based on the available data of daily tests for the entire country (Fig. 4a), since the availability of the data for specific regions is much lower. Consequently, the number of daily tests for each region is either taken from official statistics [43] or determined from the daily number of cases for the entire Russian Federation (Fig. 4a) [44] in proportion to the particular region population. Fig. 4b shows the relevance of such an evaluation for available data for the Nizhny Novgorod region and compares estimated numbers with actual data obtained for the period 10.10.2020 – 10.04.2021. The fraction of tested agents with symptoms d was assumed to be equal to zero for first 25 days of simulation (26 February 2020 – 23 March 2020) indicating the time required to develop a testing system, and then shifts to a non-zero value and increases with the number of day i according to the following law:

$$d(i) = \begin{cases} 0, i \le 25 \\ d_0 + (d_f - d_0)\frac{i^3}{i^3 + i_d^3}, i > 25 \end{cases}, \qquad (46)$$

where d_0 is initial value for $i > 25$, d_f is asymptotic value being reached for $i \gg i_d$, i_d is an empirically chosen parameter.

The parameter N_{cont} determining the average number of infected persons tested in the frames of the testing contacts of the agents $\bar{\Omega}_{i-1}$ who got the positive test on the previous day $i - 1$, was assumed to be either constant through the entire simulation period, or to have a step-wise decrease in the end of the second wave, since the first wave period was characterized by the maximal efforts to reveal all the cases.

It is worth mentioning that the tests accuracy a_c was rather low in the beginning of the pandemic, and, in this respect, the test sensitivity is assumed to increase with time in the beginning of the pandemic. Similar to the dynamics of d, it was assumed that a_c is described by the following law:

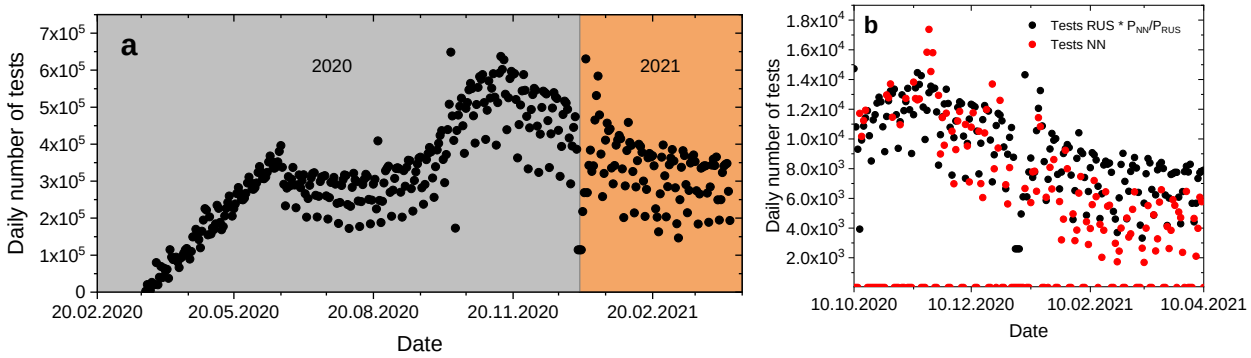


Fig. 4 Daily number of tests in Russian Federation (RUS) in the period 20 February 2020 – 20 April 2021 (a) and daily number of tests in Nizhny Novgorod region (NN) versus evaluation in the period 10 October 2020 – 10 April 2021 (b). Ratio P_{NN}/P_{RUS} is the ratio of populations of Nizhny Novgorod region and Russian Federation.

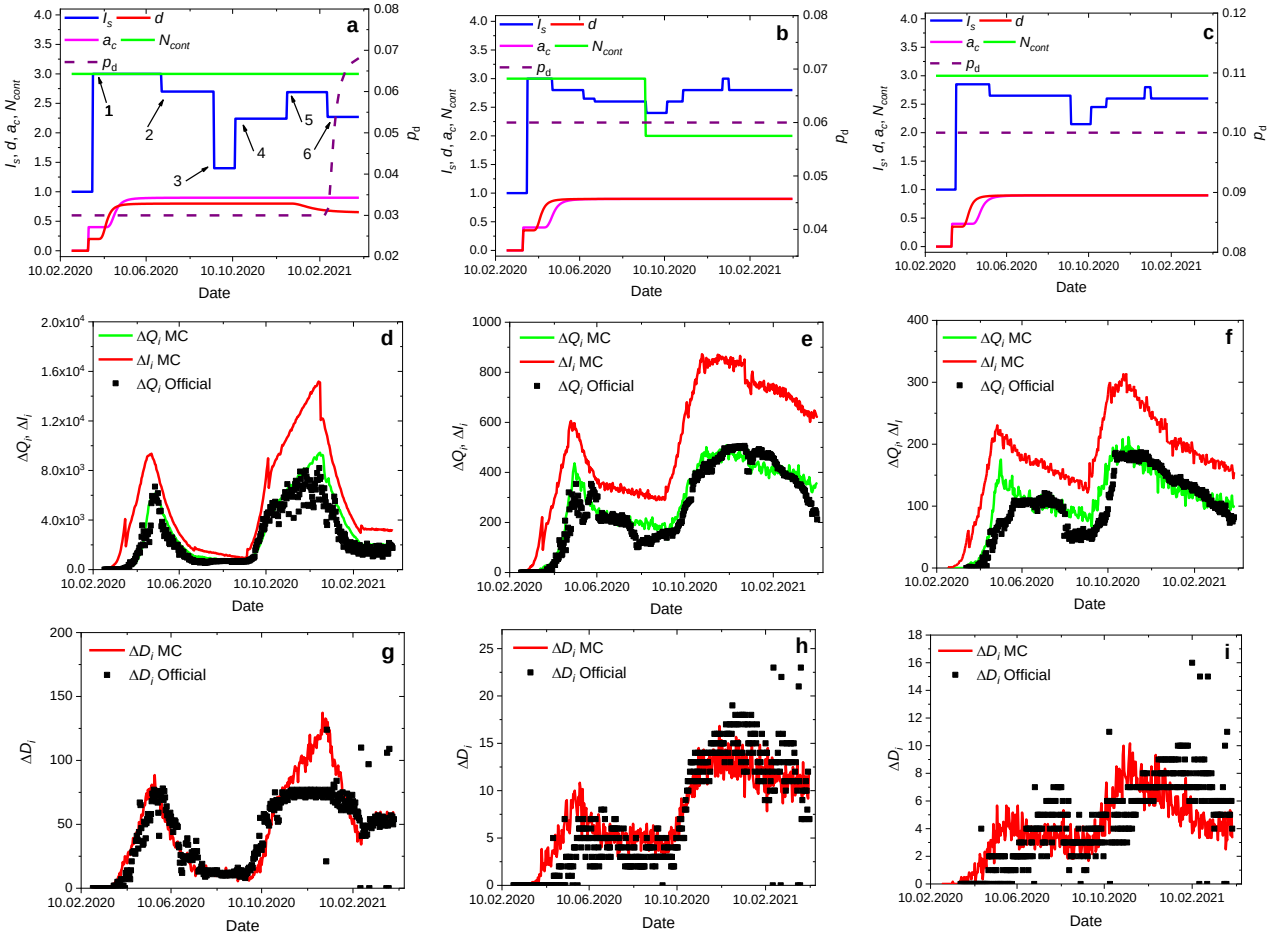


Fig. 5 Empirically chosen simulation parameters (a, b, c) and comparison of simulated scenarios (MC) and official statistical data (Official) for daily numbers of newly revealed COVID-19 (d, e, f) and COVID-19–associated deaths (g, h, i) in Moscow (a, d, g), Nizhny Novgorod region (b, e, h) and Novosibirsk region (c, f, i) in the period of 26 February 2020 – 06 April 2021.

$$a_c(i) = \begin{cases} 0, i \le 25 \\ a_{c,0} + (a_{c,f} - a_{c,0}) \frac{i^3}{i^3 + i_T^3}, i > 25 \end{cases}, \quad (47)$$

where i is the number of simulation day starting from 26 February 2020, initial $a_{c,0}$ and asymptotic $a_{c,f}$ values are chosen empirically, as well as i_T. The specificity of the tests is assumed to equal 100%, and no false positive test results are considered in simulations.

To provide a best-fit scenario, we manipulated with parameters of the model, namely, primarily the self-isolation index I_s and testing strategy parameters d, N_{cont} and a_c. Each scenario was constructed by simulation of 10 random scenarios with the same parameters and further averaging five scenarios that gave the minimal deviation from the official data. Due to the stochastic origin of the developed model, similar starting parameters may result in totally different scenarios of an epidemic progress.

3 Results

This study includes the analysis for three regions: Moscow, Nizhny Novgorod region, and Novosibirsk region. Fig. 5 shows the best fit scenarios obtained for these regions. The dependencies of the key time-dependent parameters for the considered regions are shown in Figs. 5a–c. At the first step the parameters for the Moscow region (Fig. 5a) were determined. The variation of the self-isolation index is the most significant among other parameters and its dynamics is regulated by the dates of municipal and governmental decrees and social processes: introduction of the quarantine regime (1), release of the restrictions (2) followed by further cancellation of restrictive measures (3), restoration of restrictive measures after the second wave start (4), a winter-time isolation increase related to New Year holidays (5), and its release (6). The parameters of the testing system are quite hard to be accurately extracted from the official data, so they were empirically fitted based on general conclusions. The test accuracy a_c was assumed to be quite low ($a_{c,0}$ = 0.4) in the beginning of the testing period and rose up to 90% ($a_{c,f}$ = 0.9) during two months of the testing period (4). In Moscow the rise of the test accuracy (Fig. 5a) is assumed to be faster, since the newly developed tests arrive first of all to the capital, which is followed by their distribution to other regions. Similar trend is chosen for the percentage d of the

symptomatic agents with symptoms manifestation that are being tested (3). It is assumed, that in the very beginning of the pandemic only few of them are tested, however, with its progression the testing strategy changes both due to governmental requirements and people's awareness. The latter decrease in the d parameter for Moscow (Fig. 5a) simulates smaller attention to early symptom manifestation.

Figs. 5d–f show the simulated dynamics of the new daily COVID-19 counts, while Figs. 5g–i present the simulated dynamics of the daily COVID-19 associated lethal cases for Moscow, Nizhny Novgorod region and Novosibirsk region, respectively. Official statistical data for daily counts and daily deaths that was fitted by manipulating the simulation parameters (Figs. 5a–c) are given in each plot for the reference in Figs. 5d–i; scatter data show the official statistical data, while solid lines show the simulated dynamics. The new daily counts dynamics ΔQ_i show good agreement with the official statistics, especially for Moscow and Novosibirsk region, while an insignificant discrepancy is observed for the beginning of the first wave for Nizhny Novgorod region. Agreement of the simulation results with the official statistics data (Figs. 5d–f) demonstrate the relevance of the developed model. Although the deviations may occur in particular days, the general trend is reproduced quite accurately for all three considered regions (Figs. 5d–f) with the same parameter r governing disease properties and associated with the reproducibility rate. An important advantage of the employed approach is the ability to predict the real number of new cases, including those that were not tested and thus did not contribute to the official statistics. In Figs. 5d–f solid green lines demonstrate calculated dynamics of daily detected cases, while red solid lines show the dynamics of the evaluated total new COVID-19 cases. The simulations show a 1.5–2 fold difference between the evaluated numbers of the officially confirmed new daily counts and the evaluated number of total daily cases.

It is important to note that in general the daily deaths time series ΔD_i follow the trend of the daily new cases ΔQ_i with the delay equal to the average period between first manifestation and death, as can be seen from official statistics data. Since in accordance with official statistics the death rate does not exceed 5% [45, 46], the number of daily new COVID-19-associated deaths was simulated by varying the parameter p_d only.

The observed trend is reproduced in all the considered regions except the second wave for Moscow, where the daily death statistics (Fig. 5g) shows a plateau, which is not observed in the simulated daily new cases graph (Fig. 5d). In this connection, a discrepancy occurs between the model predictions and official statistics (Fig. 5g), although for other considered regions (Figs. 5h, i) the agreement is much better. It is also worth mentioning that the time shift between the dependencies ΔQ_i and ΔD_i is smaller for Moscow as compared to Novosibirsk and Nizhny Novgorod, which is most probably due to delay in the representation of COVID-19 associated death cases in official statistics in the regions with respect to Moscow, since the difference in disease progression in different regions is not expected. This discrepancy could be compensated by introducing a corresponding delay to the model, however, it was avoided to maximally keep the basic parameters of the model for different regions.

Despite the similarity of the key model parameters for the first wave of the pandemic in the chosen regions, for the second wave different trends were revealed to govern the wave progression in different sites: for Moscow an increased death probability was introduced in the end of the second wave (Fig. 5a), while for Nizhny Novgorod region the number of tested contacts N_{cont} was decreased (Fig. 5c). In Moscow city the summer relaxation period followed by the beginning of the second wave was related to a higher decrease in isolation index as compared to other regions. In Supplementary materials we present a collection of the simulation results which do not show the good fit to the official data, however allow to see the effect of particular parameters on the model predictions.

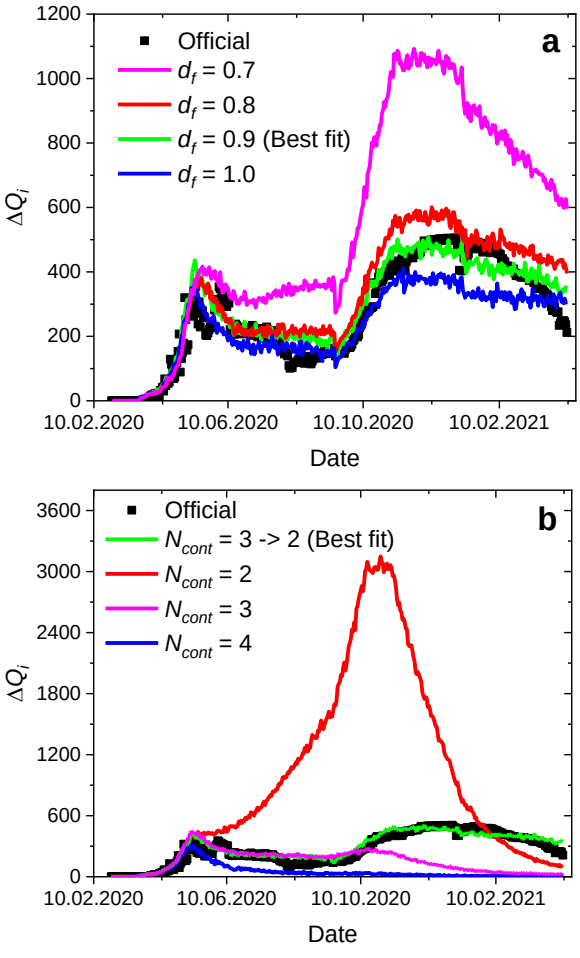


Fig. 6 Comparison of simulated scenarios (MC) and real statistical data (Official) for daily numbers of newly revealed COVID-19 cases for different percentage of tested agents (different dynamics of fraction of tested agents with symptoms d) with symptoms manifestation (a) and different number of tested agents, which were in contact with an agent with positive COVID-19 test (b) in the period of 26 February 2020 – 06 April 2021.

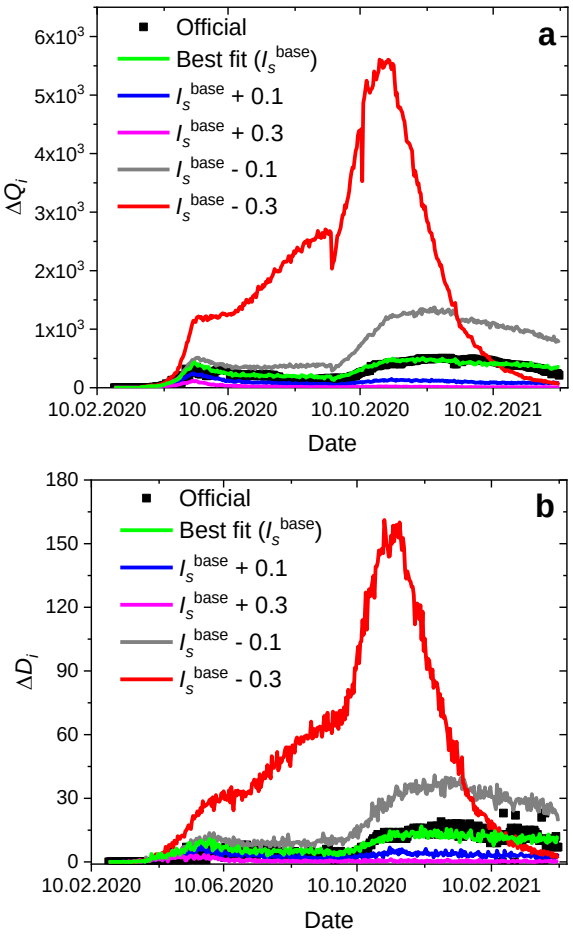


Fig. 7 Comparison of simulated scenarios and real statistical data (Official) for daily numbers of newly revealed COVID-19 (a) and COVID-19-associated deaths (b) for different self-isolation index I_s in Nizhny Novgorod region in the period of 26 February 2020 – 06 April 2021.

In order to analyze the impact of testing strategy parameters on the epidemic process we performed simulations for Nizhny Novgorod region varying parameters d and N_{cont}. We limit ourselves by only one region in this part of the study, since we expect that the general trends will be similar for different regions owing to similarity of the model parameters, since the considered variations are higher than those between different regions. The results for the daily revealed cases ΔQ_i for different values of the parameters d and N_{cont} are shown in Figs. 6a and 6b, respectively.

In simulations presented in Fig. 6a, the evolution of the fraction of agents with symptoms manifestation d that are tested is described by Eq. 3, similar to previous simulations with a fixed value of $d_0 = 0.35$, while d_f value is varied between 0.7 and 1.0. The increase in d_f value leads to higher detection rate and, hence, a faster isolation of the infected agents and a corresponding decrease in the number of the revealed and total COVID-19 cases. Note that even the total testing of all the agents with symptoms manifestation ($d_f = 1$) does not provide full elimination of the pandemic progression owing to both high percentage of symptomless disease progression and limited accuracy of the tests.

Fig. 6b shows simulated dynamics of ΔQ_i for different number of tested infected agents N_{cont} that were previously contacting with the revealed cases. Similar to variations in d, the increase in N_{cont} leads to decrease in daily detected COVID-19 cases and vice versa. A pronounced rise in ΔQ_i for $N_{cont} = 2$ (red line) with a further sharp decrease indicate the herd immunity development, when most agents were infected and then recovered or died. The decrease of ΔQ_i to zero for $N_{cont} = 3$ and $N_{cont} = 4$ indicates the situation when all the infected agents were revealed and isolated thus preventing further development of the pandemic.

Fig. 7 demonstrates the effect of the basic level of the self-isolation index I_s on the dynamics of daily revealed and lethal COVID-19 associated cases ΔQ_i and ΔD_i calculated for Nizhny Novgorod region. The results are shown for basic self-isolation index dynamics I_s^{base} (as shown in Fig. 5c) and its variations (± 0.1 and ± 0.3 from base values for all days during considered period).

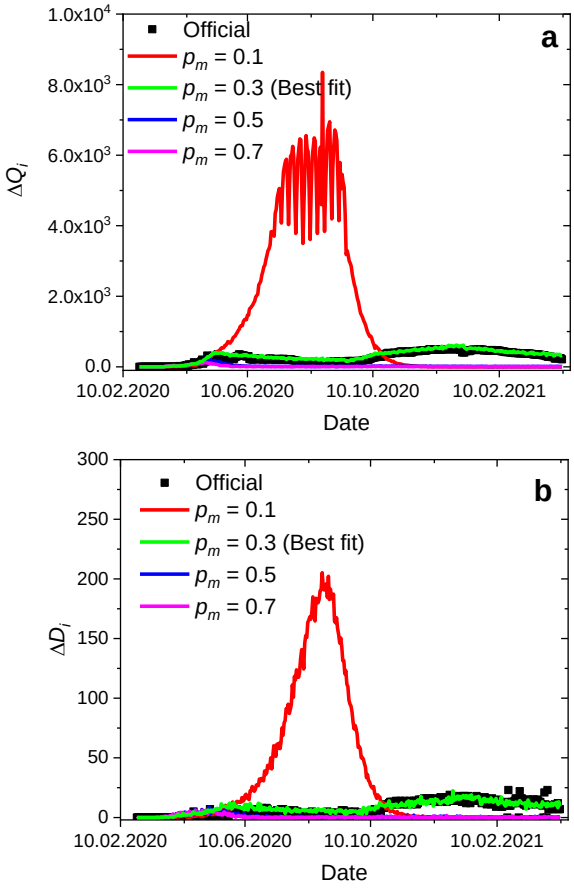


Fig. 8 Comparison of simulated scenarios and real statistical data (Official) for daily numbers of newly revealed COVID-19 (a) and lethal COVID-19 associated (b) cases in Nizhny Novgorod region for different probability of symptoms manifestation p_m in the period of 26 February 2020 – 06 April 2021.

The simulated dynamics show clear evidence that the increase of the self-isolation index leads to the decrease

in social activity and, hence, slows down the epidemic process and vice versa. Note that similar to the case of $N_{cont} = 2$, the decrease of I_s^{base} for the value of 0.3 induces a sharp increase in the number of daily revealed cases followed by a sharp drop indicating the formation of herd immunity, while similarly to the case of $N_{cont} = 4$ (Fig. 6b), a suppression of epidemic progression is observed for the increase of the isolation level ($I_s^{base} + 0.3$).

Another important parameter of the model is the probability of symptoms manifestation p_m. Fig. 8 shows the results of simulations for Nizhny Novgorod region with basic parameters (Fig. 5c) and different manifestation probability p_m.

As it can be seen form Fig. 8a, the increase in the percentage of symptoms manifestation leads to a larger number of potentially tested agents and, therefore, to the timely isolation of infected agents. With the significant decrease of symptoms manifestation probability, the pandemic scenario is represented by a quick spread of infection and the development of herd immunity (Fig. 8a, red curve), accompanied by huge number of lethal cases (Fig. 8b, red curve).

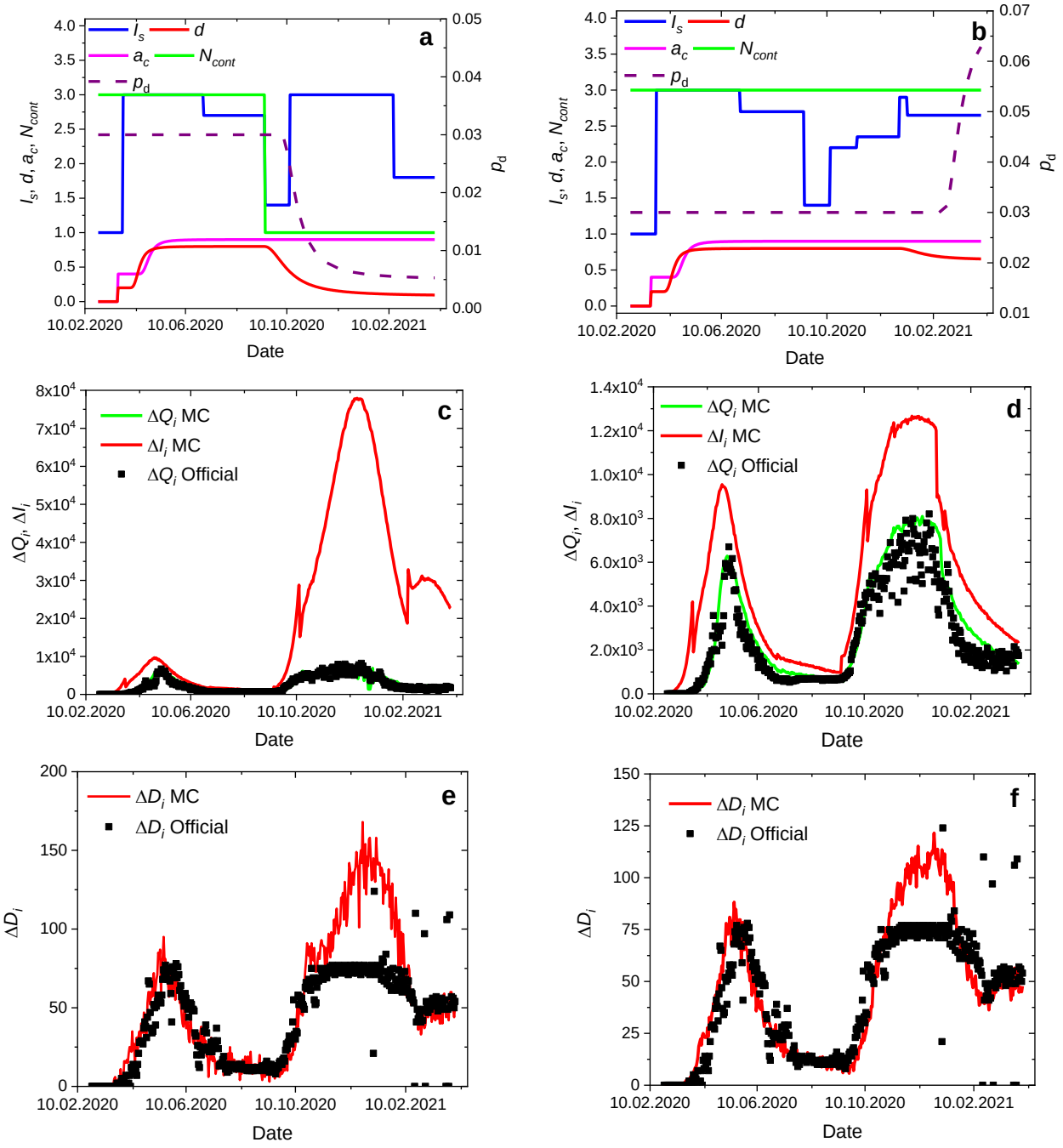


Fig. 9 Empirically chosen alternative simulation parameters (a, b) and comparison of corresponding simulated scenarios (MC) and official statistical data (Official) for daily numbers of newly revealed COVID-19 (c, d) and COVID-19 – associated deaths (e, f) in Moscow in the period of 26 February 2020 – 06 April 2021.

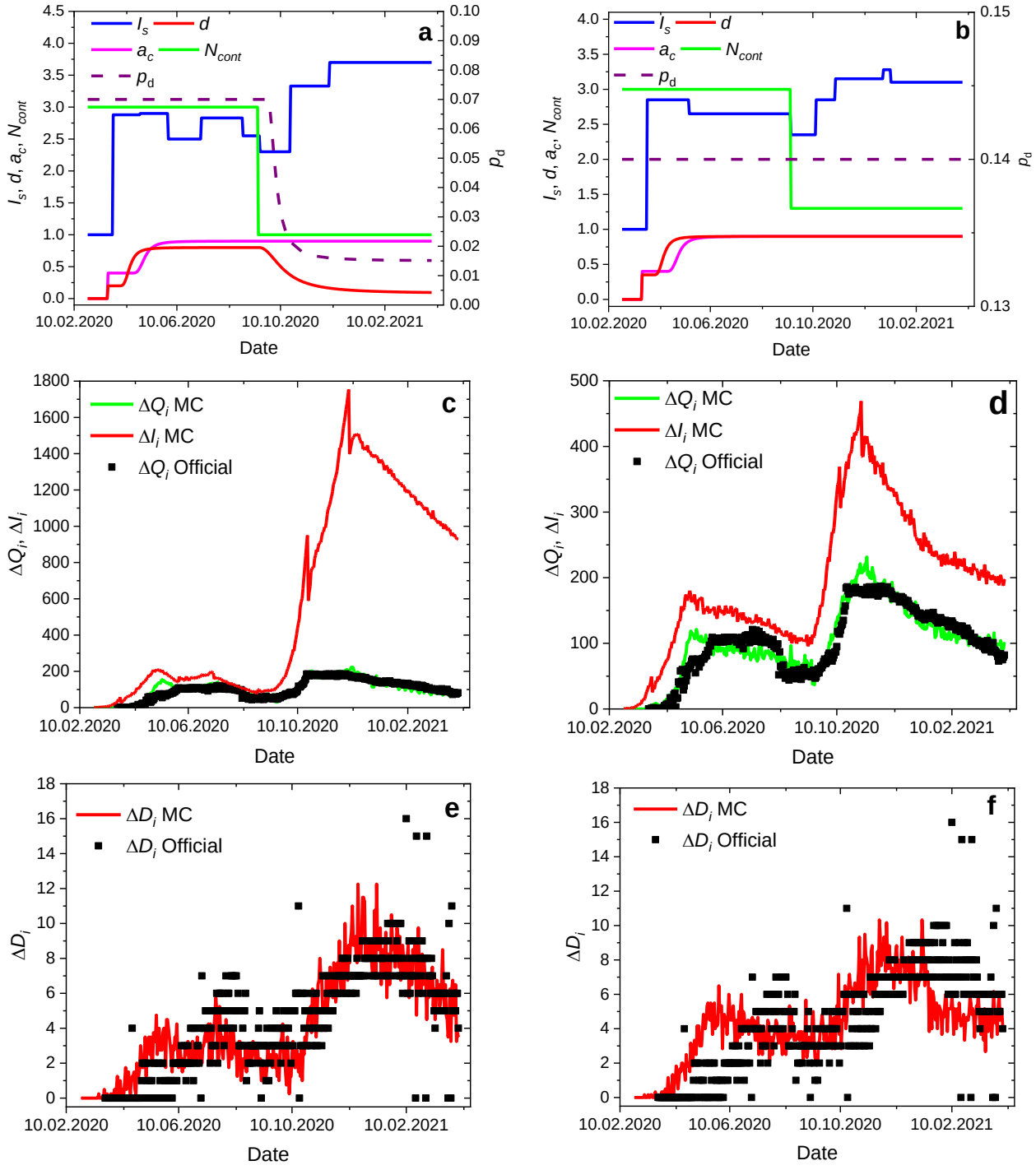


Fig. 10 Empirically chosen alternative simulation parameters (a, b) and comparison of corresponding simulated scenarios (MC) and official statistical data (Official) for daily numbers of newly revealed COVID-19 (c, d) and COVID-19–associated deaths (e, f) in Novosibirsk region in the period of 26 February 2020 – 06 April 2021.

Since the considered simulation of pandemic progression is a multiparameter problem, several solutions could be found to fit the given official statistics data. Abovementioned results were obtained for realistic parameters, e.g. relatively smaller self-isolation index I_s during the second wave of COVID-19 in comparison to the first one. Nonetheless, different solutions were found for Moscow (Fig. 9) and Novosibirsk region (Fig. 10) fitting official statistics well, and suggesting comparable isolation index during the first and the second waves of the pandemic (Figs. 9a, b and 10a, b) or even higher isolation index during the second wave (Fig. 9d, e and 10d, e). However, these scenarios implied a significant variation of p_d and d parameters during the second wave (Figs. 9c and 9f).

As can be seen from Figs. 9 and 10, the major difference of these scenarios from those shown in Fig. 5 lies in the total number of daily COVID-19 cases, which is significantly

higher than routinely revealed COVID-19 cases (demonstrating from 2 to 9-fold difference). This situation indicates that although the proposed model provides good agreement with the reported official statistics, additional information regulating model parameters is to be employed for more accurate simulation and prediction of further pandemic progression.

4 Conclusion

In this paper we presented an agent-based model of COVID-19 epidemic spread with the employment of Monte Carlo simulation principles. The model is able to account for the age-dependent disease development, restrictive measures as well as testing system. The results are encouraging and were validated on the statistical data for daily new cases and deaths which were reported during the first and the second waves of COVID-19 pandemics from three representative regions of Russia, such as the Moscow city, Nizhny Novgorod region, and Novosibirsk region. The results of simulations show the possibilities of developed model for the simulation of disease spread with regard to analysis of restrictive measurements and different testing strategies.

It is worth noting that different combinations of simulations parameters could provide similar results in the dynamics of newly revealed cases and deaths, although the dynamics of total cases in such scenarios may differ significantly. This indicates, that some parameters of the model should be defined independently based on available information on social activity/testing strategy, etc., which could increase the accuracy of the prognosis provided by the model.

The reported results demonstrate the abilities of the developed model in simulating the progression of the epidemics, however, owing to a multiparametric nature of the considered problem, the choice of the parameters remains an important issue in performing simulations. The approach used in this study is based on employing available parameters, such as statistics on population, percentage of symptomless cases, number of daily tests etc., and finding the empirical values for other parameters that govern social activity issues, that cannot be extracted directly. It is worth noting that the parameters found for particular regions could be used as starting sets for another regions providing fast solution.

As it was mentioned in the model description, the general pool concept could be connected with the classical compartmental model, however, consideration of individual agents gives more flexibility to the model allowing to avoid considering numerous small compartments that would be required in case of application of a compartmental model in similar settings and detalization.

Disclosures

The authors have no relevant financial interest in this article and no conflict of interest to disclose.

Acknowledgements

The study is supported by RFBR (project no. 20-51-80004), CNPq (project no. 441016/2020-0), and NSFC (project no. 82161148012).

References

1. T. Carletti, D. Fanelli, and F. Piazza, "COVID-19: The unreasonable effectiveness of simple models," Chaos, Solitons & Fractals: X 5, 100034 (2020).
2. E. Pelinovsky, A. Kurkin, O. Kurkina, M. Kokoulina, and A. Epifanova, "Logistic equation and COVID-19," Chaos, Solitons & Fractals 140, 110241 (2020).
3. K. Wu, D. Darcet, Q. Wang, and D. Sornette, "Generalized logistic growth modeling of the COVID-19 outbreak: comparing the dynamics in the 29 provinces in China and in the rest of the world," Nonlinear Dynamics 101, 1561–1581 (2020).
4. A. Cunha, F. da C. Batista, P. R. de L. Gianfelice, R. S. Oyarzabal, J. M. V. Grzybowski, and E. E. N. Macau, "epidWaves: A code for fitting multi-wave epidemic models," Software Impacts 14, 100391 (2022).
5. E. Pelinovsky, M. Kokoulina, A. Epifanova, A. Kurkin, O. Kurkina, M. Tang, E. Macau, and M. Kirillin, "Gompertz model in COVID-19 spreading simulation," Chaos, Solitons & Fractals 154, 111699 (2022).
6. H. S. Burkom, S. P. Murphy, and G. Shmueli, "Automated time series forecasting for biosurveillance," Statistics in Medicine 26(22), 4202–4218 (2007).
7. J. C. Brillman, T. Burr, D. Forslund, E. Joyce, R. Picard, and E. Umland, "Modeling emergency department visit patterns for infectious disease complaints: results and application to disease surveillance," BMC Medical Informatics and Decision Making 5(1), 4 (2005).
8. D. Lai, "Monitoring the SARS epidemic in China: a time series analysis," Journal of Data Science 3(3), 279–293 (2005).
9. J. Díaz-Hierro, J. J. Martín Martín, Á. Vilches Arenas, M. P. López Del Amo González, J. M. Patón Arévalo, and C. Varo González, "Evaluation of time-series models for forecasting demand for emergency health care services," Emergencias 24(3), 181–188 (2012).

10. S. Unkel, C. P. Farrington, P. H. Garthwaite, C. Robertson, and N. Andrews, "Statistical methods for the prospective detection of infectious disease outbreaks: a review," Journal of the Royal Statistical Society: Series A (Statistics in Society) 175(1), 49–82 (2012).
11. R. Kiang, F. Adimi, V. Soika, J. Nigro, P. Singhasivanon, J. Sirichaisinthop, S. Leemingsawat, C. Apiwathnasorn, and S. Looareesuwan, "Meteorological, environmental remote sensing and neural network analysis of the epidemiology of malaria transmission in Thailand," Geospatial Health 1(1), 71–84 (2006).
12. W. O. Kermack, A. G. McKendrick, "A contribution to the mathematical theory of epidemics," Proceedings of the Royal Society of London. Series A 115(772), 700-721 (1927).
13. Z. Zhao, X. Li, F. Liu, G. Zhu, C. Ma, and L. Wang, "Prediction of the COVID-19 spread in African countries and implications for prevention and controls: A case study in South Africa, Egypt, Algeria, Nigeria, Senegal and Kenya," Science of The Total Environment 729, 138959 (2020).
14. N. Ghaffarzadegan, H. Rahmandad, "Simulation-based estimation of the early spread of COVID-19 in Iran: actual versus confirmed cases," System Dynamics Review 36(1), 101–129 (2020).
15. S. Annas, M. I. Pratama, M. Rifandi, W. Sanusi, and S. Side, "Stability analysis and numerical simulation of SEIR model for pandemic COVID-19 spread in Indonesia," Chaos, Solitons & Fractals 139, 110072 (2020).
16. L. López, X. Rodo, "A modified SEIR model to predict the COVID-19 outbreak in Spain and Italy: simulating control scenarios and multi-scale epidemics," Results in Physics 21, 103746 (2021).
17. X. Yu, G. Qi, and J. Hu, "Analysis of second outbreak of COVID-19 after relaxation of control measures in India," Nonlinear Dynamics 106, 1149–1167 (2020).
18. S. Kurmi, U. Chouhan, "A multicompartment mathematical model to study the dynamic behaviour of COVID-19 using vaccination as control parameter," Nonlinear Dynamics 109(3), 2185–2201 (2022).
19. Y. Fang, Y. Nie, and M. Penny, "Transmission dynamics of the COVID-19 outbreak and effectiveness of government interventions: A data-driven analysis," Journal of Medical Virology 92(6), 645–659 (2020).
20. A. Temerev, L. Rozanova, O. Keiser, and J. Estill, "Geospatial model of COVID-19 spreading and vaccination with event Gillespie algorithm," Nonlinear Dynamics 109(3), 239–248 (2022).
21. C. Siettos, C. Anastassopoulou, L. Russo, C. Grigoras, and E. Mylonakis, "Modeling the 2014 Ebola virus epidemic–agent-based simulations, temporal analysis and future predictions for Liberia and Sierra-Leone," PLoS Currents 7, (2015).
22. H. Arduin, M. Domenech de Cellès, D. Guillemot, L. Watier, and L. Opatowski, "An agent-based model simulation of influenza interactions at the host level: insight into the influenza-related burden of pneumococcal infections," BMC Infectious Diseases 17(1), 382 (2017).
23. J. T. Tuomisto, J. Yrjölä, M. Kolehmainen, J. Bonsdorff, J. Pekkanen, and T. Tikkanen, "An agent-based epidemic model REINA for COVID-19 to identify destructive policies," medRxiv: 20047498 (2020).
24. N. Hoertel, M. Blachier, C. Blanco, M. Olfson, M. Massetti, F. Limosin, and H. Leleu, "Facing the COVID-19 epidemic in NYC: a stochastic agent-based model of various intervention strategies," medRxiv: 20076885 (2020).
25. J. R. Koo, A. R. Cook, M. Park, Y. Sun, H. Sun, J. T. Lim, C. Tam, and B. L. Dickens, "Interventions to mitigate early spread of SARS-CoV-2 in Singapore: A modelling study," The Lancet Infectious Diseases 20(6), 678–688 (2020).
26. G. España, S. Cavany, "NotreDame-FRED COVID-19 forecasts," GitHub (accessed 18 November 2022). [https://github.com/confunguido/covid19_ND_forecasting].
27. N. M. Ferguson, D. Laydon, G. Nedjati-Gilani, N. Imai, K. Ainslie, M. Baguelin, S. Bhatia, A. Boonyasiri, Z. Cucunubá, G. Cuomo-Dannenburg, A. Dighe, I. Dorigatti, H. Fu, K. Gaythorpe, W. Green, A. Hamlet, W. Hinsley, L. C. Okell, S. van Elsland, H. Thompson, R. Verity, E. Volz, H. Wang, Y. Wang, P. G. T. Walker, C. Walters, P. Winskill, C. Whittaker, C. A. Donnelly, S. Riley, and A. C. Ghani, "Impact of non-pharmaceutical interventions (NPIs) to reduce COVID-19 mortality and healthcare demand," Imperial College London (2020).
28. S. L. Chang, N. Harding, C. Zachreson, O. M. Cliff, and M. Prokopenko, "Modelling transmission and control of the COVID-19 pandemic in Australia," Nature Communications 11, 5710 (2020).
29. D. Kai, G.-P. Goldstein, A. Morgunov, V. Nangalia, and A. Rotkirch, "Universal masking is urgent in the COVID-19 pandemic: SEIR and agent based models, empirical validation, policy recommendations, arXiv:2004.13553 (2020).
30. J. A. Moreno López, B. Arregui García, P. Bentkowski, L. Bioglio, F. Pinotti, P.-Y. Boëlle, A. Barrat, V. Colizza, and C. Poletto, "Anatomy of digital contact tracing: Role of age, transmission setting, adoption, and case detection," Science Advances 7(15), eabd8750 (2021).
31. Md. S. Shamil, F. Farheen, N. Ibtehaz, I. M. Khan, and M. S Rahman, "An Agent-Based Modeling of COVID-19: Validation, Analysis, and Recommendations," Cognitive Computation (2021).
32. A. Aleta, D. Martin-Corral, A. Pastore y Piontti, M. Ajelli, M. Litvinova, M. Chinazzi, N. E. Dean, M. E. Halloran, I. M. Longini, S. Merler, A. Pentland, A. Vespignani, E. Moro, and Y. Moreno, "Modeling the impact of social distancing, testing, contact tracing and household quarantine on second-wave scenarios of the COVID-19 epidemic," medRxiv:20092841 (2020).

33. P. C. L. Silva, P. V. C. Batista, H. S. Lima, M. A. Alves, F. G. Guimarães, and R. C. P. Silva, "COVID-ABS: An agent-based model of COVID-19 epidemic to simulate health and economic effects of social distancing interventions," Chaos, Solitons & Fractals 139, 110088 (2020).
34. P. Keskinocak, B. E. Oruc, A. Baxter, J. Asplund, and N. Serban, "The impact of social distancing on COVID19 spread: State of Georgia case study," PLoS One 15(10), e0239798 (2020).
35. P. T. Gressman, J. R. Peck, "Simulating COVID-19 in a university environment," Mathematical Biosciences 328, 108436 (2020).
36. F. Ying, N. O'Clery, "Modelling COVID-19 transmission in supermarkets using an agent-based model," PLoS One 16(4), e0249821 (2021).
37. A. Truszkowska, B. Behring, J. Hasanyan, L. Zino, S. Butail, E. Caroppo, Z. Jiang, A. Rizzo, and M. Porfiri, "High-Resolution Agent-Based Modeling of COVID-19 Spreading in a Small Town," Advanced Theory and Simulations 4(3), 2000277 (2021).
38. C. Cheng, D. Zhang, D. Dang, J. Geng, P. Zhu, M. Yuan, R. Liang, H. Yang, Y. Jin, J. Xie, S. Chen, and G. Duan, "The incubation period of COVID-19: a global meta-analysis of 53 studies and a Chinese observation study of 11 545 patients," Infectious Diseases of Poverty 10(1), 119 (2021).
39. W. Dhouib, J. Maatoug, I. Ayouni, N. Zammit, R. Ghammem, S. B. Fredj, and H. Ghannem, "The incubation period during the pandemic of COVID-19: a systematic review and meta-analysis," Systematic Reviews 10, 101 (2021).
40. S. Paul, E. Lorin, "Distribution of incubation periods of COVID-19 in the Canadian context," Scientific Reports 11(1), 12569 (2021).
41. H. Xin, J. Y. Wong, C. Murphy, A. Yeung, S. Taslim Ali, P. Wu, and B. J. Cowling, "The Incubation Period Distribution of Coronavirus Disease 2019: A Systematic Review and Meta-analysis," Clinical Infectious Diseases 73(12), 2344–2352 (2021).
42. M. Kirillin, E. Sergeeva, A. Khilov, D. Kurakina, and N. Saperkin, "Monte Carlo simulation of the covid-19 spread in early and peak stages in different regions of the Russian Federation using an agent-based modelling," in Saratov Fall Meeting, Chinese-Russian workshop on Biophotonics and Bioimaging-2020 1, 71–74 (2020).
43. Coronavirus-monitor – interactive map of COVID-19 spread and statistics (accessed 06 April 2021). [https://coronavirus-monitor.info/country/russia/nizhegorodskaya-oblast/, in Russian].
44. Newsletter on the situation and measures taken to prevent the spread of diseases caused by the new coronavirus, (accessed 06 April 2021). [https://rospotrebnadzor.ru/about/info/news/news_details.php?ELEMENT_ID=19030&sphrase_id=4390258, in Russian].
45. E. Mathieu, H. Ritchie, L. Rodés-Guirao, C. Appel, D. Gavrilov, C. Giattino, J. Hasell, B. Macdonald, S. Dattani, D. Beltekian, E. Ortiz-Ospina, and M. Roser, "Coronavirus Pandemic (COVID-19)," Our World in Data (accessed 19 April 2022). [https://ourworldindata.org/mortality-risk-covid].
46. E. Dong, H. Du, and L. Gardner, "An interactive web-based dashboard to track COVID-19 in real time," Lancet Infectious Diseases 20(5), 533–534 (2020).

Concentration Dependence of Optical Transmission and Extinction of Different Diatom Cultures

Julijana Cvjetinovic[1*], Sergei A. Perkov[1], Maxim A. Kurochkin[1], Igor S. Sergeev[1,2], Sergey V. German[1], Yekaterina D. Bedoshvili[3,1], Nickolai A. Davidovich[4,1], Alexander M. Korsunsky[5], and Dmitry A. Gorin[1]

[1] Center for Photonic Science and Engineering, Skolkovo Institute of Science and Technology, 30 Bolshoy Boulevard, bld. 1, Moscow 121205, Russia

[2] Laboratory of Laser Biomedicine, FSRC "Crystallography and Photonics" RAS, 59 Leninskiy Prospekt, Moscow 119333, Russia

[3] Limnological Institute, Siberian Branch, Russian Academy of Sciences, 3 Ulan-Batorskaya str., Irkutsk 664033, Russia

[4] T. I. Vyazemsky Karadag Scientific Station, Natural Reserve of the Russian Academy of Sciences, Kurortnoe, Feodosiya 98188, Russia

[5] Department of Engineering Science, University of Oxford, Oxford, OX1 3PJ, United Kingdom

***e-mail:** julijana.cvjetinovic@skoltech.ru

Abstract. Diatoms are unicellular microalgae enclosed in a hierarchically structured silica cell wall that play a significant role in maintaining the health of the planet's ecosystem. As one of the main photosynthesizers, they are responsible for 20–25% of the world's oxygen release and carbon fixation. In order to develop technologies for the efficient extraction of carbon dioxide, for example, using bioreactors that provide optimal conditions for the growth of diatoms, it is also necessary to effectively track the diatom lifecycle, as well as control parameters that affect their growth. Here we offer a simple device consisting of LED illumination with a central wavelength of 505 nm that allows to monitor changes in diatom concentrations. We examined marine centric and freshwater pennate diatom strains with different morphologies, sizes, and volumes and obtained a linear dependence of the measured transmission on the concentration. The results were compared with the spectrophotometric approach, which showed a higher inaccuracy with respect to the linear fit. We believe that such an optical setup can be used to solve the problems of continuous flow monitoring of algae both in bioreactors as well as in their natural environment. © 2023 Journal of Biomedical Photonics & Engineering.

Keywords: diatom algae; optical setup; spectrophotometry; fluorescence; microscopy.

Paper #3567 received 02 Dec 2022; revised manuscript received 06 Dec 2022; accepted for publication 07 Dec 2022; published online 30 Jan 2023. doi: 10.18287/JBPE23.09.010303.

1 Introduction

Diatoms are the most numerous representatives of phytoplankton, having appeared nearly 200 million years ago [1]. These exquisite single-celled microalgae thrive wherever there is light, water, essential gases and nutrients and play an immense role in keeping the planet's ecosystem working. As one of the main photosynthesizers, they produce about 20–25% of the atmospheric oxygen and form up to a quarter of the organic material [2]. Their most important feature is a highly porous silica cell wall called frustule, whose intricate patterns and sophisticated designs have captured the attention of researchers for centuries [3, 4]. The silica frustule consists of two halves (valves): the epitheca (the upper part), and the hypotheca (the lower part), joined together by siliceous girdle bands. Diatoms (phylum Bacillariophyta) consists of three classes Coscinodiscophyceae (centric species with radial valve symmetry), Mediophyceae (centric species with radial and bipolar valve symmetry), and the bilaterally symmetric class Bacillariophyceae [5]. Diatoms are extremely diverse, with conservative estimates ranging from 100,000

to 200,000 species, making them one of the most species-rich eukaryotic lineages [6]. Their size ranges from 2 to 1500 μm, although there are a few larger species. In terms of the number of species, pennate diatoms dominate over the centric ones [7]. On the other hand, centric diatoms, which are mainly planktonic, create the bulk of primary production.

Despite their crucial role in the ecosystem, the use of diatoms has previously been almost exclusively limited to academic research. However, owing to their unique structure, abundance, and properties such as high porosity, large surface area, ease of modification, thermal stability, good optical and mechanical properties, efforts have been made to start exploring them for commercial and industrial applications. Over the past 30 years, the potential of diatom frustules as a novel functional material for bio-manufacturing and use as gas sensors, drug delivery systems, biosensors, solar cells, SERS platforms, battery electrodes have been examined [8–12]. Moreover, they are indicators of water quality and a source of bioactive substances, such as lipids, omega-3 fatty acids, and proteins [13, 14]. Nowadays, there is a considerable need for optimization of algae bioreactors, both in terms of production efficiency of target algae cultures, and in terms of efficient monitoring of the algal life cycle for cultivation protocols optimization. The growth of diatoms is traditionally assessed by obtaining growth curves upon counting cells under a microscope in selected aliquots. However, many species are prone to aggregation and clustering, therefore, after several days of cultivation, their counting becomes very difficult, especially in the case of small benthic cultures. Probably, the main difficulty in counting cells in a microvolume in a well plate is the impossibility of selecting adequate aliquots, so growth curves are usually presented with rather large technical errors. Diatom cultivation in large bioreactors and subsequent selection of probes would lead to even greater errors.

In order to facilitate the collection and extraction of various bioactive compounds from diatoms, they must not only be grown correctly under optimal conditions, but also effectively monitored. The optical probe methods can selectively analyze the state of diatom cells and monitor their life cycle based on the absorbance and fluorescence of the main light-harvesting pigments: chlorophyll a, chlorophyll c and carotenoids [15]. Chlorophyll a absorbs energy in the violet-blue and orange-red regions of the spectrum, while chlorophyll c mainly absorbs blue and red light [16]. Fucoxanthin, the main carotenoid in diatoms, absorbs in the blue-green part of the spectrum (500–530 nm). Diatoms can be easily studied and visualized with a variety of optical methods, ranging from the historically first light microscopy to modern methods such as fluorescence lifetime imaging and optoacoustic microscopy, which allow studying not only individual cells of diatoms, but also colonies [17]. Moreover, the photoacoustic method in combination with in situ fluorescence imaging has been used to monitor the growth of diatoms during long-term cultivation in the laboratory conditions based on the absorption and fluorescence signals of the pigments [18–21]. These methods are also promising for studying the activity of these microorganisms in the natural environment, as well as for monitoring their growth in bioreactors or aquaculture installations. Among the current solutions for the bioreactors, some do not allow precise control of growth conditions, as well as continuous monitoring without manual probing [22] and others are designed only for chlorophyll content monitoring [23], whereas the cultivation of diatoms requires monitoring of additional parameters, such as carotenoid content. Moreover, Voznesenskiy et al. showed that temperature dependence of fluorescence intensity of chlorophyll a reflects the specific processes in cells of different microalgae species [24].

In this work, an optical setup consisting of LED illumination with a central wavelength of 505 nm was developed to monitor changes in diatom concentrations. Here, we have selected marine centric and freshwater pennate diatom cultures with different morphologies and sizes to prove the versatility of our method and compared it with results obtained using a commercially available spectrophotometer. We believe that this setup can be used in the future as a component in bioreactors as well as open water bodies for the purpose of continuous flow monitoring of algae.

2 Materials and Methods

2.1 Diatom Cell Cultures

Here we studied seven different freshwater pennate and marine centric diatom cultures. Pennate diatom cultures (*Asterionella formosa* – strain BZ 33, *Amphipleura* sp. – strain Ov 466, *Hannaea baicalensis* – strain BK 479, *Ulnaria acus* – strain 15k 595) were isolated from a natural population in Lake Baikal and cultivated in the DM medium [25] at 10 °C under natural light and day–night cycle. Marine centric diatoms *Biddulphiopsis titiana* (strain 0.0212-OH, Atlantic ocean), *Coscinodiscus oculus-iridis* (strain 0.1211-OD, Tsushima Strait), *Coscinodiscus sp.* (strain 21.0407-OA, Black sea) were cultivated in ESAW medium prepared according to a modified recipe as described by Polyakova et al. [26] with salinity of ca. 36‰ (0.0212-OH, 0.1211-OD) and 20‰ (21.0407-OA). Cell culture flasks "T-25" (Eppendorf, Germany) with diatom cultures were kept on a windowsill of the laboratory at room temperature under natural light. Sample probes were taken for measurements during the stationary phase of growth.

2.2 Visualization of Diatom Algae

Diatoms were visualized and counted under the inverted luminescent microscope NIB-FL (LOMO-MA, Russia) using PH10x and PH40× objectives. Images were taken with an UltraHD-4k (35k/s) camera. To determine the concentration of cultures, the flasks with diatoms were thoroughly shaken and 10 μl of each culture was applied to a glass slide in triplicate. For fluorescent visualization, 100 μl of each diatom strain was placed in the individual

well of 96-well plate (CellCarrier Ultra, PerkinElmer, USA) and imaged with a ×20 and ×60 magnification objectives using the Operetta High Content Imaging System (Perkin Elmer, USA) in the fluorescence mode. The chlorophyll autofluorescence was excited at 410–430 nm, while the emission was registered at 650–700 nm. The obtained images were processed using Harmony 4.1 software (Perkin Elmer, USA).

2.3 Experimental Setup for Optical Monitoring

An optical setup developed to monitor changes in algae concentrations is shown in Fig. 1(a–c). A light emitting diode (LED) with a central wavelength of 505 nm was used as a light source. This wavelength was chosen to match the absorption maximum of carotenoids [27] presented in diatoms, such as fucoxanthin and beta-carotene [16]. The emission spectrum of LED is shown in Fig. 1(d). Emitted light was coupled in a multimode optical fiber with 105 µm core for spatial filtering then collimated by f = 7.5 mm aspheric lens, passed through plastic cuvette with analyzed volume of algae suspended in nutrient medium and measured by a linear photodiode (PD) with preamplifier (OPT101P, Texas Instruments, USA). The data transfer between the optical system and the personal computer was performed using a microcontroller Arduino Nano. The LED and the photodiode were powered by a 5 V voltage source. The diameter of the probe light beam was 1.5 mm. The PD square shaped photosensitive area size was 1.7×1.7 mm. Discretization frequency for Arduino analog-to-digital converter (ADC) was set to 100 Hz. A python code was used to read the data from Arduino, and calculate mean value and standard deviation over 12000 measurements during 2 min. To avoid external illumination influence, the optical setup was covered with a non-transparent enclosure.

LED illumination was coupled into an optical fiber by placing the end of the optical fiber to the LED light-emitting crystal at a distance of 200 µm. For this purpose, a 350 µm diameter hole was drilled in the LED transparent body under the optical control of a stereomicroscope ADF S645. An optical fiber was placed in the LED drilled hole and fixed using epoxy resin as shown on Fig. 1(b). The resulting output power of the LED light output of the collimating aspheric lens was 8.5 µW. Mounting elements of the optical system were produced by photopolymer printing approach.

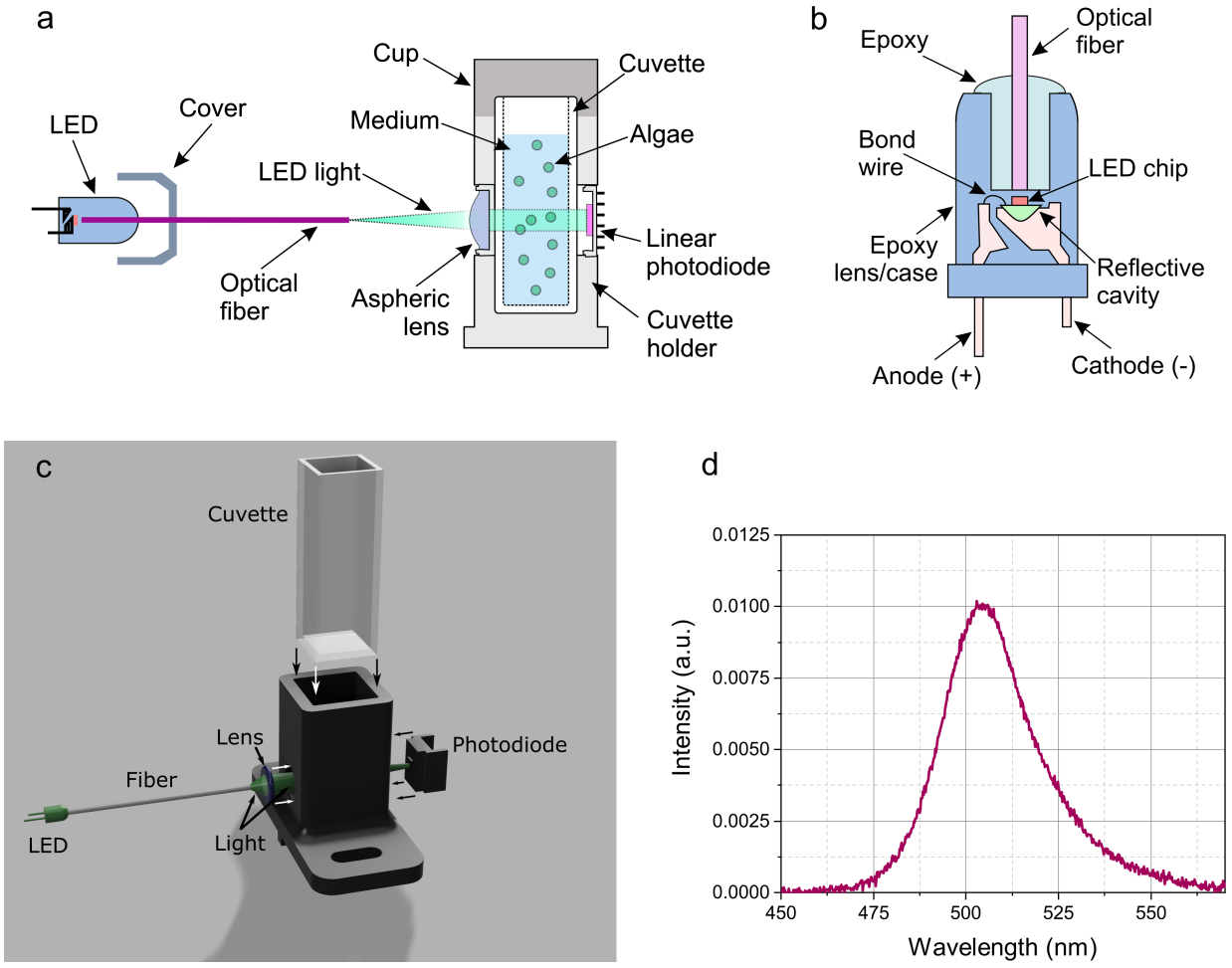


Fig. 1 Experimental setup for monitoring changes in the diatom algae concentration. (a) Artistic representation of an optical system for measuring the transmission of algae in a nutrient medium depending on their fractional dilution. (b) Direct LED light coupling in multimode optical fiber. (c) Schematic representation of the experimental setup key components for transmission measurements. (d) Emission spectrum of LED.

Table 1 Size and morphology of the studied diatom cultures.

No.	Diatom culture (strain number)	Type	Shape	Diameter, μm	Length (height), μm	Volume, μm^3
1	*Biddulphiopsis titiana* (0.0212-OH)	marine centric	rectangular with round corners	132	255	$3.5 \cdot 10^6$
2	*Coscinodiscus oculus-iridis* (0.1211-OD)	marine centric	disc-shaped	31	10	$7.5 \cdot 10^3$
3	*Coscinodiscus* sp. (21.0407-OA)	marine centric	cylindrical	27	36	$2.1 \cdot 10^4$
4	*Amphipleura sp.* (Ov 466)	freshwater pennate	elliptical	7	57	$2.2 \cdot 10^3$
5	*Hannaea baicalensis* (BK 479)	freshwater pennate	banana-shaped	7	65	$2.5 \cdot 10^3$
6	*Asterionella formosa* (BZ 33)	freshwater pennate	single: elongated, star-shaped colonies	5	85	$1.7 \cdot 10^3$
7	*Ulnaria acus* (15k 595)	freshwater pennate	needle-shaped	5	175	$3.4 \cdot 10^3$

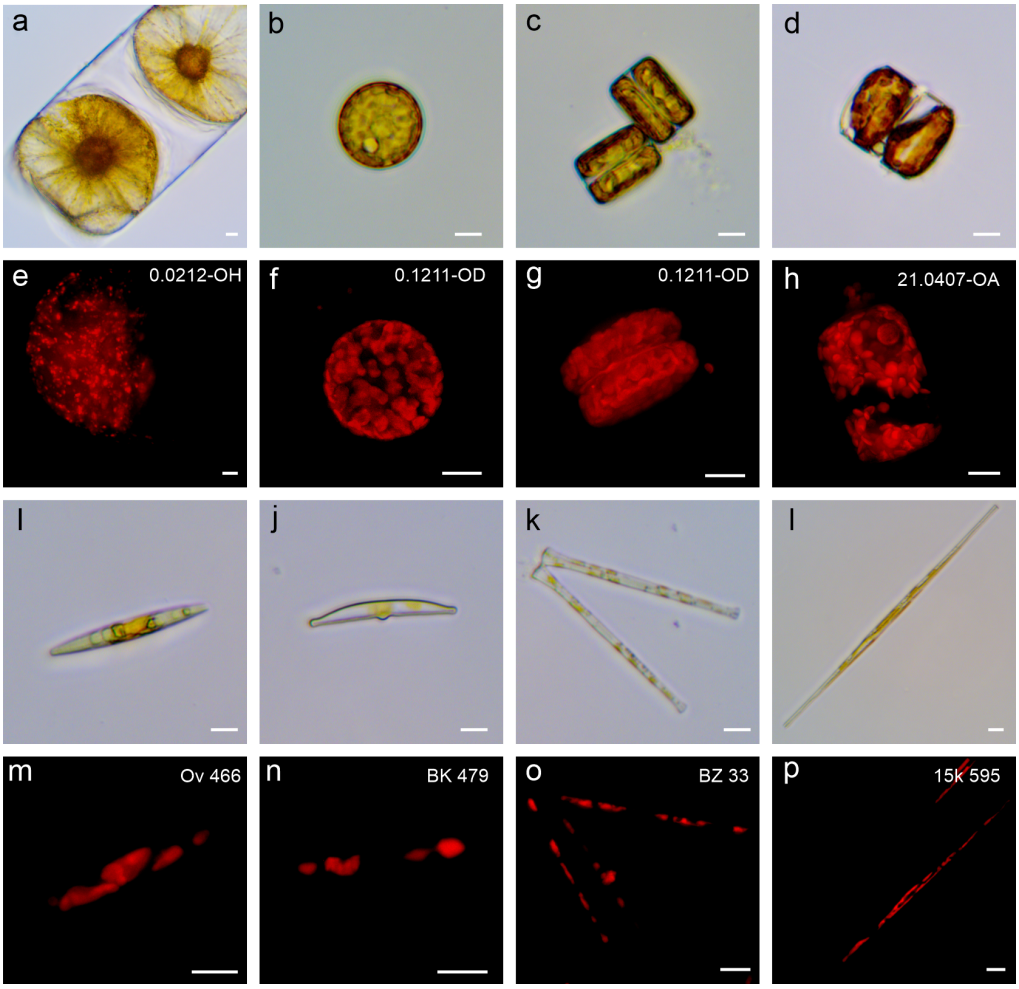


Fig. 2 Brightfield microscopy images of marine centric diatoms: (a) *Biddulphiopsis titiana* (0.0212-OH), *Coscinodiscus oculus-iridis* (0.1211-OD): (b) top view, (c) side view, (d) *Coscinodiscus* sp. (21.0407-OA). Fluorescence images of marine centric diatoms: (e) *Biddulphiopsis titiana* (0.0212-OH), *Coscinodiscus oculus-iridis* (0.1211-OD): (f) top view, (g) side view, (h) *Coscinodiscus* sp. (21.0407-OA). Brightfield microscopy images of freshwater pennate diatoms: (i) *Amphipleura* sp. (Ov 466), (j) *Hannaea baicalensis* (BK 479), (k) *Asterionella formosa* (BZ 33), (l) *Ulnaria acus* (15k 595). Fluorescence images of freshwater pennate diatoms: (m) *Amphipleura* sp. (Ov 466), (n) *Hannaea baicalensis* (BK 479), (o) *Asterionella formosa* (BZ 33), (p) *Ulnaria acus* (15k 595).

2.4 Optical Measurements and Spectrophotometry

To verify cell counting ability of the experimental setup, 7 diatom strains were examined. For optical measurements, 1.5 mL of each strain were put into a plastic cuvette in the experimental setup. A custom python script was used to record light intensity values for 2 min, and, subsequently, average them over measurement time and calculate standard deviation. Then, for each strain the sample was diluted ×1.154 times. This new sample was placed into the experimental setup, and new light intensity values were recorded. This procedure of dilution and measurement was repeated 11 times for each strain. The well-plate with the same 12 dilutions for each of 7 diatoms strains was placed into a spectrophotometer Tecan Infinite M Nano+ (Tecan Trading AG, Männedorf, Switzerland). For all the initial diatoms concentrations extinction and fluorescence spectra (the excitation wavelength was set to 430 nm) were measured. Then for each sample extinction value and fluorescence intensity were measured. Extinction was measured at the wavelength of 505 nm. The fluorescence intensity was registered at 680 nm, when the excitation wavelength was set to 430 nm.

3 Results and Discussion

3.1 Diatom Algae: Description and Visualization

In this work, we studied 3 marine centric diatom strains and 4 pennate cultures from Lake Baikal with different sizes and morphologies (Table 1, Fig. 2). The diameter and length or height were obtained from brightfield images (Fig. 2), while the volume was calculated for each strain as $V = \pi (d/2)^2 l$, where d is a diameter, l is a length, approximating diatom cells as cylinders.

Brightfield images of centric (Figs. 2(a–d)) and pennate diatom cells (Figs. 2(i–l)) show how the chloroplast color changes from yellow to golden brown depending on the strain. Fluorescence images demonstrate distribution of chlorophyll throughout the cells (Figs. 2(e–h, m–p). In the case of *Biddulphiopsis titiana* (0.0212-OH), whose cell size is around 250 µm, chloroplasts partly fill the volume from both sides (Fig. 2(e)). On the other hand, chloroplasts in *Coscinodiscus* species (0.1211-OD, 21.0407-OA) are more densely packed and have oval shape (Figs. 2(f–h)). Figs. 2(c, g) show the side view of C*oscinodiscus oculus-iridis* in the process of division. Chloroplasts in the case of freshwater cultures *Amphipleura* sp. (Ov 466) and *Ulnaria acus* (15k 595) occupy most of the cells (Fig. 2(m, p)), while in *Hannaea baicalensis* (BK 479) and *Asterionella formosa* (BZ 33) they are distributed in the form of grains (Fig. 2(n, o)).

3.2 Optical Measurements and Spectrophotometry

The results of measurements obtained using experimental setup described in Fig. 1 are demonstrated in Fig. 3. For each diatom strain measured light intensity values were normalized by the nutrient medium light intensity values, and the concentration values were multiplied by the number of cells in mL, calculated on the microscope for each diatom strain. Standard deviation, that was calculated from 12000 measurements for each sample, cannot be seen on graph because error bars do not exceed the size of a dot. The observed dependence of the measured light intensity on the relative concentration of diatoms was approximated by the linear fit for each diatoms strain. It can be seen that all values have high correlation with the linear fit, and are in a good agreement with Bouguer-Beer-Lambert Law, which states that sample's extinction (light attenuation) has linear dependence on light absorber's concentration:

$$A = \varepsilon l C + G_S, \tag{1}$$

where A is extinction, ε is molar extinction coefficient, l is optical path, C is concentration of chromophores, presented in diatoms, G_s is the attenuation factor, accounting for scattering and geometry of particles [28].

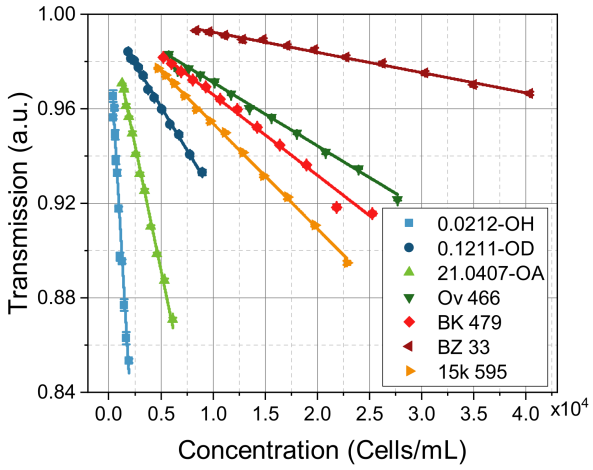


Fig. 3 Optical measurements of diatom cultures. Dependence of light intensity on the relative diatom cell concentrations. Light intensity was normalized on the measurements of nutrient medium. Scatter plot represents measured values, solid lines represent linear fit.

To demonstrate the advantages of our system over conventional spectrophotometric approach and investigate opportunities for future development of the device, the extinction and fluorescence intensity measurements were made. Fig. 4(a) demonstrates extinction spectra for initial concentrations of 7 diatom strains. The dependence of diatoms extinction on the concentration is demonstrated in Fig. 4(b). For all strains measured values were approximated by the linear fit. The

coefficients of determination (COD) for all linear fits are shown in Table 2. It can be seen, that for all strains spectrophotometric measurements demonstrate lower COD values, than optical measurements on the custom setup, which indicates higher accuracy of the latter. This can be explained by the difference in the sensing volume. According to the manufacturer of Tecan Infinite M Nano+, the spot size of the absorbance light beam is 0.7 mm in diameter. The optical path for 200 µL sample is 6.25 mm, thus the sensing volume is V = 2.405 mm^3. In contrast to that, our setup has a spot size of light beam scaled to 1.5 mm in diameter, and the optical path is 10 mm. Therefore, the sensing volume in our setup is V = 17.67 mm^3, which is 7 times greater than in spectrophotometer. This allows our setup to average values more accurately even for small diatom cell concentrations.

Table 2 Comparison of the coefficient of determination (COD) for spectrophotometric measurements with optical measurements on the custom device.

Diatom strain	Spectrophotometer, COD	Custom device, COD
0.0212-OH	0.840	0.981
0.1211-OD	0.954	0.997
21.0407-OA	0.983	0.998
Ov 466	0.929	0.996
BK 479	0.975	0.993
BZ 33	0.638	0.995
15k 595	0.901	0.999

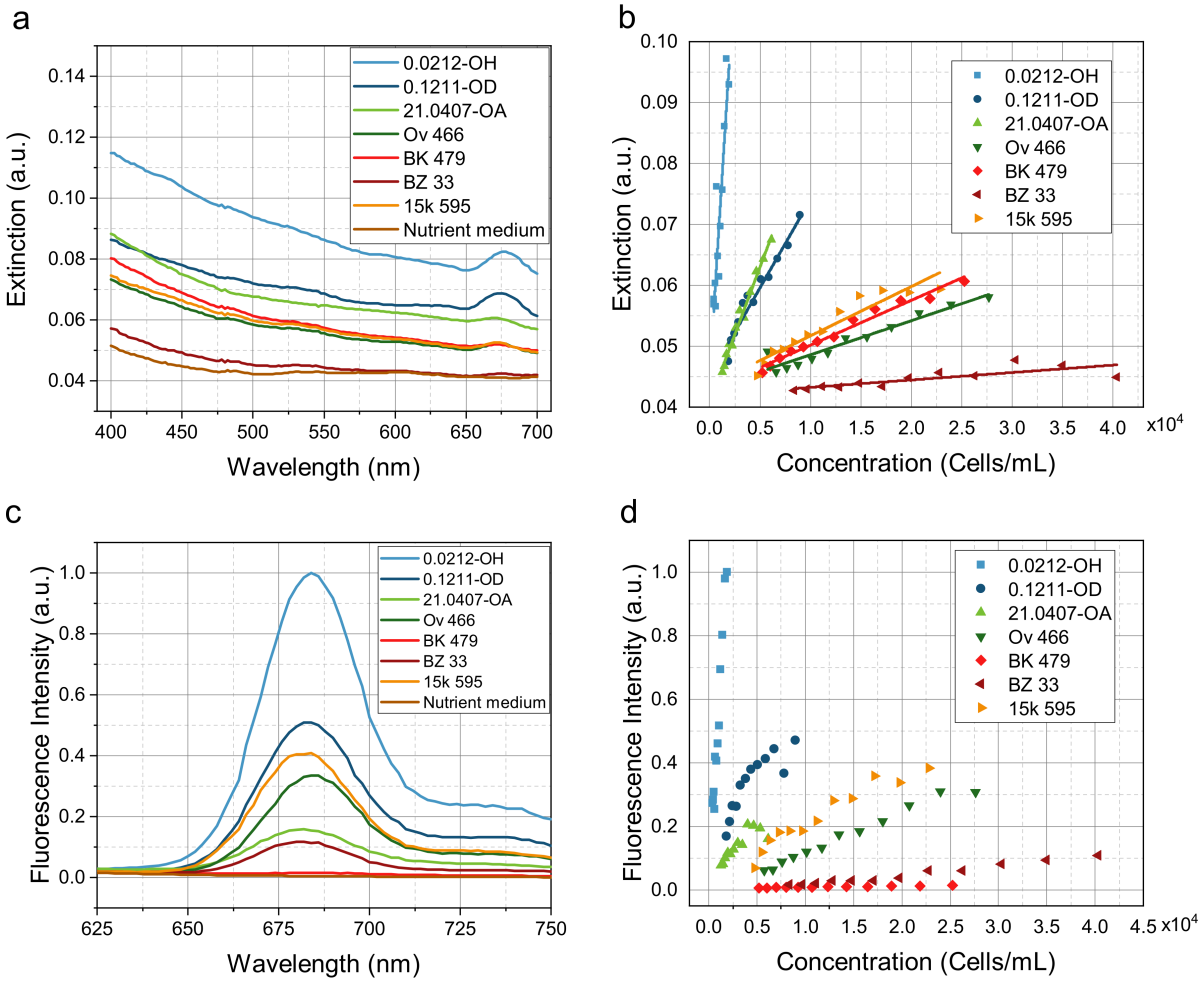


Fig. 4 Spectrophotometric and fluorescence measurements of diatoms. (a) Extinction spectra. (b) Dependence of extinction (λ = 505 nm) on the diatom concentration. Scatter plot represents extinction values normalized on the nutrient medium extinction. Solid lines represent linear fit. (c) Fluorescence intensity spectra. Excitation wavelength: 430 nm. (d) Dependence of fluorescence intensity (λ_{ex} = 430 nm, λ_{em} = 680 nm) on the diatom concentration. Scatter plot represents fluorescence intensity values normalized on the nutrient medium values.

Fig. 4(c) demonstrates fluorescence intensity spectra for initial concentrations of 7 diatom strains (excitation wavelength: 430 nm). It can be seen that all strains exhibit fluorescence except for nutrient medium and BK 479 strain. This observation correlates with the absence of extinction peak of chlorophyll *c* in BK 479, that should be located near 680 nm. Brightfield microscopic images and the growth curve allow to assume, that this strain was in the transition between stationary growth phase and the last (death) phase during measurements. The composition and quantity of pigments is not constant and depends on the intensity of light, the spectral composition of light, the content of nutritional elements in water, as well as on the growth phase and the characteristics of diatom vital activity [16, 29]. The amount of chlorophyll somewhat decreases at the end of the stationary phase of growth without renewal of the medium. Thus, fluorescence and extinction measurements of diatoms at the wavelength of 680 nm might be a potential marker of the diatom growth phase.

Also, Fig. 4(d) shows the dependence of fluorescence intensity on the concentration for 7 diatom strains (excitation wavelength: 430 nm, emission wavelength: 680 nm). One can observe, that marine centric diatom cultures (strain No. 0.0212-OH, 0.1211-OD and 21.0407-OA) exhibit stronger fluorescence dependence on concentration than pennate diatom cultures (strain No. 15k 595, Ov 466, BK 479, BZ 33).

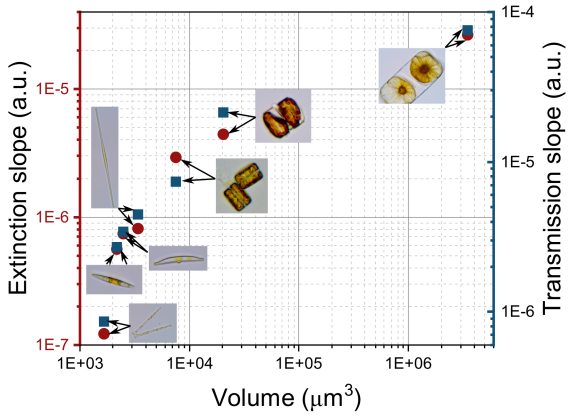


Fig. 5 The dependence of linear fit slopes on the diameter of diatom cells. The red circles represent slopes of linear fit in extinction measurements. The blue squares represent absolute values of slopes of linear fit in transmission measurements on the custom-made setup described in Fig. 1.

It can be noted from Figs. 3 and 4, that slopes of linear fits differ between diatom strains. To be more precise, slope of linear fit is connected to geometrical parameters of a strain, and this dependence is demonstrated in Fig. 5. One can clearly see the monotonic dependence of the slope on the volume of diatom cells, that was extracted from the Table 1. The relation between slopes of linear fits and diatom volume is similar in both extinction and transmission measurements and mostly determined by the extinction coefficient, that combines absorption and scattering properties of diatoms. This knowledge could be used for more accurate tuning of the photodetector sensitivity for monitoring of each diatom strain and for characterization of diatom biomass.

4 Conclusions

In this work capabilities of transmission measurements at the wavelength of 505 nm for 7 diatom strains were demonstrated and compared to the spectrophotometric approach. As a result, the linear dependence of measured transmission on the diatom concentration was observed with high accuracy for all 7 diatom strains. However, for spectrophotometric extinction measurements this dependence exhibits higher inaccuracy when compared to linear fit. Fluorescence measurements suggest that transmission measurements at the wavelength of 680 nm and fluorescence measurements with excitation wavelength of 430 nm and emission wavelength of 680 nm can improve understanding of diatoms life cycles and current state of diatoms in the bioreactor. Also, a monotonic dependence of linear fit slopes for both extinction and transmission measurements on the diatom volume was demonstrated. Thus, it can be concluded that described approach is promising for continuous monitoring of diatoms in bioreactors, and can be improved with addition of transmission measurements at the wavelength of 680 nm and fluorescence measurements with the same emission wavelength, as well as fine tuning of a photodetector sensitivity based on the obtained dependencies of the linear fits on the diatom volume.

Disclosures

The authors declare that there is no conflict of interest.

Acknowledgements

The work was supported by Russian Science Foundation (RSF) grant No. 22-14-00209. The investigated marine centric diatom strains were isolated and introduced in a culture thanks to the project number 121032300019–0, Study of Fundamental Physical, Physiological, Biochemical, Reproductive, Population, and Behavioural Characteristics of Marine Hydrobionts funded by the Ministry of Science and Higher Education of the Russian Federation.

References

1. M. J. Behrenfeld, K. H. Halsey, E. Boss, L. Karp-Boss, A. J. Milligan, and G. Peers, "Thoughts on the evolution and ecological niche of diatoms," Ecological Monographs 91(3), e01457 (2021).
2. S. Malviya, E. Scalco, S. Audic, F. Vincent, A. Veluchamy, J. Poulain, P. Wincker, D. Iudicone, C. de Vargas, L. Bittner, A. Zingone, and C. Bowler, "Insights into global diatom distribution and diversity in the world's ocean," Proceedings of the National Academy of Sciences 113(11), E1516–E1525 (2016).
3. E. De Tommasi, J. Gielis, and A. Rogato, "Diatom Frustule Morphogenesis and Function: a Multidisciplinary Survey," Marine Genomics 35, 1–18 (2017).
4. A. M. Korsunsky, P. V. Sapozhnikov, J. Everaerts, and A. I. Salimon, "Nature's neat nanostructuration: The fascinating frustules of diatom algae," Materials Today 22, 159–160 (2019).
5. M. D.Guiry, G. M. Guiry, AlgaeBase. World-wide electronic publication, National University of Ireland, Galway (accessed 1 December 2022). [https://www.algaebase.org].
6. R. Gordon, D. Losic, M. A. Tiffany, S. S. Nagy, and F. A. S. Sterrenburg, "The Glass Menagerie: diatoms for novel applications in nanotechnology," Trends in Biotechnology 27(2), 116–127(2009).
7. N. A. Davidovich, O. I, Davidovich, Reproductive Biology of Diatoms, ARIAL, LLC, Simferopol (2022). ISBN 978-5-907587-63-2 [in Russian].
8. N. Sharma, D. P. Simon, A. M. Diaz-Garza, E. Fantino, A. Messaabi, F. Meddeb-Mouelhi, H. Germain, and I. Desgagné-Penix, "Diatoms Biotechnology: Various Industrial Applications for a Greener Tomorrow," Frontiers in Marine Science 8, 636613 (2021).
9. A. Bozarth, U.-G. Maier, and S. Zauner, "Diatoms in biotechnology: Modern tools and applications," Applied Microbiology and Biotechnology 82(2), 195–201 (2009).
10. M. Mishra, A. P. Arukha, T. Bashir, D. Yadav, and G. B. K. S. Prasad, "All new faces of diatoms: Potential source of nanomaterials and beyond," Frontiers in Microbiology 8, 1239 (2017).
11. A. M. Korsunsky, Y. D. Bedoshvili, J. Cvjetinovic, P. Aggrey, K. I. Dragnevski, D. A. Gorin, A. I. Salimon, and Y. V. Likhoshway, "Siliceous diatom frustules – A smart nanotechnology platform," Materials Today: Proceedings 33(4), 2032–2040 (2020).
12. P. Aggrey, M. Nartey, Y. Kan, J. Cvjetinovic, A. Andrews, A. I. Salimon, K. I. Dragnevski, and A. M. Korsunsky, "On the diatomite-based nanostructure-preserving material synthesis for energy applications," RSC Advances 11(51), 31884–31922 (2021).
13. H.-Y. Li, Y. Lu, J.-W. Zheng, W.-D. Yang, and J.-S. Liu, "Biochemical and genetic engineering of diatoms for polyunsaturated fatty acid biosynthesis," Marine Drugs 12(1), 153–166 (2014).
14. I. Barkia, L. Al-Haj, A. Abdul Hamid, M. Zakaria, N. Saari, and F. Zadjali, "Indigenous marine diatoms as novel sources of bioactive peptides with antihypertensive and antioxidant properties," International Journal of Food Science & Technology 54(5), 1514–1522 (2019).
15. A. Burson, M. Stomp, E. Greenwell, J. Grosse, and J. Huisman, "Competition for nutrients and light: testing advances in resource competition with a natural phytoplankton community," Ecology 99(5), 1108–1118 (2018).
16. P. Kuczynska, M. Jemiola-Rzeminska, and K. Strzalka, "Photosynthetic pigments in diatoms," Marine Drugs 13(9), 5847–5881 (2015).
17. J. Cvjetinovic, A. I. Salimon, M. V. Novoselova, P. V. Sapozhnikov, E. A. Shirshin, A. M. Yashchenok, O. Yu. Kalinina, A. M. Korsunsky, and D. A. Gorin, "Photoacoustic and fluorescence lifetime imaging of diatoms," Photoacoustics 18, 100171 (2020).
18. J. Cvjetinovic, Y. Bedoshvili, D. Nozdriukhin, O. Efimova, A. Salimon, N. Volokitina, A. Korsunsky, and D. Gorin, "In situ fluorescence / photoacoustic monitoring of diatom algae," Proceedings of SPIE 11641, 116410G (2021).
19. J. Cvjetinovic, A. I. Salimon, M. V. Novoselova, P. V. Sapozhnikov, O. Y. Kalinina, A. M. Korsunsky, and D. A. Gorin, "Photoacoustic visualization of diatom algae," Limnology and Freshwater Biology 3(4), 779-780 (2020).
20. J. Cvjetinovic, Y. D. Bedoshvili, D. V. Nozdriukhin, A. I. Salimon, A. M. Korsunsky, and D. A. Gorin, "Photonic tools for evaluating the growth of diatom colonies during long-term batch cultivation," Journal of Physics: Conference Series 2172(1), 012011 (2022).
21. J. Cvjetinovic, D. V. Nozdriukhin, Y. D. Bedoshvili, A. I. Salimon, A. M. Korsunsky, and D. A. Gorin, "Assessment of diatom growth using fluorescence imaging," Journal of Physics: Conference Series 1984, 012017 (2021).
22. L. Rodolfi, N. Biondi, A. Guccione, N. Bassi, M. D'Ottavio, G. Arganaraz, and M. R. Tredici, "Oil and eicosapentaenoic acid production by the diatom Phaeodactylum tricornutum cultivated outdoors in Green Wall Panel (GWP®) reactors," Biotechnology and Bioengineering 114(10), 2204–2210 (2017).
23. T. Yu. Plyusnina, S. S. Khruschev, N. S. Degtereva, I. V. Konyukhov, A. E. Solovchenko, M. Kouzmanova, V. N. Goltsev, G. Yu. Riznichenko, and A. B. Rubin, "Gradual changes in the photosynthetic apparatus triggered by nitrogen depletion during microalgae cultivation in photobioreactor," Photosynthetica 58(Special Issue), 443–451 (2020).

24. S. S. Voznesenskiy, E. L. Gamayunov, A. Yu. Popik, Zh. V. Markina, and T. Yu. Orlova, "Temperature dependence of the parameters of laser-induced fluorescence and species composition of phytoplankton: The theory and the experiments," Algal Research 44, 101719 (2019).
25. A. S. Thompson, J. C. Rhodes, and I. Pettman, Culture Collection of Algae and Protozoa: Catalogue of Strains, Amblesibe, UK (1998).
26. S. L. Polyakova, O. I. Davidovich, Y. A. Podunay, and N. A. Davidovich, "Modification of the ESAW culture medium used for cultivation of marine diatoms," Marine Biological Journal 3(2), 73–80 (2018).
27. R. Croce, H. Van Amerongen, "Natural strategies for photosynthetic light harvesting," Nature Chemical Biology 10, 492–501 (2014).
28. V. V. Tuchin (Ed.), Tissue Optics: Light Scattering Methods and Instruments for Medical Diagnosis, 3rd Ed., SPIE Digital Library, USA (2015). ISBN: 9781628415162.
29. E. S. Holdsworth, "Effect of growth factors and light quality on the growth, pigmentation and photosynthesis of two diatoms, Thalassiosira gravida and Phaeodactylum tricornutum," Marine Biology 86, 253–262 (1985).

Inhibition of Self-Assembling Peptide Fibrils Formation Using Thioflavin T as a Photosensitizer

Tatiana N. Tikhonova[1*], Anna A. Rubekina[1], Viktor A. Vorobev[1], Ekaterina A. Mefodeva[1], Eugene G. Maksimov[2], Yuri M. Efremov[3,4], Maxim E. Darvin[5], Peter S. Timashev[3,4], Peter V. Gorelkin[6], Alexander S. Erofeev[6], Nikolay N. Sysoev[1], and Evgeny A. Shirshin[1+]

[1] Department of Physics, M.V. Lomonosov Moscow State University, 1/2 Leninskie gory, Moscow 119991, Russia
[2] Department of Biophysics, Faculty of Biology, M.V. Lomonosov Moscow State University, 1/24 Leninskie gory, Moscow 119991, Russia
[3] World-Class Research Center "Digital biodesign and personalized healthcare", Sechenov First Moscow State Medical University, 8–2 Trubetskaya str., Moscow 119991, Russia
[4] Institute for Regenerative Medicine, Sechenov University, 8–2 Trubetskaya str., Moscow 119991, Russia
[5] Department of Dermatology, Venerology and Allergology, Center of Experimental and Applied Cutaneous Physiology, Charité–Universitäts medizin Berlin, Corporate Member of Freie Universität Berlin and Humboldt-Universität zu Berlin, Charitéplatz 1, Berlin 10117, Germany
[6] National University of Science and Technology "MISiS", 4 Leninskiy prospekt, Moscow 119049, Russia

e-mail: *tikhonova@physics.msu.ru, +eshirshin@gmail.com

Abstract. Misfolded proteins produce fibrillar aggregates, which contain β-sheet higher order structures. The oligomers, protofibrils, and fibrils generated during protein aggregation process are cytotoxic and can cause various neurodegenerative diseases. Recently the photo-active materials, the photosensitizers, have attracted increased attention in the study and treatment of amyloid-related diseases. Here, we studied the photodynamic effect of the amyloid-specific fluorescence dye Thioflavin T on the formation of self-assembled peptide hydrogel. It was demonstrated that the gelation process under irradiation inhibits significantly, at that the structural and mechanical properties of mature fibrils change notably suggesting that ThT could be regarded as a theranostic probe. The developed peptide model allows for quantification of the photodynamic agent's efficiency in preventing aggregation, thus paving the way for a high-throughput test system for screening of light-responsive theranostic agents. © 2023 Journal of Biomedical Photonics & Engineering.

Keywords: hydrogel; peptide self-assembly; photosensitizer; fibrillation; scanning ion conductance microscopy; Thioflavin T; Fmoc-FF.

Paper #3572 received 16 Dec 2022; revised manuscript received 20 Dec 2022; accepted for publication 21 Dec 2022; published online 3 Feb 2023. doi: 10.18287/JBPE23.09.010304.

1 Introduction

Protein conformation disorders accompany disruptions in nervous system functioning and are involved in etiology of neurodegenerative diseases [1, 2]. Misfolding and abnormal aggregation of β-amyloid, tau, α-synuclein, and polyglutamine containing proteins may result in the plaques deposition in brain, and cytotoxicity of protein aggregates, both fibrils and oligomers on the fibrillation pathway, is considered to be among the factors initiating Alzheimer's disease, Parkinson's disease, Huntington's disease, amyotrophic lateral sclerosis [3–6].

Development of amyloid formation inhibitors has been the subject of numerous investigations, where both "chemical" and "physical" mechanisms of action were considered. While chemical approaches employ the use of specific biomolecules as amyloid inhibitors [7], physical strategies imply application of high hydrostatic pressure, low temperature, and irradiation with light [8]. In the latter case irradiation is supposed to induce

generation of reactive oxygen species (ROS, e.g., H_2O_2, O_2^-, OH, $^1O_2$) by photosensitizers such as light-responsive nanomaterials (fullerene, polyoxometalate, g-C_3N_4, etc.), organic dyes (riboflavin, rose bengal, porphyrins, etc.), metal oxide photocatalysts (Ag-TiO_2, $BiVO_4$, etc.) [9–12]. Among different photosensitizers, the methylene blue (MB) has been extensively used for photodynamic treatment of cancer cells due to its high solubility in aqueous media, low toxicity, ability to cross the blood-brain barrier, and high quantum yield of singlet molecular oxygen generation [13]. Lee et al. performed *in vivo* experiments where MB was supplied with food into the Drosophila organisms with model Alzheimer's disease, which was further illuminated by red LEDs. The high effectiveness of photodynamic treatment with MB as a sensitizer in suppressing synaptic toxicity and enhancing locomotion was demonstrated [14].

Another study demonstrated that the fluorescent dye Thioflavin T (ThT), which exhibits high affinity to amyloid fibrils [15, 16], could be used as a photosensitizer to destroy amyloid fibrils formed of the keratoepothelin peptide [17]. In the experiment, ThT molecules were incorporated into the fibrils and excited with pulsed 442 nm laser light, that led to the generation of ROS, inhibition of growth and destruction of fibrils.

ThT acts as a molecular rotor upon excitation, i.e., photon absorption results in the mutual rotation of two ThT fragments – benzthiazole ring and benzene ring, see Fig. 1 (benzthiazole ring is marked with blue color, benzene ring with yellow color) [18, 19]. Calculations demonstrate that in the ground state the angle between these two fragments, Φ, is 37°. Upon light absorption, ThT is excited to a local excited state (LE) with the same geometry, from where intramolecular ultrafast relaxation process takes place: the angle Φ increases from 37° to 90°, resulting in the formation of twisted internal charge-transfer state (TICT), which is responsible for the ultrafast (~1 ps) relaxation of excitation. Hence, triplet yield and, consequently, singlet oxygen generation rate are negligible for free ThT in aqueous solution. On the contrary, upon binding to amyloid fibrils, a significant reduction of ThT flexibility occurs, thereby preventing intramolecular rotation and TICT state formation. Hence, ThT binding to fibrils leads to a 1000-fold increase of fluorescence lifetime (up to a few ns) and makes the population of the triplet state more efficient [20, 21]. As the result, only bound ThT molecules are efficient as photosensitizers. This fact suggests that ThT could be used as a theranostic agent: it stains fibrils selectively and potentially allows for their partial destruction via photodynamic action (Fig. 1). The aim of the paper was to verify this concept based on a robust and minimalistic model system.

For this purpose, we used the fibrillar hydrogel formed as the result the of N-fluorenylmethoxycarbonyl diphenylalanine peptide (Fmoc-FF) self-assembly (Fig. 1A) [22–24]. Fmoc-FF is one of the most studied peptides for hydrogel preparation that alone or in combination with other substances can be used as a 3D scaffold for cartilage and bone tissue engineering [25].

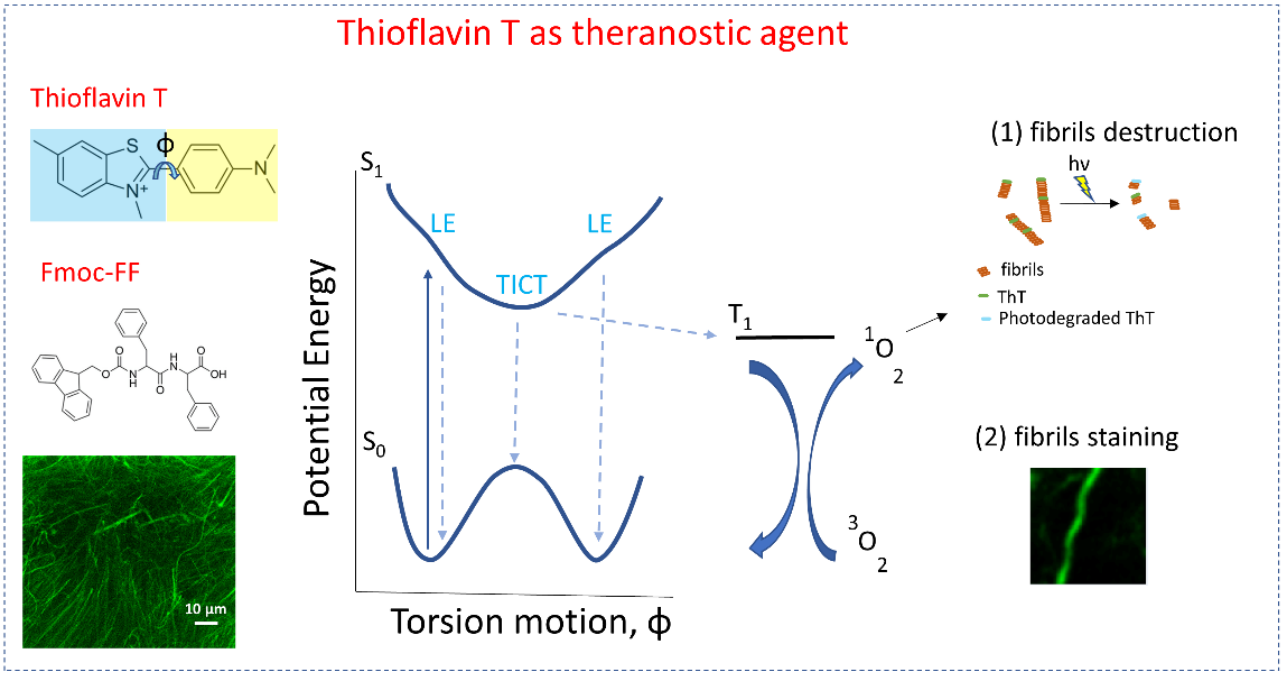


Fig. 1 The structure of ThT and Fmoc-FF (left) and schematic representation of the phophysical processes in ThT according to Ref. [18]: upon excitation into the local excited (LE) state, relative rotation of two fragments in a free ThT molecule (marked with blue and yellow rectangles in the ThT structure) occurs, leading to the emergence of the twisted internal charge transfer (TICT) state. The TICT state exhibits ultrafast relaxation to the ground state on a ~1 ps scale. Upon ThT binding to fibrils, its internal rotation is restricted, thus preventing the formation of the TICT state, leading to prolonged excited state relaxation (~1 ns) and increasing the efficiency of singlet-triplet conversion and singlet oxygen generation. Hence, ThT potentially allows for both staining and destruction of fibrils via the photosensibilisation effect.

It was shown that ThT not only could stain mature Fmoc-FF fibrils, but also could bind to the Fmoc-FF aggregates formed on the initial stages of hydrogelation [26]. The use of the peptide hydrogels as a model system for photodynamic ThT assay is attractive due to reproducibility of the kinetics of gel formation and certain similarity of interaction mechanisms upon peptide self-assembly and protein fibrils formation (π–π stacking, hydrophobic interactions). Moreover, the duration of fibrillation in the case of Fmoc-FF can be precisely tuned by external conditions and be as short as a few minutes, while for protein fibrils the aggregation process lasts from a few hours to a few weeks [27, 28]. Hence, peptide hydrogels could be a prospective system for testing physical approaches to fibrils disruption, including the photodynamic treatment.

In this paper we investigated the influence of photosensitization effect on the fibrillar structures formation by self-assembling Fmoc-FF peptide by a set of methods including fluorescence spectroscopy, fluorescence lifetime imaging microscopy (FLIM), and scanning ion-conductance microscopy (SICM). The kinetics of self-assembly and related morphological alterations were studied upon irradiation of the system in the presence of ThT. The developed model allows for quantification of the photodynamic agent's efficiency in preventing aggregation, thus paving the way for a high-throughput test system for screening of light-responsive theranostic agent.

2 Materials and Methods

2.1 Sample Preparation

The N-fluorenylmethoxycarbonyl diphenylalanine peptide (Fmoc-FF) was purchased from GL Biochem (Shanghai, China). Thioflavin T (ThT) was obtained from Sigma-Aldrich (Steinheim, Germany). The Fmoc-FF hydrogel was prepared using the solvent-switch method: peptide stock solution in dimethyl sulfoxide, $C_{\text{Fmoc-FF (stock)}}$ = 100 mg/mL, was dissolved with double distilled water to a final concentration of $C_{\text{Fmoc-FF}}$ = 1 mg/mL [29, 30]. The final pH value of the samples was set to 5.

To calculate the ThT concentration, the molar extinction coefficient of 31600 1/(M·cm) at 410 nm was used [31]. The temperature in the experiments was controlled and set to 25 °C. ThT concentration was C_{ThT} = 70 μM in all the experiments. So, the ratio of peptide to dye concentration in all the experiment was constant and equal to $C_{\text{Fmoc-FF}}/C_{\text{ThT}}$ = 26.

Photosensitization was induced by irradiating the samples at 460 nm with a LED (80 mW/cm^2).

The sample preparation for each method was as follows:

1) Turbidity measurements. The ratio of peptide to dye concentration was constant, $C_{\text{Fmoc-FF}}/C_{\text{ThT}}$ = 26 ($C_{\text{Fmoc-FF}}$ = 1865 μM, C_{ThT} = 70 μM). The irradiation time was varied (0, 5, 10, 40 min), corresponding to irradiation doses of 0, 24, 48, and 192 J/cm^2.

2) FLIM measurements. The ratio of peptide to dye concentration was constant, $C_{\text{Fmoc-FF}}/C_{\text{ThT}}$ = 26 ($C_{\text{Fmoc-FF}}$ = 1865 μM, C_{ThT} = 70 μM). Excitation was performed in the two-photon excitation regime, the excitation wavelength was set to 900 nm. The protocol was as follows: first, a ROI of 10×10 μm was irradiated for a certain time, and then a scan of a larger field, including the irradiated ROI, was performed – hence, both irradiated and non-irradiated areas were assessed.

3) Scanning ion-conductance microscopy (SICM). By this technique the structures of mature hydrogels were examined in the solution– the hydrogel that was formed without irradiation ($C_{\text{Fmoc-FF}}$ = 1865 μM) and the hydrogel that was formed after the sample was prepared and irradiated for 1 h with a 460 nm LED (80 mW/cm^2, the irradiation dose 288 J/cm^2). The samples were prepared in a Petri dish and filled with acetate buffer, pH 5.

4) Atomic force microscopy (AFM) measurements. The method of sample preparation was the same as in the SICM measurements except for the moment that the samples were dried for 2 h after the hydrogels (with or without irradiation) were formed.

5) Measurement of the rheological properties of the samples. The mechanical properties of hydrogels were examined during its formation without irradiation ($C_{\text{Fmoc-FF}}$ = 1865 μM, C_{ThT} = 70 μM) and when the hydrogel was irradiated for 40 min with a LED (460 nm, 80 mW/cm^2, the irradiation dose 192 J/cm^2).

So, turbidity, FLIM and rheological measurements were carried out during the process of hydrogel formation, whereas the microscopy studies – AFM and SICM, were carried out when the hydrogel had been already formed to analyze the final structure of investigated system.

2.2 Turbidity Measurements

Turbidity measurements were performed by measuring the transmission of a 633 nm laser through the cuvette (with a 2 mm optical path) with a spectrometer Maya 2000 PRO (Ocean Optics, USA) in a 180 degrees geometry. The exposure time was set to 100 ms for each measurement point.

2.3 Fluorescence Lifetime Imaging Microscopy (FLIM) Measurements

For FLIM measurements, a custom setup equipped with a Simple Tau 152 TCSPC FLIM module (Becker & Hickl GmbH, Berlin, Germany) was used. Fluorescence was excited by radiation from a TOPOL parametric femtosecond generator (Avesta, Moscow, Russia). Two-photon excitation was carried out at 900 nm with a pulse repetition rate of 80 MHz. The duration of one pulse was 100 fs. A lens with a 60× magnification NA = 1.4 (CFI Plan Apochromat Lambda 60×, Nikon, Japan) was used.

2.4 Measurement of the Rheological Properties of the Samples

The Physica MCR 302 rheometer (Anton Paar GmbH, Graz, Austria) was used to study the mechanical properties of hydrogel with a parallel plate geometry (25 mm in diameter). Time sweep oscillatory measurements were carried out immediately after preparation of samples. The measurements were carried out at 25 °C.

2.5 Scanning Ion-Conductance Microscopy

The SICM (ICAPPIC Limited, United Kingdom) was used to investigate the samples topography. In the experiments the inverted optical microscope Eclipse Ti-2 (Nikon, Japan) was used. The feedback control and piezo positioning was controlled by the ICAPPIC Universal Controller and Piezo Control System (ICAPPIC Limited, United Kingdom). A P-2000 laser puller (Sutter Instruments, USA) was used to fabricate the pipettes with inner radius 40–50 nm. The approach rate was 120 $\mu m \cdot s^{-1}$. The set point was 0.5% for topography studies.

In SICM, the scanning probe is a glass pipette that is filled with buffer with a radius on the order of several tens of nanometers. The main Ag/AgCl electrode is placed inside the pipette whereas the reference electrode is in the Petri dish where the sample is situated. The ion current begins to flow through the pipette tip when the potential bias is applied between Ag/AgCl electrodes. Away from the sample surface the ion current has a constant value at that it starts to decrease when the tip-sample surface distance is smaller than the probe tip radius. To obtain the topography of the sample, a feedback system is used based on the registration of the ion current flowing through the pipette and the coordinates of the piezo actuators [32].

2.6 Atomic Force Microscopy Measurements

Atomic force microscopy (AFM) photos of the dried hydrogels were obtained using a Bruker Bioscope Resolve AFM (Bruker, USA). The Peak Force Tapping mode was used to minimize the tip tapping force. We used the ScanAsyst Air cantilevers (Bruker AFM Probes, Camarillo, CA, USA) with a nominal spring constant of 0.4 N/m and a tip radius of 2 nm. 10 × 10 μm and 3 × 3 μm images were obtained at a maximal force < 2 nN, at a resolution of 256 × 256 or 512 × 512 pixels. The measurements were carried out at 25 °C for dried samples.

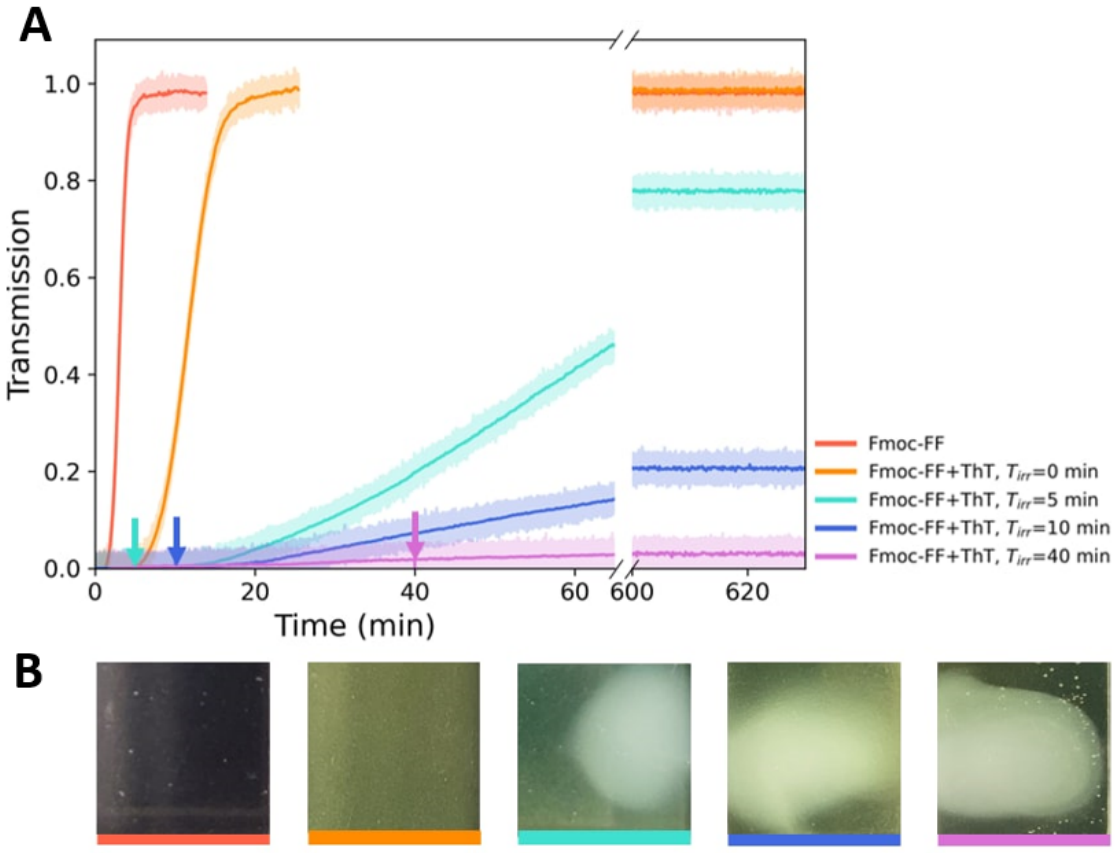


Fig. 2 (A) Irradiation time dependence of the Fmoc-FF+ThT gelation kinetics as monitored by light transmission. $C_{Fmoc\text{-}FF}$ = 1865 μM, C_{ThT} = 70 μM ($C_{Fmoc\text{-}FF}/C_{ThT}$ = 26). The irradiation power was constant, I = 80 mW/cm^2. The irradiation wavelength was λ = 460 nm. (B) The images of the Fmoc-FF systems after their transmittance curves reached a plateau and the hydrogel was formed. Red, orange, greenish-blue, blue, and violet lines correspond to Fmoc-FF in the absence of ThT and Fmoc-FF in the presence of ThT upon irradiation during 0, 2.5, 5, 10, and 40 min. The arrows indicate where irradiation was switched off for each curve.

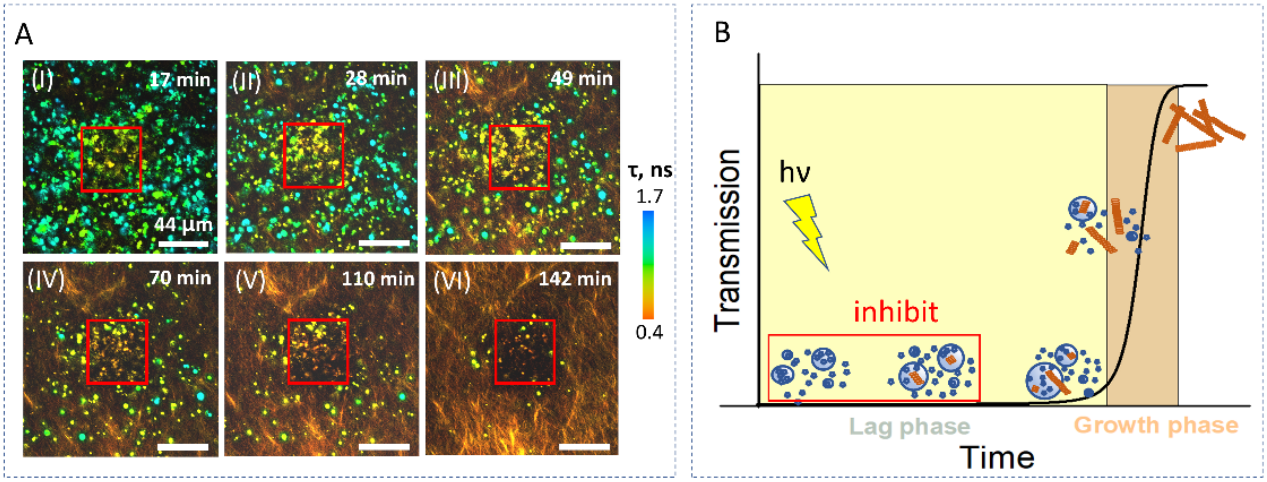


Fig. 3 (A) FLIM images of the Fmoc-FF hydrogelation process measured at different time. The red square depicts the area of irradiation. In the right upper corner of the images, the time from the beginning of the gelation can be seen. $C_{\text{Fmoc-FF}}$ = 1865 µM, C_{ThT} = 70 µM (Scale bar 44 µm). (B) Schematic of the Fmoc-FF peptide hydrogelation process tracked via transmission.

3 Results and Discussion

3.1 The Influence of Irradiation on Hydrogel Formation in the Presence of ThT

Turbidity measurements allow to observe the process of Fmoc-FF solution transition from the opaque into the optically transparent system during the hydrogel formation [27]. Hence, as the first step, the effect of the time irradiation on the Fmoc-FF self-assembly rate was assessed in the presence of ThT. Measuring the transmittance of the Fmoc-FF system under the irradiation revealed a gradual elongation of the hydrogelation kinetics, see Fig. 2A. The experiments performed at a fixed concentration of the peptide ($C_{\text{Fmoc-FF}}$ = 1865 µM) and ThT (C_{ThT} = 70 µM) while varying irradiation time (0, 5, 10, and 40 min). Importantly, no effect of irradiation on the Fmoc-FF hydrogel formation without ThT was observed, see Fig. S1.

As it can be seen from Fig. 2B, the irradiated area doesn't become transparent, moreover, the gelation kinetics slows down strongly under irradiation (see Fig. 2A). At the same time in the unirradiated area the transparency is observed. So, the irradiation of peptide in the presence of ThT leads to the inhibition of self-assembly. The image of the Fmoc-FF system at the beginning of hydrogel formation can be seen in Fig. S2.

3.2 Hydrogel Structural Phase Transition and Its Dependence on the Irradiation Time as Revealed by FLIM

To study how irradiation affects the structure of Fmoc-FF aggregates in the presence of ThT, the FLIM measurements were caried out. We note that FLIM allows both for imaging of aggregates in the system as well as for mapping the parameters of ThT microenvironment (mainly, viscosity) by mapping the ThT fluorescence lifetime [33, 34]. Fig. 3A demonstrates representative FLIM images obtained during the Fmoc-FF hydrogelation, where the red square depicts the irradiated area.

A number of stages could be observed under the Fmoc-FF hydrogel formation. When a dilution of the Fmoc-FF stock solution in water occurs, spherical aggregates can be seen (Fig. 3A(I–II)), that evolve into larger spheres after a while. Then, the transition from spheres to fibers was observed (Fig. 3A(III–IV)), at that the mature fibrillar gel was the terminal stage of the self-assembly process (Fig. 3A(V–VI)). The FLIM image for the final hydrogel with the irradiation of the central part, like Fig. 3A(VI) with smaller scale can be seen in Fig. S3, where the significant difference between irradiated and non-irradiated part of the hydrogel can be seen.

Fig. 3A(I) demonstrated that in 17 min the hydrogel had not been formed in the presence of ThT, see the non-irradiated area (out of red square). This points on the fact that ThT has a strong effect on the gelation process. This data is in accordance with work where it was revealed that ThT has a direct effect on the structural properties of the Fmoc-FF hydrogel. The kinetics of gelation changed significantly in the presence of dye: the growth rate decreases and increase of the lag phase duration were observed.

FLIM demonstrated that irradiation of the Fmoc-FF system in the presence of ThT effects the lag phase of hydrogel formation. Fig. 3A(VI) shows that while the Fmoc-FF formed fibrillar structures outside the area of irradiation, the irradiated area (red square) still contains only spherical aggregates that corresponds to the lag-phase of the Fmoc-FF peptide hydrogelation process (schematically shown in Fig. 3B).

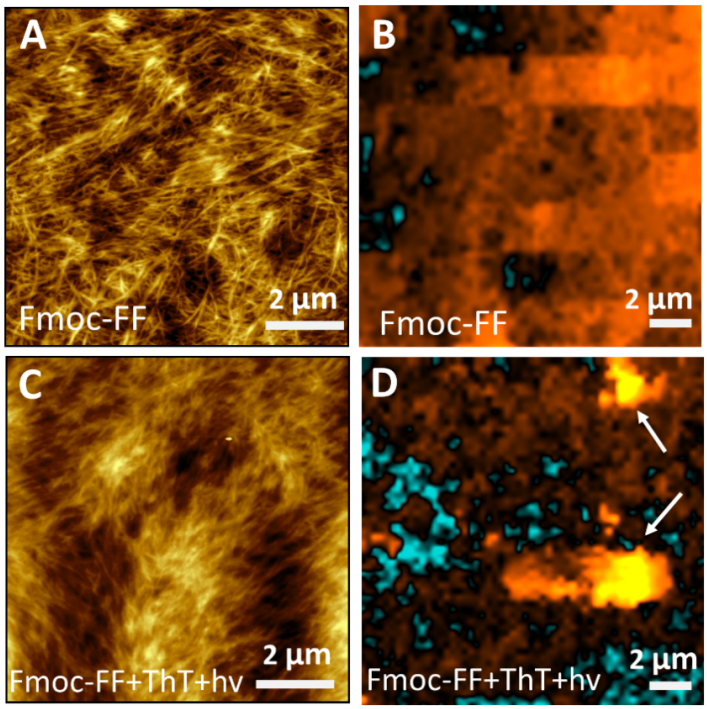


Fig. 4 Structural analysis of Fmoc-FF aggregates in the presence of ThT formed during self-assembly in the absence and presence of irradiation. AFM images for (A) Fmoc-FF hydrogel (C) Fmoc-FF aggregates formed in the presence of ThT under irradiation. SICM images for (B) Fmoc-FF hydrogel (D) Fmoc-FF hydrogel formed in the presence of ThT under the irradiation. By arrows the peptide aggregates are shown in the formed hydrogel. $C_{\text{Fmoc-FF}}$ = 1865 μM, C_{ThT} = 70 μM. The samples were irradiated for 1 h with a diode, λ_{ex} = 460 nm, I = 80 mW/cm^2.

3.3 The Effect of Photosensitizer on the Morphology and Structure of Fibers in the Fmoc-FF Hydrogel

We also assessed the morphology of the formed Fmoc-FF aggregates using two techniques – AFM and SICM. AFM measurements were performed on dried samples (Fig. 4A, C), while the SICM method allowed to obtain the topography of the surface of the sample under the native conditions (in aqueous solution) in a non-contact mode (Fig. 4B, D) [35–37].

Both methods revealed topography with high resolution – the fibrils were characterized by several hundred nanometers thickness and several micrometers length. In the case of SICM technique the mature fibrils are thicker as they "swelled" in aqueous solution in comparison with dried AFM samples, see Fig. 4A, B, correspondingly. The average thickness of fibrils that were dried overnight and obtained by AFM technique was d = 0.33 μm, while for fibrils that were studied in aqueous solution by SICM method this value was d = 0.43 μm.

According to the obtained data it can be stated that the fibers formed in the presence of photosensitizer (ThT) under the irradiation are thicker and shorter (see Fig. 4C, D) compared to the fibers formed at the absence of ThT and irradiation (see Fig. 4A, B). Also, the irradiated Fmoc-FF+ThT system demonstrated the presence of large spherical aggregated, that are marked with arrows (~ 2–3 μm, Fig. 3D), which are responsible for the turbidity of the irradiated area (Fig. 2A).

So, summarizing microscopy measurements it can be said that FLIM investigations demonstrated that the irradiation influences namely the lag phase during hydrogel formation: irradiation leads to the situation when a great amount of peptide aggregates stays in the form of spheres and do not transform into the protofibrils. SICM and AFM studies provided information dozthat when the irradiation is stopped the hydrogel is formed though its structure differs from the structure of hydrogel that is formed without irradiation: the mature irradiated hydrogel consists of shorter fibrils, also in its structure big peptide aggregates are observed.

3.4 The Effect of Photosensitizer on the Mechanical Properties of the Fmoc-FF Hydrogel

Herein the rheological measurements were carried out in order to study the effect of photosensitizer on the mechanical characteristics of self-assembled hydrogel. The dependence of the storage modulus G' on the gelation time for Fmoc-FF+ThT hydrogel without irradiation (black line) and with 40 min of irradiation (red line) (the doze of irradiation was d = 192 J/m^2) is shown in Fig. 5A. The dependence of the storage modulus on time for pure Fmoc-FF system without irradiation can be seen in Fig. S4.

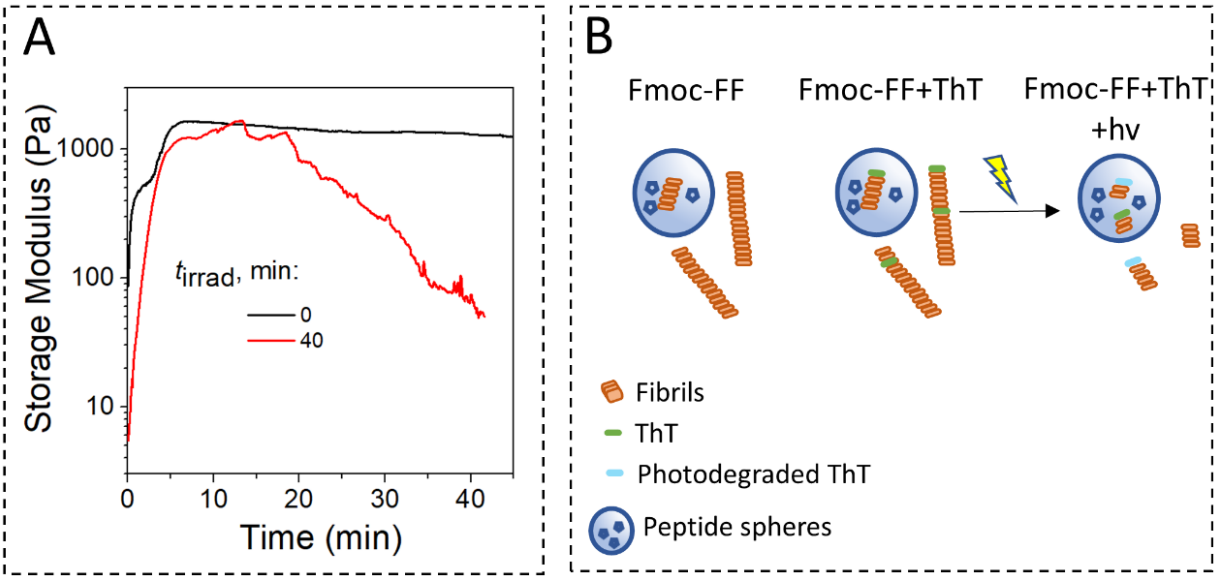


Fig. 5 (A) The dependence of storage modulus on time for Fmoc-FF + ThT hydrogel without irradiation (black line) and with 40 min of irradiation (red line), (B) An illustration of dissociation of hydrogel fibrils by photo-excited ThT.

The storage modulus G' for the investigated system reached a plateau of 1800 Pa after 5 min. The photo-excitation of photosensitizer leads to the situation when initially the storage modulus grows to the value 1800 Pa (like for Fmoc-FF+ThT system without irradiation) whereafter the softening of hydrogel structure under irradiation over time is observed (see green line in Fig. 5A). This process can be explained as follows: due to the photosensitization the oxidation of peptides occurs. This process can be a reason for the weakening of the interaction energy between peptides and further destruction of intermolecular peptides bonds that can lead to the decrease of systems' Young modulus, see Fig. 5B.

The destructive effect of ThT on different amyloid structures were demonstrated in literature. Ozawa et. al studied the irradiation of 442 nm laser with nm on β2-microglobulin (β2-m) in the presence of 10 μM ThT and showed that irradiation inhibited fibrillation and led to partial destruction of preformed fibrils [38]. Also, the effect of laser beam on Aβ (1–40) fibrils in the presence of ThT was studied [39], where irradiation also led to partial destruction of fibrils. The effect of laser irradiation on keratoepithelin in the presence of Thioflavin T was demonstrated [17]. The generation of ROS from photoexcited fluorescence dye was a reason for fibril destruction. By Ahn et al. the chemical and mechanistic study of photodynamic inhibition of Alzheimer's amyloids in the presence of ThT was conducted [40].

The chemical modifications of main amino acid residues of due to photoexcited ThT were observed using blue LED light (450 nm). The quantitative chemical kinetics analysis suggested that the oxidized monomer species did not aggregate. The authors described the oxidation of aggregates by the generation of singlet oxygen by photoexcited ThT. These results are in accordance with the data of the present work that shown that ThT can be regarded as a photosensitizer its presence has a direct effect on the structural and mechanical properties of the Fmoc-FF hydrogel.

4 Conclusions

The results of the present work show that ThT can be regarded as a photosensitizer its presence has an influence on Fmoc-FF hydrogel properties. The kinetics of hydrogel formation varied in the presence of photo-excited fluorescence dye: increase of the lag phase duration was observed. FLIM studies demonstrated that upon irradiation inhibition of hydrogel formation occurs due to the slow down of the metastable spheres transition to the protofibrils. Moreover, the irradiation of Fmoc-FF + ThT system leads to the shortening and softening of the final fibrillar structure of hydrogel suggesting that ThT can be regarded as a theranostic probe: (1) due to its presence in hydrogel the laser-induced destruction of fibrils was observed, (2) the ThT is a gold standard for amyloids staining.

Disclosures

Authors declare no competing interests.

Funding

The work was performed employing unique scientific facility "Scanning ion-conductance microscope with a confocal module" (registration number 2512530), and was financially supported by the Ministry of Education and Science of the Russian Federation, Agreement No. 075-15-2022-264.

References

1. C. Soto, S. Pritzkow, "Protein misfolding, aggregation, and conformational strains in neurodegenerative diseases," Nature Neuroscience 21(10), 1332–1340 (2018).
2. A. B. Diack, J. D. Alibhai, R. Barron, B. Bradford, P. Piccardo, and J. C. Manson, "Insights into mechanisms of chronic neurodegeneration," International Journal of Molecular Sciences 17(1), 82 (2016).
3. C. Peng, J. Q. Trojanowski, and V. M. Y. Lee, "Protein transmission in neurodegenerative disease," Nature Reviews Neurology 16(4), 199–212 (2020).
4. C. Di Scala, N. Yahi, S. Boutemeur, A. Flores, L. Rodriguez, H. Chahinian, and J. Fantini, "Common molecular mechanism of amyloid pore formation by Alzheimer's β-amyloid peptide and α-synuclein," Scientific Reports 6(1), 28781 (2016).
5. C. A. Ross, M. A. Poirier, "What is the role of protein aggregation in neurodegeneration?" Nature Reviews Molecular Cell Biology 6(11), 891–898 (2005).
6. F. J. Bäuerlein, R. Fernández-Busnadiego, and W. Baumeister, "Investigating the structure of neurotoxic protein aggregates inside cells," Trends in Cell Biology 30(12), 951–966 (2020).
7. P. Velander, L. Wu, F. Henderson, S. Zhang, D. R. Bevan, and B. Xu, "Natural product-based amyloid inhibitors," Biochemical Pharmacology 139, 40–55 (2017).
8. R. Liu, R. Su, M. Liang, R. Huang, M. Wang, W. Qi, and Z. He, "Physicochemical strategies for inhibition of amyloid fibril formation: an overview of recent advances," Current Medicinal Chemistry 19(24), 4157–4174 (2012).
9. B. I. Lee, Y. J. Chung, and C. B. Park, "Photosensitizing materials and platforms for light-triggered modulation of Alzheimer's β-amyloid self-assembly," Biomaterials 190, 121–132 (2019).
10. B. S. Dash, S. Das, and J. P. Chen, "Photosensitizer-functionalized nanocomposites for light-activated cancer theranostics," International Journal of Molecular Sciences 22(13), 6658 (2021).
11. K. Kannan, D. Radhika, K. K. Sadasivuni, K. R. Reddy, and A. V. Raghu, "Nanostructured metal oxides and its hybrids for photocatalytic and biomedical applications," Advances in Colloid and Interface Science 281, 102178 (2020).
12. J. S. Lee, B. I. Lee, and C. B. Park, "Photo-induced inhibition of Alzheimer's β-amyloid aggregation in vitro by rose bengal," Biomaterials 38, 43–49 (2015).
13. M. Oz, D. E. Lorke, M. Hasan, and G. A. Petroianu, "Cellular and molecular actions of Methylene Blue in the nervous system," Medicinal Research Reviews 31(1), 93–117 (2011).
14. B. I. Lee, Y. S. Suh, Y. J. Chung, K. Yu, and C. B. Park, "Shedding light on Alzheimer's β-amyloidosis: photosensitized methylene blue inhibits self-assembly of β-amyloid peptides and disintegrates their aggregates," Scientific Reports 7(1), 7523 (2017).
15. N. R. Rovnyagina, G. S. Budylin, Y. G. Vainer, T. N.Tikhonova, S. L. Vasin, A. A. Yakovlev, V. O. Kompanets, S. V. Chekalin, A. V. Priezzhev, and E. A. Shirshin, "Fluorescence lifetime and intensity of thioflavin T as reporters of different fibrillation stages: Insights obtained from fluorescence up-conversion and particle size distribution measurements," International Journal of Molecular Sciences 21(17), 6169 (2020).
16. B. Frieg, L. Gremer, H. Heise, D. Willbold, and H. Gohlke, "Binding modes of thioflavin T and Congo red to the fibril structure of amyloid-β (1–42)," Chemical Communications 56(55), 7589–7592 (2020).
17. D. Ozawa, Y. Kaji, H. Yagi, K. Sakurai, T. Kawakami, H. Naiki, and Y. Goto, "Destruction of amyloid fibrils of keratoepithelin peptides by laser irradiation coupled with amyloid-specific thioflavin T," Journal of Biological Chemistry 286(12), 10856–10863 (2011).
18. V. I. Stsiapura, A. A. Maskevich, V. A. Kuzmitsky, V. N. Uversky, I. M. Kuznetsova, and K. K. Turoverov, "Thioflavin T as a molecular rotor: fluorescent properties of thioflavin T in solvents with different viscosity," The Journal of Physical Chemistry B 112(49), 15893–15902 (2008).
19. F. Y. Khusbu, X. Zhou, H. Chen, C. Ma, and K. Wang, "Thioflavin T as a fluorescence probe for biosensing applications," Trends in Analytical Chemistry 109, 1–18 (2018).
20. V. I. Stsiapura, A. A. Maskevich, S. A. Tikhomirov, and O. V. Buganov, "Charge transfer process determines ultrafast excited state deactivation of thioflavin T in low-viscosity solvents," The Journal of Physical Chemistry A 114(32), 8345–8350 (2010).
21. N. Amdursky, Y. Erez, and D. Huppert, "Molecular rotors: what lies behind the high sensitivity of the thioflavin-T fluorescent marker," Accounts of Chemical Research 45(9), 1548–1557 (2012).
22. A. M. Smith, R. J. Williams, C. Tang, P. Coppo, R. F. Collins, M. L. Turner, A. Saiani, and R. V. Ulijn, "Fmoc-diphenylalanine self assembles to a hydrogel via a novel architecture based on π–π interlocked β-sheets," Advanced Materials 20(1), 37–41 (2008).
23. C. Diaferia, M. Ghosh, T. Sibillano, E. Gallo, M. Stornaiuolo, C. Giannini, G. Morelli, L. Adler-Abramovich, and A. Accardo, "Fmoc-FF and hexapeptide-based multicomponent hydrogels as scaffold materials," Soft Matter 15(3), 487–496 (2019).

24. R. Orbach, I. Mironi-Harpaz, L. Adler-Abramovich, E. Mossou, E. P. Mitchell, V. T. Forsyth, E. Gazit, and D. Seliktar, "The rheological and structural properties of Fmoc-peptide-based hydrogels: the effect of aromatic molecular architecture on self-assembly and physical characteristics," Langmuir 28(4), 2015–2022 (2012).
25. E. Rosa, C. Diaferia, E. Gianolio, T. Sibillano, E. Gallo, G. Smaldone, M. Stornaiuolo, C. Giannini, G. Morelli, and A. Accardo, "Multicomponent Hydrogel Matrices of Fmoc-FF and Cationic Peptides for Application in Tissue Engineering," Macromolecular Bioscience 22(7), 2200128 (2022).
26. T. N. Tikhonova, N. R. Rovnyagina, Z. A. Arnon, B. P. Yakimov, Y. M. Efremov, D. Cohen-Gerassi, M. Halperin-Sternfeld, N. V. Kosheleva, V. P. Drachev, A. A. Svistunov, P. S. Timashev, L. Adler-Abramovich, and E. A. Shirshin, "Mechanical Enhancement and Kinetics Regulation of Fmoc-Diphenylalanine Hydrogels by Thioflavin T," Angewandte Chemie International Edition 60(48), 25339–25345 (2021).
27. K. Lundmark, G. T. Westermark, A. Olsén, and P. Westermark, "Protein fibrils in nature can enhance amyloid protein A amyloidosis in mice: Cross-seeding as a disease mechanism," Proceedings of the National Academy of Sciences 102(17), 6098–6102 (2005).
28. C. Li, J. Adamcik, and R. Mezzenga, "Biodegradable nanocomposites of amyloid fibrils and graphene with shape-memory and enzyme-sensing properties," Nature Nanotechnology 7(7), 421–427 (2012).
29. V. Basavalingappa, T. Guterman, Y. Tang, S. Nir, J. Lei, P. Chakraborty, L. Schnaider, M. Reches, G. Wei, and E. Gazit, "Expanding the functional scope of the fmoc-diphenylalanine hydrogelator by introducing a rigidifying and chemically active urea backbone modification," Advanced Science 6(12), 1900218 (2019).
30. J. Raeburn, G. Pont, L. Chen, Y. Cesbron, R. Lévy, and D. J. Adams, "Fmoc-diphenylalanine hydrogels: understanding the variability in reported mechanical properties," Soft Matter 8(4), 1168–1174 (2012).
31. A. I. Sulatskaya, A. V. Lavysh, A. A. Maskevich, I. M. Kuznetsova, and K. K. Turoverov, "Thioflavin T fluoresces as excimer in highly concentrated aqueous solutions and as monomer being incorporated in amyloid fibrils," Scientific Reports 7(1), 2146 (2017).
32. A. Page, D. Perry, and P. R. Unwin, "Multifunctional scanning ion conductance microscopy," Proceedings of the Royal Society A: Mathematical, Physical and Engineering Sciences 473(2200), 20160889 (2017).
33. B. Yakimov, A. Gayer, E. Maksimov, E. Mamonov, A. Maydykovsky, T. Murzina, V. Fadeev, and E. Shirshin, "Fluorescence saturation imaging microscopy: molecular fingerprinting in living cells using two-photon absorption cross section as a contrast mechanism," Optics Letters 47(17), 4455–4458 (2022).
34. S. Kundu, C. Banerjee, and N. Sarkar, "Inhibiting the fibrillation of serum albumin proteins in the presence of surface active ionic liquids (SAILs) at low pH: spectroscopic and microscopic study," The Journal of Physical Chemistry B 121(32), 7550–7560 (2017).
35. V. S. Kolmogorov, A. S. Erofeev, E. Woodcock, Y. M. Efremov, A. P. Iakovlev, N. A. Savin, A. V. Alova, S. V. Lavrushkina, I. I. Kireev, A. O. Prelovskaya, E. V. Sviderskaya, D. Scaini, N. L. Klyachko, P. S. Timashev, Y. Takahashi, S. V. Salikhov, Y. N. Parkhomenko, A. G. Majouga, C. R. W. Edwards, P. Novak, Y. E. Korchev, and P. V. Gorelkin, "Mapping mechanical properties of living cells at nanoscale using intrinsic nanopipette–sample force interactions," Nanoscale 13(13), 6558–6568 (2021).
36. Y. Zhang, Y. Takahashi, S. P. Hong, F. Liu, J. Bednarska, P. S. Goff, P. Novak, A. Shevchuk, S. Gopal, I. Barozzi, L. Magnani, H. Sakai, Y. Suguru, T. Fujii, A. Erofeev, P. Gorelkin, A. Majouga, D. J. Weiss, C. Edwards, A. P. Ivanov, D. Klenerman, E. V. Sviderskaya, J. B. Edel, and Y. Korchev, "High-resolution label-free 3D mapping of extracellular pH of single living cells," Nature Communications 10(1), 5610 (2019).
37. Y. Takahashi, A. I. Shevchuk, P. Novak, Y. Murakami, H. Shiku, Y. E. Korchev, and T. Matsue, "Simultaneous noncontact topography and electrochemical imaging by SECM/SICM featuring ion current feedback regulation," Journal of the American Chemical Society 132(29), 10118–10126 (2010).
38. D. Ozawa, H. Yagi, T. Ban, A. Kameda, T. Kawakami, H. Naiki, and Y. Goto, "Destruction of amyloid fibrils of a β2-microglobulin fragment by laser beam irradiation," Journal of Biological Chemistry 284(2), 1009–1017 (2009).
39. H. Yagi, D. Ozawa, K. Sakurai, T. Kawakami, H, Kuyama, O. Nishimura, T. Shimanouchi, R. Kuboi, H. Nauki, and Y. Goto, "Laser-induced propagation and destruction of amyloid β fibrils," Journal of Biological Chemistry 285(25), 19660–19667 (2010).
40. M. Ahn, B. I. Lee, S. Chia, J. Habchi, J. R. Kumita, M. Vendruscolo, C. Dobson, and C. B. Park, "Chemical and mechanistic analysis of photodynamic inhibition of Alzheimer's β-amyloid aggregation," Chemical Communications 55(8), 1152–1155 (2019).

Features of L-Menthol Crystallization in Optically Active Medium Based on L- and D-Asparaginate Chitosan

Anna B. Shipovskaya*, Natalia O. Gegel, and Xenia M. Shipenok
Department of Polymers, Saratov National Research State University named after N.G. Chernyshevsky, 83 Astrakhanskaya str., Saratov 410012, Russia

***e-mail:** shipovskayaab@yandex.ru

Abstract. The phase separation kinetics of an ethanolic L-menthol solution in an aqueous solution of optically and biologically active chitosan L- and D-aspartate was studied. It has been established that this process proceeds according to the extraction crystallization mechanism and combines two types of phase separation, namely: liquid–liquid and liquid–crystal. The effect of aspartic acid stereoisomer, chitosan molecular weight, and polymer: acid ratio on the optical, structural-morphological, and dimensional characteristics of dispersed phase droplets at the initial stage of phase separation and crystal aggregates of the L-menthol condensed phase at the final stage was assessed. In the chitosan D-aspartate medium, as well as with an increase in the concentration of components in the optically active medium and the molecular weight of the polymer, the rate of phase separation, the size of droplets and particles increase. It has been suggested that the system under study is promising for encapsulating hydrophobic drugs, creating chirooptic waveguides, and sensors for biomedical purposes, as well as developing new methods for studying the fundamental principles of phase separation in intracellular regulation of membraneless organelles and subcellular organization of biosystems, including under stress conditions of a living organism underlying the development of new pharmaceuticals to treat rare and currently incurable diseases. © 2023 Journal of Biomedical Photonics & Engineering.

Keywords: chitosan; L- and D-aspartic acid; salt formation; L-menthol; phase separation; extraction crystallization; spherulites; intracellular regulation; subcellular organization.

Paper #3582 received 15 Jan 2023; revised manuscript received 2 Feb 2023; accepted for publication 9 Feb 2023; published online 27 Feb 2023. doi: 10.18287/JBPE23.09.010305.

1 Introduction

Achieving control over the molecular and structural chirality of the created product is one of the urgent problems of modern materials science in the field of stereospecific polymeric materials for biomedical purposes. This is primarily due to some functional features of such systems, which provide fundamentally novel chirooptic and complementary-selective properties inaccessible for achiral polymeric materials [1–4]. For example, salt complexes of the aminopolysaccharide chitosan (CS) with L- and D-ascorbic acid (AscA) or L- and D-aspartic acid (AspA) significantly differ in chirooptic, structural-morphological, and biological properties from traditional chitosan-containing materials obtained from polymer solutions in optically inactive carboxylic acids, depending on the stereoisomer (L- or D-) of the acid used [5–7]. At the same time, CS salts with the biologically inactive D-isomers of AscA and AspA have the best properties, while the L-isomer of AscA (vitamin C) or AspA (an essential amino acid) exhibits the highest biological activity in the case of individual acids.

The specific biological role of D-isomers of the acids is no longer considered as a rare occurrence, since recent studies have revealed a deviation from the previously

declared “chiral purity” of biosystems, in particular, the principle of constructing natural proteins from L-amino acids only. It has turned out that, in addition to the detection of D-amino acids in the cell walls of prokaryotes, free D-amino acids are involved in normal metabolism and in the regulation of eukaryotic vital activity [8]. D-AspA has been found in mammalian hormone-producing cells [9] and human dental dentin [10]. It has also been established that it is not the natural biologically active L-isomer which is effective in the treatment of certain diseases, but its synthetic D-antipode [11, 12]. In addition, D-amino acids have been shown to be highly effective in destroying biofilms and reducing the antibiotic resistance of living organisms, which has opened up new directions for the development of personalized antimicrobial drugs [13, 14].

One of the informative approaches to assessing the stereospecificity of the spatial organization of L- and D-isomer chitosan salts can be considered the study of their interaction with some chiral, optically pure and, at the same time, biologically active compound, e.g., L-menthol. This organic substance belongs to the class of cyclic monoterpene alcohols, it is solid at room temperature and melts within 42–45 °C (α-phase), is insoluble in water and readily soluble in ethyl alcohol, chloroform and acetone, has optical activity (in solution) and optical anisotropy (in melts). Depending on the conditions of phase separation (temperature gradient, cooling rate, substrate structure, solvent, and precipitating medium), it is characterized by a variety of morphostructures formed in this process. For example, ring-shaped spherulites are formed during thermally induced crystallization from a melt in an air atmosphere, in which acicular crystals (whiskers) of L-menthol self-organize into radially oriented periodic regions with high and low densities of the solid phase of the substance, or non-banded continuous spherulites, consisting of densely packed lamellar crystals [15]. Such rhythmic crystallization could be due to the chirality of L-menthol [16], as well as nonlinear diffusion of the substance during mass transfer [17, 18] and the “unbalanced” surface energy of the system [19]. During thermally induced crystallization in an aqueous medium (antisolvent), the phase transition from the liquid–liquid region to the solid–liquid one is accompanied by the formation of the stable α-polymorphic form of L-menthol [20, 21]. When dispersing an L-menthol solution in ethanol or chloroform into an aqueous medium, a phase separation of the liquid–liquid type is observed with the formation of an oil-in-water emulsion, whose dispersed phase is represented by nano- and microscopic drops of the hydrophobic component [22−24]. The liquid–liquid type of phase separation was successfully used for the encapsulation of L-menthol into nano- and microcapsules made of chitosan (solutions in CH_3COOH and additional cross-linking of the polymer with Na tripolyphosphate) [25], the vegetable protein zein [23], or polycaprolactone [24] were used, and specific thermally induced crystallization with no use of any organic solvent was successfully used for the encapsulation of L-menthol into monodisperse spherical micro- and macroparticles [20], thus ensuring stabilization, controlled delivery and release of this substance. The use of L-menthol as an initiator of multiepitaxial oriented crystallization (liquid-phase epitaxy) made it possible to obtain ordered and aligned poly-lactic-*co*-glycolic acid nanofibers for tissue engineering scaffolds and neural interface systems [22].

L-menthol has low toxicity for humans [26, 27]. In addition to well-known cooling properties and a characteristic minty odor, L-menthol exhibits anesthetic, antibacterial, antitumor and immunomodulatory effects, and is also an effective agent for transdermal drug transport [22, 28]. It has also demonstrated the ability to act as an inhibitory molecule on voltage-gated channels which significantly affect the neurotransmission functions of a living organism and gene expression in various cell types [29]. Based on the above properties and taking into account the molecular chirality and variety of supramolecular chiral symmetries formed under varying crystallization conditions, L-menthol can be considered as a model biosystem for studying the stereospecificity of the chiral polymeric materials developed. In particular, we considered L-menthol to be suitable for studying the decay kinetics of optical anisotropy intensity during phase separation of this substance in a chiral aqueous medium based on the optically and biologically active chitosan L- and D-aspartate. This process mimics liquid-phase separation during intracellular signal transduction [30, 31].

We have previously found that the interaction of an aqueous solution of chitosan ascorbate and an L-menthol solution in ethyl alcohol or its mixture with acetone is accompanied by crystalline phase separation of the mixture system to form anisodiametric fibrillar entities in the case of CS in L-AscA, which exhibit pronounced optical anisotropy in polarized light, or densely packed confocal domains of a shape close to spherical in the case of CS in D-AscA [5, 6]. In this work, we will consider features of the crystallization of the L-menthol + ethanol system in an aqueous solution of CS in L- and D-AspA.

2 Materials and Methods

The following reagents were used: chitosan hydrochloride with a viscosity average molecular weight $\overline{M}_\eta$ = 38 kDa (CS-38), a degree of deacetylation DD = 80 mol %, and chitosan with $\overline{M}_\eta$ = 200 kDa (CS-200), DD = 82 mol % (Bioprogress Ltd., RF); L-AspA (JSC Bioamid, RF); D-AspA (Vekton Ltd., RF); L-menthol with a 99% basic substance (Alfa Aesar, Heysham, Lancs, UK); 95% ethyl alcohol (RFK Corp., Orel, RF); and distilled water. All reagents were chemical grade and used without further purification.

To prepare solutions of chitosan L- and D-asparaginate, weighed portions of CS, L- and D-AspA powders were dissolved in distilled water under stirring on a magnetic stirrer at 50 °C for 3 h. The concentration

of CS was varied in the range of 0.3–0.8 g/dL, those of L- and D-AspA were varied within 0.2–0.6 g/dL. Since the protonation degree of -NH_2 groups of CS upon its dissolution in an aqueous AspA solution does not exceed 0.8–0.9 [32], the molar ratio [AspA]/[~-NH_2] = 0.85−0.95 mol/monomol was observed in the preparation of solutions to eliminate the influence of unbound acid. A solution of L-menthol with a concentration of 2.5 g/dL was prepared by dissolving a sample of air-dry L-menthol in 95% ethyl alcohol for 24 h.

Surface tension was measured on a K20 automatic tensiometer (KRÜSS GmbH, Germany) using the Wilhelmy plate method at 25 °C.

To explore the kinetics of phase separation, 3 ml of an aqueous solution of CS in L-(D-)AspA was poured into a Petri dish 3 cm in diameter, and 1.5 ml of an ethanolic L-menthol solution was added dropwise onto the surface of the liquid medium with an automatic dispenser without stirring the system. The Petri dish was covered with a cover slip and left under static conditions in an air atmosphere at a temperature of 22 ± 2 ºC for 24 h. The phase separation process was considered complete if there were no changes in both the size and morphostructure of the condensed phase and the disappearance of any birefringence effect.

The kinetics of phase separation was observed both visually and on a LaboPol-2 (RF) polarization microscope (PM) with the polarizer and analyzer crossed. A halogen lamp (12 V, 30 W) served as the light source. PM-photos were obtained by a DMC 300 (3 Mpx) USB camera (Hangzhou, China). The size of the forming phases (droplets and solid-phase particles) was measured using the scale of an eyepiece micrometer with a division value of 0.01 mm. The effective diameter was taken as the size of droplets and particles with shapes close to spherical, while the largest characteristic effective diameter (largest transverse size) was taken as the size of particles with a noticeably different from spherical shape.

The morphology of the air-dry condensed phase of L-menthol isolated at the final stage of phase separation was evaluated by scanning electron microscopy (SEM) on a MIRA\\LMU scanning electron microscope (Czech Republic) at a voltage of 15 kV and a conductive current of 400 pA. The sample preparation was carried out as follows: the liquid phase was removed from the Petri dish with a plastic pipette, the remaining condensed phase was dried in air at 22 ± 2ºC for 24 h until the formation of an air-dry state of the substance, then the resulting object was fixed on a standard aluminum table of an electronic microscope with plastic tweezers and deposited a gold layer 5 nm thick using a K450X Carbon Coater (Germany).

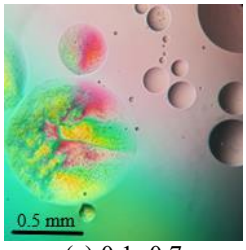
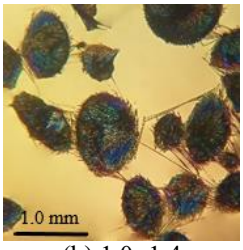
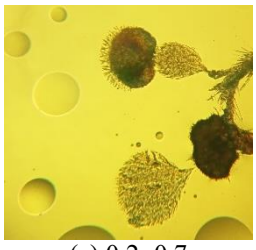
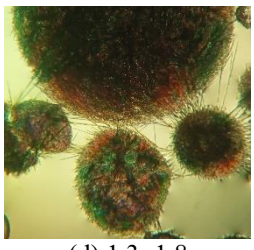
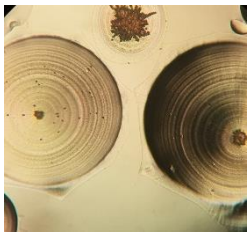
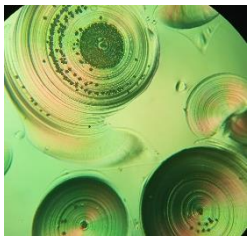
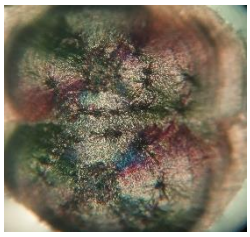
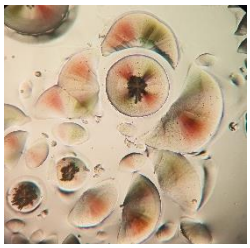
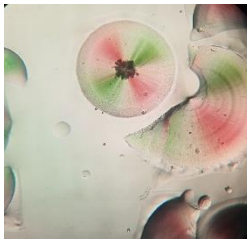
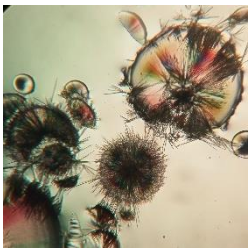
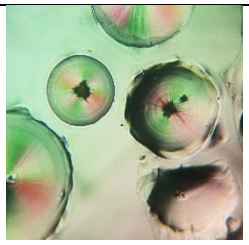
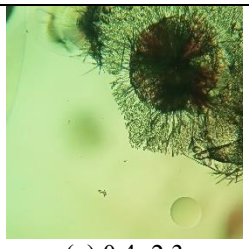
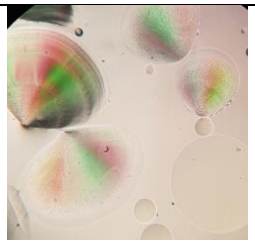
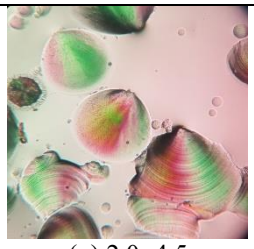
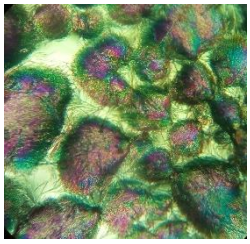
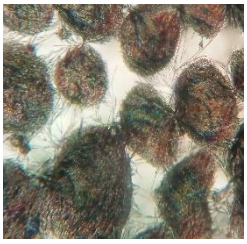
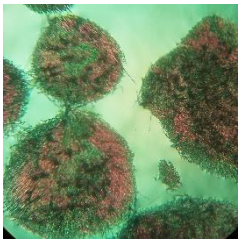
3 Results and Discussion

Studying L-menthol crystallization in an optically active aqueous medium, we discovered a new feature of the phase separation of this substance (not having noted by other authors), which consists in a combination of two types of phase separation, namely: liquid–liquid and liquid–crystal. After applying the ethanolic L-menthol solution to the surface of the aqueous solution of CS L- and D-aspartate, the spontaneous dispersion of the hydrophobic weakly polar component in the aqueous medium begins almost immediately to form a direct oil-in-water microemulsion. The liquid–liquid phase separation proceeds very intensively and visually resembles the process of water seething, just without a characteristic sound background. Subsequently, the process of coalescence of microdroplets proceeds, and crystallization of the optically active low-molecular-weight substance proceeds in the macrodroplets of the dispersed phase. Table 1 gives PM-photos and the size of droplets and particles formed during the phase separation of L-menthol in the solutions of CS-38(-200) in L- and D-AspA.

Consider the kinetics of the phase formation process of the L-menthol + ethanol system in an aqueous solution of chitosan L- and D-aspartate. At the initial stage of phase separation (2–5 min after the start of the experiment), drops of the alcoholic menthol solution, which have microscopic dimensions and are initially isotropic, increase up to millimeter sizes due to Brownian aggregation of particles and acquire birefringence. When observed in a polarizing optical microscope through a system of crossed polarizers, it is clearly seen that phase-separated optically anisotropic macrodroplets of the oil phase are characterized by a ring ordering of the substance with a radial orientation of multi-colored texture patterns (anisotropic periodic spherulites), Maltese-cross textures are also observed, which indicates the beginning of L-menthol crystallization. With an increase in the concentration of CS : AspA components in the antisolvent liquid phase, the phase formation rate increases, and the droplet size decreases, which may be due to the superposition of the effects of increased viscosity of the polymer solution with a simultaneous decrease in the protonation degree of its -NH_2 groups [32].

At the next stage of the phase separation of the system (5–30 min), the macrodroplets of the dispersed phase (hydrophobic in nature) are separated from the dispersion medium (not only by PM, but also visually) and L-menthol crystallization continues therein to form spherical or ovoid solids particles of non-banded spherulite morphology, consisting of densely packed whiskers. In some cases, coalescence of such particles and individual whiskers into larger supramolecular formations is observed (see photo (r), (t), and (v) in Table 1) and even their coalescence into a continuous optically anisotropic crystalline phase (photo (x) in Table 1). In this case, birefringence attenuation is observed, and the effect of optical anisotropy disappears after 24 h, which is expressed in the disappearance of the color effect of the glow of objects. The molecular weight of CS has little effect on the morphostructure of liquid-like oily droplets and aggregates of L-menthol whiskers, but its increase raises the phase separation rate, the density and thickness of the condensed phase.

Table 1 PM photos of the extraction crystallization stages of an ethanolic L-menthol solution in aqueous CS solutions in L- and D-AspA with varying concentrations of CS : AspA, magnification ×40. The range of effective diameter (min−max) of droplets and particles formed is indicated under the photos.

Concentration CS : AspA (g/dL : g/dL)	PM-photos and droplet/particle size (mm)			
	CS · L-AspA		CS · D-AspA	
	Extraction crystallization time (min)			
	5	30	5	30
	CS-38			
0.3 : 0.2	 (a) 0.1−0.7	 (b) 1.0−1.4	 (c) 0.2−0.7	 (d) 1.3−1.8
0.6 : 0.4	 (e) 0.3−1.4	 (f) 1.2−1.4	 (g) 0.4−1.7	 (h) 1.5−2.5
0.8 : 0.6	 (i) 0.1−0.4	 (j) 0.2−0.8	 (k) 0.3−0.8	 (l) 0.5−1.3
	CS-200			
0.3 : 0.2	 (m) 0.3−0.8	 (n) 0.4−2.3	 (o) 0.5−1.0	 (p) 2.0−4.5
0.6 : 0.4	 (q) 0.4−1.0	 (r) 0.5−3.0	 (s) 2.0−4.5	 (t) 3.0−7.0

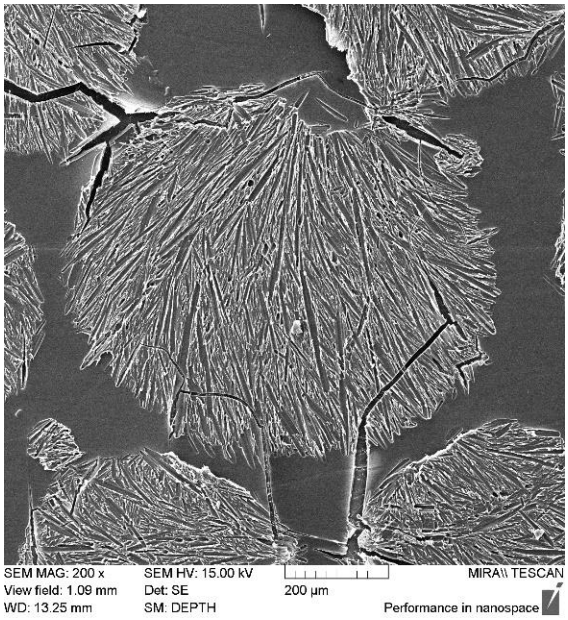


(u) 0.05−0.1 (v) 0.2−1.0 (w) 1.7−2.0 (x) 7.0−10.0

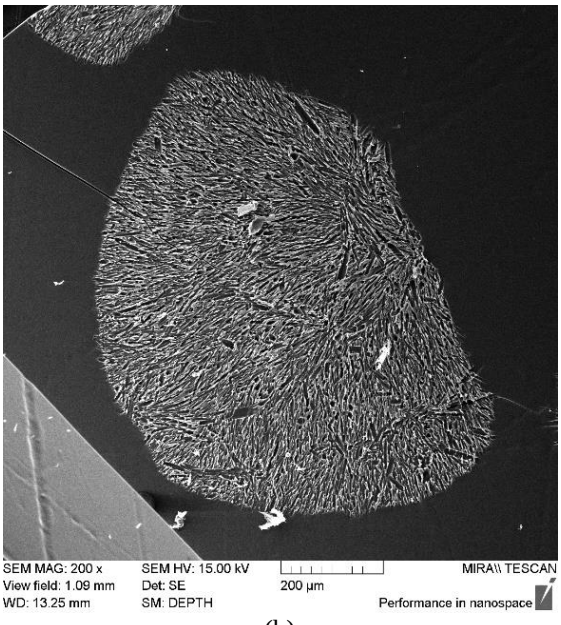
According to the phase diagram [23], intensive dispersion of the ethanolic L-menthol solution in the achiral aqueous medium results in liquid phase separation to form an emulsion. Suspended emulsion drops are unstable; they spontaneously coalesce over time due to the system tending to a minimum of its free energy by decreasing the phase interface, which leads to the separation of the system into two liquid macrophases. In the case of dispersion of the ethanolic L-menthol solution in the chiral aqueous medium based on CS in L- and D-AscA, solid-phase separation was fixed with the precipitation of mixed polymorphic crystalline CS-menthol modifications [5, 6]. Based on the above, the phase separation of L-menthol in the chiral aqueous medium based on CS in L- and D-AspA, combining spontaneous liquid-phase (in the absence of convection and mixing) and solid-phase (in the absence of a temperature gradient) phase separation, is essentially selective extraction crystallization of the chiral low-molecular-weight substance: it was observed for the first time for the objects studied. This process is probably due to a significant difference in the surface energy of the achiral and chiral aqueous media. For example, the surface tension of H_2O at 25 ºC is 71.9 mN/m, while that of CS solutions in L- and D-AspA at CS : AspA = 0.8 : 0.6 g/dL : g/dL are 47.1 and 43.4 mN/m, respectively.

It should also be noted the influence of the AspA isomer on the formation rate of L-menthol micro- and macroemulsions, as well as the size characteristics of the droplets and particles formed. In the aqueous CS · D-AspA-based medium, the rate of liquid–liquid and liquid–solid phase separation is significantly higher than in that on the basis of CS · L-AspA. The size of the oily phase droplets and anisotropic crystalline particles is also significantly higher during phase formation in the CS · D-AspA medium. In the CS ·L-AspA solution, the crystallites of the dispersed phase almost do not aggregate, forming only dendritic entities of non-banded spherulites and primary structural elements (filamentous whiskers), while in the CS · D-AspA medium (especially at high concentrations of CS : AspA), the whiskers coalesce into a compacted condensed phase, which is confirmed by SEM.

As an example, Fig. 1 shows SEM photos of the air-dry condensed phase isolated during the extraction crystallization of L-menthol in the aqueous solution of CS-200 in L- and D-AspA at the component concentration of 0.6 : 0.4 g/dL : g/dL.



(a)



(b)

Fig. 1 SEM photos of the condensed phase isolated during the extraction crystallization of the ethanolic L-menthol solution in the aqueous CS-200 solution in L-AspA (a) and in D-AspA (b) at the concentration of components CS-200 : L-(D-)AspA = 0.6 : 0.4 g/dL : g/dL; the scale mark, 200 µm.

For ease of comparison, non-banded spherulites of similar size were selected. Darker and lighter whiskers correspond to high-density and low-density crystalline packing, respectively, while extended dark bands, matching the background color of the SEM photo, correspond to an empty area (no crystals). As can be seen, the crystallites are represented by the so-called leaky radial configuration, when whiskers grow from one point into a cone-shaped space and the angle between the main axes of the growing whiskers is approximately 20−30º. At the same time, the condensed L-menthol phase obtained in the CS-200 · L-AspA medium is more loose than that obtained in the CS-200 · D-AspA medium.

We should also dwell on the difference in orientational ordering and supramolecular chirality of non-banded crystal structures obtained in this work in an optically active aqueous medium and in an achiral aqueous medium in Ref. [15]. Non-banded L-menthol spherulites during thermally induced phase separation (in the absence of a liquid medium) are formed due to the spatial growth of lamellar crystals or of whiskers during extraction crystallization in a chiral aqueous medium. Lamellar spherulites have a twist-radial orientation, i.e. spherical symmetry about the center, since the crystals grow radially from a common center in the disk space and twist along the radius of the spherulite. Acicular spherulites of leaked radial orientation have no center of symmetry due to the radial growth of crystals from a common point in a conical space. Thus, acicular spherulites, in addition to molecular chirality, exhibit macroscopic chirality as well.

4 Conclusion

We have studied the decay kinetics of the intensity of the optical anisotropy of the L-menthol + ethanol system at a qualitative level during its phase separation in an aqueous solution of L- and D-chitosan aspartate. We emphasize once again that this process proceeds spontaneously according to the extraction crystallization mechanism and combines two types of phase separation, namely: liquid–liquid and liquid–crystal. The effect of AspA stereoisomer, variation of the CS : L-(D-)AspA ratio, and polymer molecular weight on the optical anisotropy, morphostructure, and droplet size of the dispersed phase at the initial stage of phase separation and phase aggregates of the L-menthol crystalline phase at the final stage was assessed. It has been established that in the CS · D-AspA medium, in contrast to CS · L-AspA, larger particles of oily droplets and aggregated L-menthol crystals are formed, which coalesce in time into a continuous optically anisotropic condensed phase. With an increase in the CS : L-(D-)AspA concentration and the molecular weight of the polymer, the rate of phase separation increases.

The results obtained open up extremely interesting practical applications. It is expected that aqueous CS solutions in L- or D-AspA can be used to encapsulate not only L-menthol, but also other hydrophobic drugs into microcapsules and microparticles, as well as to design new types of chirooptic waveguides and biomedical sensors. In addition, since biochemical reactions inside cells proceed in the limited spaces of both classical membrane and non-membrane organelles (cell bodies in the form of a liquid drop formed as a result of the liquid–liquid phase separation [30, 31]), the hydroalcoholic CS · L-(D-)AspA + L-menthol system could be very useful for studying the fundamental principles of intracellular communication and regulation in both physiological and pathological cellular processes.

Disclosures

All authors declare that there is no conflict of interests in this paper.

Acknowledgements

The study was supported by a grant from the Russian Science Foundation № 22-23-00320, https://rscf.ru/project/22-23-00320/.

References

1. M. Mabrouk, S. F. Hammad, A. A. Abdella, and F. R. Mansour, “Enantioselective chitosan-based racemic ketoprofen imprinted polymer: chiral recognition and resolution studym,” International Journal of Biological Macromolecules 200, 327–334 (2022).
2. C. Liu, C. Dong, S. Liu, Y. Yang, and Z. Zhang, “Multiple chiroptical switches and logic circuit based on salicyl-imine-chitosan hydrogel,” Carbohydrate Polymers 257, 117534 (2021).
3. X. Dou, N. Mehwish, C. Zhao, J. Liu, C. Xing, and C. Feng, “Supramolecular hydrogels with tunable chirality for promising biomedical applications,” Accounts of Chemical Research 53(4), 852–862 (2020).
4. L. Xu, Y. A. Huang, Q. J. Zhu, and C. Ye, “Chitosan in molecularly-imprinted polymers: Current and future prospects,” International Journal of Molecular Sciences 16(8), 18328–18347 (2015).
5. A. B. Shipovskaya, O. N. Malinkina, N. O. Gegel, I. V. Zudina, and T. N. Lugovitskaya, “Structure and properties of chitosan salt complexes with ascorbic acid diastereomers,” Russian Chemical Bulletin 70(9), 1765–1774 (2021).
6. N. O. Gegel, Yu. Yu. Zhuravleva, A. B. Shipovskaya, O. N. Malinkina, and I. V. Zudina, “Influence of chitosan ascorbate chirality on the gelation kinetics and properties of silicon-chitosan-containing glycerohydrogels,” Polymers 10(3), 259–275 (2018).

7. A. B. Shipovskaya, N. O. Gegel, X. M. Shipenok, O. S. Ushakova, T. N. Lugovitskaya, and I. V. Zudina, "Structure, properties and biological activity of chitosan salts with L- and D-aspartic acid," Biology and Life Sciences Forum 20(1), 5 (2022).
8. V. A. Tverdislov, L. V. Yakovenko, and A. A. Zhavoronkov, "Chirality as a problem of biochemical physics," Russian Chemical Journal LI(1), 13–22 (2007) [in Russian].
9. A. D'Aniello, "D-aspartic acid: an endogenous amino acid with an important neuroendocrine role," Brain Research Reviews 53(2), 215234 (2007).
10. S. C. Zapico, D. H. Ubelaker, and J. Adserias-Garriga, "Applications of physiological bases of aging to forensic science," Chapter 13 in Forensic Science and Humanitarian Action: Interacting with the Dead and the Living, R. C. Parra, S. C. Zapico, and D. H. Ubelaker (Eds.), John Wiley & Sons Ltd., New York, 183-197 (2020).
11. J. Patočka, Z. Navrátilová, "D-serin: Od kuriózní molekuly k potenciálnímu psychofarmaku [D-serine: from curiosity molecule to potential psychopharmaceutical]," Psychiatry 23(3), 142–147 (2019).
12. A. González-Sarrías, M. Á. Núñez-Sánchez, R. García-Villalba, F. A. Tomás-Barberán, and J. C. Espín, "Antiproliferative activity of the ellagic acid-derived gut microbiota isourolithin A and comparison with its urolithin A isomer: the role of cell metabolism," European Journal of Nutrition 56(2), 831–841 (2017).
13. E. Adaligil, K. Patil, M. Rodenstein, and K. Kumar, "Discovery of peptide antibiotics composed of D-amino acids," ACS Chemical Biology 14(7), 1498–1506 (2019).
14. R. Kumar, N. Singh, A. Chauhan, M. Kumar, R. S. Bhatta, and S. K. Singh, "Mycobacterium tuberculosis survival and biofilm formation studies: effect of D-amino acids, D-cycloserine and its components," Journal of Antibiotics 75, 472–479 (2022).
15. T. Kovács, R. Szűcs, G. Holló, Z. Zuba, J. Molnár, H. K. Christenson, and I. Lagzi, "Self-assembly of chiral menthol molecules from a liquid film into ring-banded spherulites," Crystal Growth & Design 19(7), 4063–4069 (2019).
16. A. G. Shtukenberg, Y. O. Punin, A. Gujral, and B. Kahr, "Growth actuated bending and twisting of single crystals," Angewandte Chemie International Edition 53(3), 672−699 (2014).
17. H.-F. Wang, C.-H. Chiang, W.-C. Hsu, T. Wen, W.-T. Chuang, B. Lotz, M.-C. Li, and R.-M. Ho, "Handedness of twisted lamella in banded spherulite of chiral polylactides and their blends," Macromolecules 50, 5466−5475 (2017).
18. T. Kyu, H. W. Chiu, A. J. Guenthner, Y. Okabe, H. Saito, and T. Inoue, "Rhythmic growth of target and spiral spherulites of crystalline polymer blends," Physical Review Letters 83(14), 2749−2752 (1999).
19. J. Xu, H. S. Ye, Zhang, and B. Guo, "Organization of twisting lamellar crystals in birefringent banded polymer spherulites: a mini-review," Crystals 7(8), 241–251 (2017).
20. M. Sun, S. Du, W. Tang, L. Jia, and J. Gong, "Design of spherical crystallization for drugs based on thermal-induced liquid-liquid phase separation: case studies of water-insoluble drugs," Industrial & Engineering Chemistry Research 58(44), 20401–20411 (2019).
21. I. De Albuquerque, M. Mazzotti, "Influence of liquid-liquid phase separation on the crystallization of L -Menthol from water," Chemical Engineering & Technology 40(7), 1339–1346 (2017).
22. E. Betz-Güttner, M. Righi, S. Micera, and A. Fraleoni-Morgera, "Directional growth of cm-long PLGA nanofibers by a simple and fast wet-processing method," Materials 15(2), 687 (2022).
23. S. Kim, S. C. Peterson, "Optimal conditions for the encapsulation of menthol into zein nanoparticles," LWT 144, 111213 (2021).
24. A. Ferri, N. Kumari, R. Peila, and A. A. Barresi, "Production of menthol-loaded nanoparticles by solvent displacement," Canadian Journal of Chemical Engineering 95(9), 1690–1706 (2017).
25. R. Nuisin, J. Krongsin, S. Noppakundilograt, and S. Kiatkamjornwong, "Microencapsulation of menthol by crosslinked chitosan via porous glass membrane emulsification technique and their controlled release properties," Journal of Microencapsulation 30(5), 498–509 (2013).
26. A. M. Api, D. Belsito, D. Botelho, D. Browne, M. Bruze, G.A. Burton Jr., J. Buschmann, M.L. Dagli, M. Date, W. Dekant, C. Deodhar, M. Francis, A.D. Fryer, K. Joshi, S. La Cava, A. Lapczynski, D.C. Liebler, D. O'Brien, R. Parakhia, A. Patel, T. M. Penning, G. Ritacco, J. Romine, D. Salvito, T. W. Schultz, I. G. Sipes, Y. Thakkar, E. H. Theophilus, A. K. Tiethof, Y. Tokura, S. Tsang, and J. Wahler, "RIFM fragrance ingredient safety assessment, menthyl isovalerate CAS registry number 16409-46-4," Food and Chemical Toxicology 110, S486–S495 (2017).
27. H. K. Vaddi, P. C. Ho, Y. W. Chan, and S. Y. Chan, "Terpenes in ethanol: haloperidol permeation and partition through human skin and stratum corneum changes," Journal of Controlled Release 81(1–2), 121–133 (2002).
28. G. P. P. Kamatou, I. Vermaak, A. M. Viljoen, and B. M. Lawrence, "Menthol: a simple monoterpene with remarkable biological properties," Phytochemistry 96, 15–25 (2013).
29. M. Oz, E. G. El Nebrisi, K. H. S. Yang, F. C. Howarth, and L. T. Al Kury, "Cellular and molecular targets of menthol actions," Frontiers in Pharmacology 8, 472 (2017).
30. S. V. Nesterov, N. S. Ilyinsky, and V. N. Uversky, "Liquid-liquid phase separation as a common organizing principle of intracellular space and biomembranes providing dynamic adaptive responses," Biochimica et Biophysica Acta – Molecular Cell Research 1868(11), 119102 (2021).
31. D. M. Mitrea, R. W. Kriwacki, "Phase separation in biology; functional organization of a higher order," Cell Communication and Signaling 14, 1 (2016).

32. T. N. Lugovitskaya, A. B. Shipovskaya, S. L. Shmakov, and X. M. Shipenok, "Formation, structure, properties of chitosan aspartate and metastable state of its solutions for obtaining nanoparticles," Carbohydrate Polymers 277, 118773 (2022).

Multicentral Agent-Based Model of Four Waves of COVID-19 Spreading in Nizhny Novgorod Region of Russian Federation

Mikhail Kirillin[1], Aleksandr Khilov[1*], Valeriya Perekatova[1], Ekaterina Sergeeva[1], Daria Kurakina[1], Ilya Fiks[1], Nikolay Saperkin[1,2], Ming Tang[3], Yong Zou[3], Elbert Macau[4], and Efim Pelinovsky[1,5]

[1] Institute of Applied Physics RAS, 46 Ul'yanov str., Nizhny Novgorod 603950, Russia

[2] Privolzhsky Research Medical University, 10/1 Minin and Pozharsky sq., Nizhny Novgorod 603950, Russia

[3] School of Physics and Electronic Science, 3663 N. Zhongshan rd., Shanghai 200062, China

[4] Instituto de Ciências e Tecnologia, Universidade Federal de São Paulo, R. Sena Madureira, 1500 – Vila Clementino, São Paulo 04021-001, Brasil

[5] National Research University – Higher School of Economics, 25/12 Bolshaya Pecherskaya str., Nizhny Novgorod 603155, Russia

***e-mail:** alhil@inbox.ru

Abstract. To study the characteristics of the spread of the COVID-19 pandemic and introduce timely and effective measures, there is a need for models that can predict the impact of various restrictive factors on COVID-19 disease dynamics. In this regard, it seems expedient to employ agent-based models that can take into account various characteristics of the population (for example, age distribution and social activity) and restrictive measures, testing, etc., as well as random factors that are usually omitted in traditionally used modifications of Susceptible-Infected-Recovered (SIR) type models. This paper presents the development of the previously proposed agent model for numerical simulation of the spread of COVID-19, namely, the transition from a single-center model, in which all agents interact within one common pool, to a multi-center model, in which the agents under consideration are distributed over several centers of interactions, and are also redistributed over time to other pools. This model allows us to more accurately simulate the epidemic dynamic within one region, when the patient zero usually arrives at the regional center, after which the distribution chains capture the periphery of the region due to pendulum migration. This paper demonstrates the application of the developed model to analyze the epidemic spread in the Nizhny Novgorod region of Russian Federation. Simulated dynamics of the daily number of newly detected cases and COVID-19-associated deaths is in good agreement with official statistics. Modeling results suggest that the actual number of COVID-19 cases is 1.5–3 times higher than the number of reported cases. The developed model also takes into account the process of vaccination. It is shown that with the same modeling parameters, but without vaccination, the third and fourth waves of the pandemic would be characterized by a significant increase in the incidence and the formation of natural immunity, but the number of deaths would exceed the real one by about 9 times.
© 2023 Journal of Biomedical Photonics & Engineering.

Keywords: Dynamics and control of epidemics; COVID-19; agent-based modeling.

Paper #3589 received 23 Jan 2023; revised manuscript received 13 Feb 2023; accepted for publication 13 Feb 2023; published online 16 Mar 2023. doi: 10.18287/JBPE23.09.010306.

1 Introduction

The COVID-19 pandemic has become a real global challenge, which requires reliable methods for modeling the epidemiological process in order to take timely restrictive and preventive measures. Currently, there are several classes of models used to calculate and predict the spread of infections.

Logistic models operate with ordinary differential equations of the first order. Despite their simplicity, such models made it possible to obtain a very correct description of the first wave of the spread of COVID-19 [1]. Generalized logistic models make it possible to take into account a power-law, rather than exponential, increase in the number of cases [2, 3]. Methods of mathematical statistics and machine learning make it possible to build regression [4] and network models [5] of the spread of the disease.

More complex, so-called compartmental models are based on systems of differential equations. In such models, the population is divided into several groups. In the classical SIR model proposed in Ref. [6], three groups are distinguished, namely, susceptible (S), infected (I), recovered (R), and the interaction between them is described in terms of differential equations. In more complex modern models, an even greater number of groups are distinguished. In particular, exposed (E), hospitalized (H), deceased (D), in critical state (C) and others are added [7–9].

A significant drawback of the SIR model and its modifications is the inability to take into account both random factors in the epidemic dynamics and the individual characteristics of specific people. In this regard, to model the spread of an epidemic, it is rational to use agent-based models. Within the framework of such models, the entire population is considered as a set of agents with a selected number of both constant and variable characteristics that determine the strategy of behavior and interaction with other agents in the considered population. The characteristics of the disease (incubation period, probability of infection, etc.), restrictive and preventive measures (self-isolation, social distancing, contact tracing, etc.) are also included as parameters of the model. Agent-based models have demonstrated their effectiveness in calculating the spread of infection in a population of various sizes, for example, among visitors to a supermarket [10], residents of a relatively small [11] or large city [12], and an entire country [13]. In Ref. [14], an agent-based model was developed for modeling the spread of COVID-19 in Russia, taking into account transport routes. The mean-field-type game model is actually a combination of the SIR model (or its modifications) and the agent model, which take into account the rationality of agents: each member of the population seeks to reduce the risk of hospitalization and limit its economic consequences, firms seek to maximize profits while reducing the risk of exposing workers to the risk of infection, public authorities seek to reduce the number of deaths based on cost-effectiveness considerations [15].

Within the framework of agent-based models, it is assumed that all agents belonging to a certain group, for example, an age group, behave in the same way. The effectiveness of such models can be increased by introducing new data, such as demographic or transport data, and transition to the so-called multicenter agent model, in which the population is considered as a set of several separate pools of agents with different behavioral characteristics. Thus, in Ref. [16], a simulation of the spread of COVID-19 in several schools was performed, taking into account, for example, kinship (brothers, sisters) and friendships between students from various educational institutions. The paper [17] considers four Chinese cities with the interaction of agents both within each of the cities and between them. The paper [14] presents the country model like a combination of a city models set and a matrix of population flows defined for each day, considering different types of transport links.

The aim of this work is to develop the previously proposed agent model [18, 19] to simulate the spread of COVID-19 in various regions of the Russian Federation. The development is associated with the transition to a multicenter model, which allows considering a separate region of the Russian Federation as a set of regions with population movement between them, as well as taking into account the vaccination process as one of the measures to prevent the spread of the disease.

2 Materials and Methods

2.1 Multicentral Agent-Based COVID-19 Spread Model

The previously developed single-center agent-based COVID-19 spread model with the Monte Carlo method implementation is described in detail in Ref. [19]. Within the framework of the proposed approach, a set of agents $\mathfrak{N}$ representing the population of the chosen region is considered. Each agent $a_n \in \mathfrak{N}$ is characterized by a set of daily changing Boolean states (“alive”, “infected”, “contagious”, “with symptoms of a disease”, etc.) that determine its behavior (interaction with a common pool of agents, self-isolation, etc.). The model presented in Ref. [19] assumes that every agent interacts with all the others, and the probability of spreading the disease is determined by the total number of non-isolated agents. Table 1 presents the main parameters of the previously proposed single-center model.

In order to generalize the developed model to the multi-center case, all agents from the common pool are distributed among n_c pools of smaller size, which correspond to the districts of the region (regional center and peripheral cities). The number of agents N_i in each i-th pool corresponds to the population of the i-th district or city, and the total number of agents in these pools is equaled to the population of the region N: $N = \sum_{i=1}^{n_c} N_i$. For each agent, the index i of its initial pool (i.e. hometown or district) is stored. During the modeling a certain percentage p_t of agents aged from 18 to 65 in each pool, excepting the population of regional center, receive

the binary status of "pendulum migrant", which means that they periodically move from native city to the regional center for working purpose. The p_t value distribution by pools (districts of the region) is chosen empirically, taking into account the distance of a particular city/district from the regional center, while the percentage of commuting migrants among the agents of the general pool is 15%, which is consistent with information available in open sources.

In the simulation, all agents that initially have the "infected" status are assigned to the regional center, and agents with the "pendulum migrant" status change their pool to the regional center from Monday to Friday, returning to the original pool on Saturday and Sunday. Thus, the mechanism of spreading the disease from the regional center to the entire region is implemented. This assumption is consistent with the general trends in the spread of imported epidemics, when the "patient zero" usually appears in the regional center.

Table 1 Values of main parameters employed for Nizhny Novgorod Region in single-center model in paper [19].

Parameter	**Value**
Probability of symptoms manifestation	0.3
Daily death probability in critical state	0.06–0.10
Average weekly number of agents infested by a spreader	4.6
Probability of isolation decision for agents with symptoms manifestation	0.5
Self-isolation index	1.0–3.0

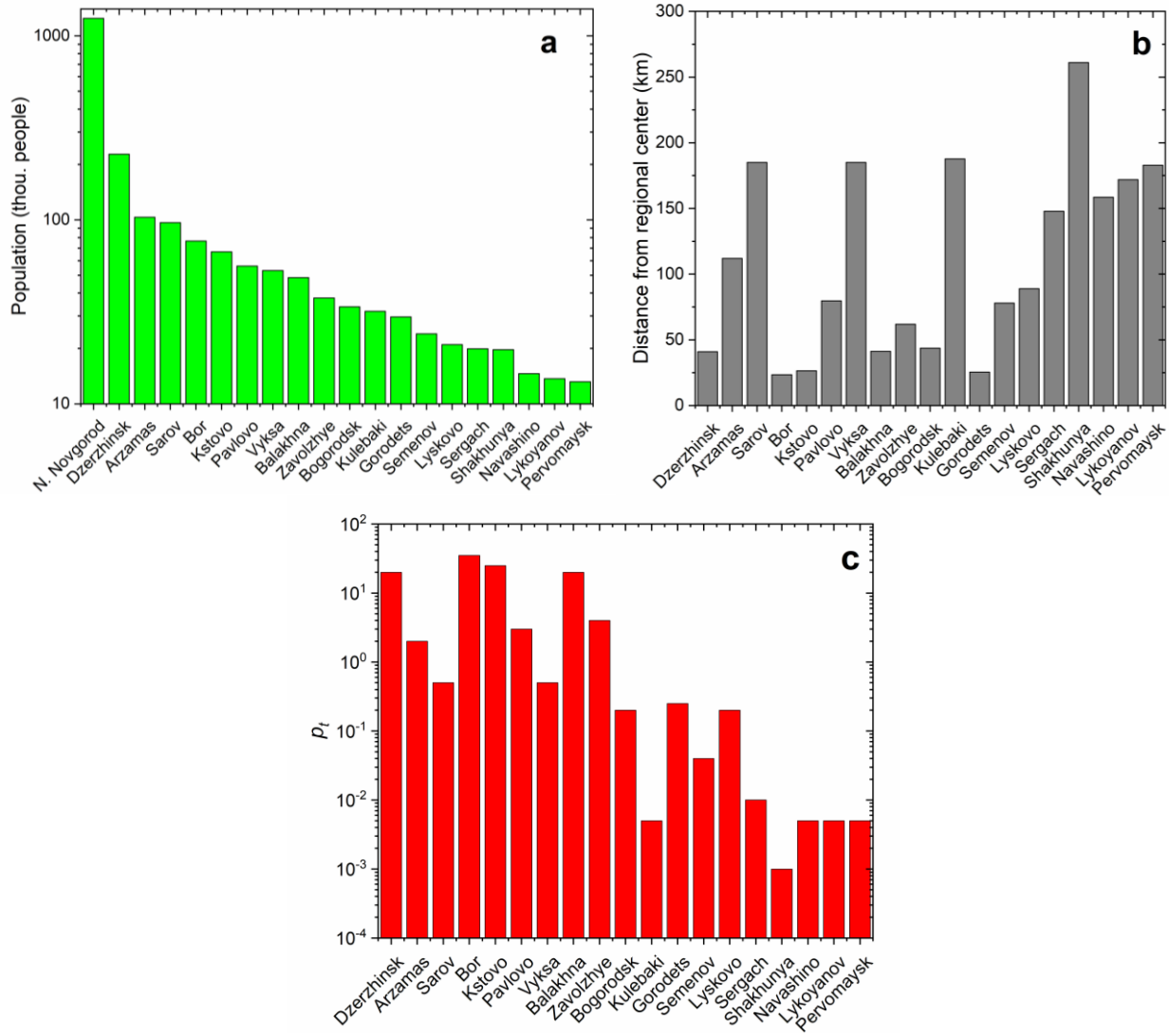


Fig. 1 (a) Population of Nizhny Novgorod Region districts and cities included into modeling; (b) distance from chosen district/city to regional center (Nizhny Novgorod); (c) distribution of agents with "pendulum migrant" status with the respect to chosen districts/cities in modeling.

2.2 Accounting for Vaccination in Modeling

For more precise modeling of the 3rd and 4th waves of the spread of COVID-19, the ability to account for the vaccination process was implemented into developed model. For this purpose, data on partial vaccination of the population in the Russian Federation from January 1, 2021 to December 31, 2021 was taken from open sources [20]. The daily number of partially vaccinated people N_i^{vacc} is calculated in proportion to the share of the region population in the population of the country.

Following the nomenclature previously suggested in Ref. [19], we introduce the additional Boolean state "vaccinated" (α_n^9) that is also set as 'false' (0) at the initialization of the simulation for all agents.

In the simulation the vaccinated group $\mathfrak{V}$ is determined each simulation day in the following way:

$$\mathfrak{V}: R_p(N_i^{vacc}, \{a_n | h_n \geq 18\} \backslash \mathfrak{P}), \quad (1)$$

where $R_p(j, \mathfrak{A})$ is a random permutation of j elements from set $\mathfrak{A}$: N_i^{vacc} is the total number of vaccinated taken at day i corresponding to the official statistics data; h_n is an agent age parameter; $\mathfrak{P}$ is the group of agents, who are unavailable for vaccination. The latter group contains agents with states "symptomatic" (α_n^3), "in critical state" (α_n^4), "dead" (α_n^5) or "positive test" (α_n^8):

$$\mathfrak{P}: (\{a_n | \alpha_n^3 = 1\} \cup \{a_n | \alpha_n^4 = 1\} \cup \cup \{a_n | \alpha_n^5 = 1\} \cup \{a_n | \alpha_n^8 = 1\}). \quad (2)$$

On each simulation day agents from the vaccinated group change the status to "vaccinated":

$$\alpha_n^9 = 1 | a_n \in \mathfrak{V}. \quad (3)$$

For each vaccinated agent, the day of vaccination t_n^{vac} is stored. After a period of vaccination and antibodies formation T_a equaled 42 days (21 days is the interval between two stages of vaccination and 21 days is the period of antibodies formation), the probability of infection p_{is} for a vaccinated agent during the interaction with a pool of other agents is artificially reduced by 20 times (immunity formation). Duration of immunity T_i chosen in the model is 6 months.

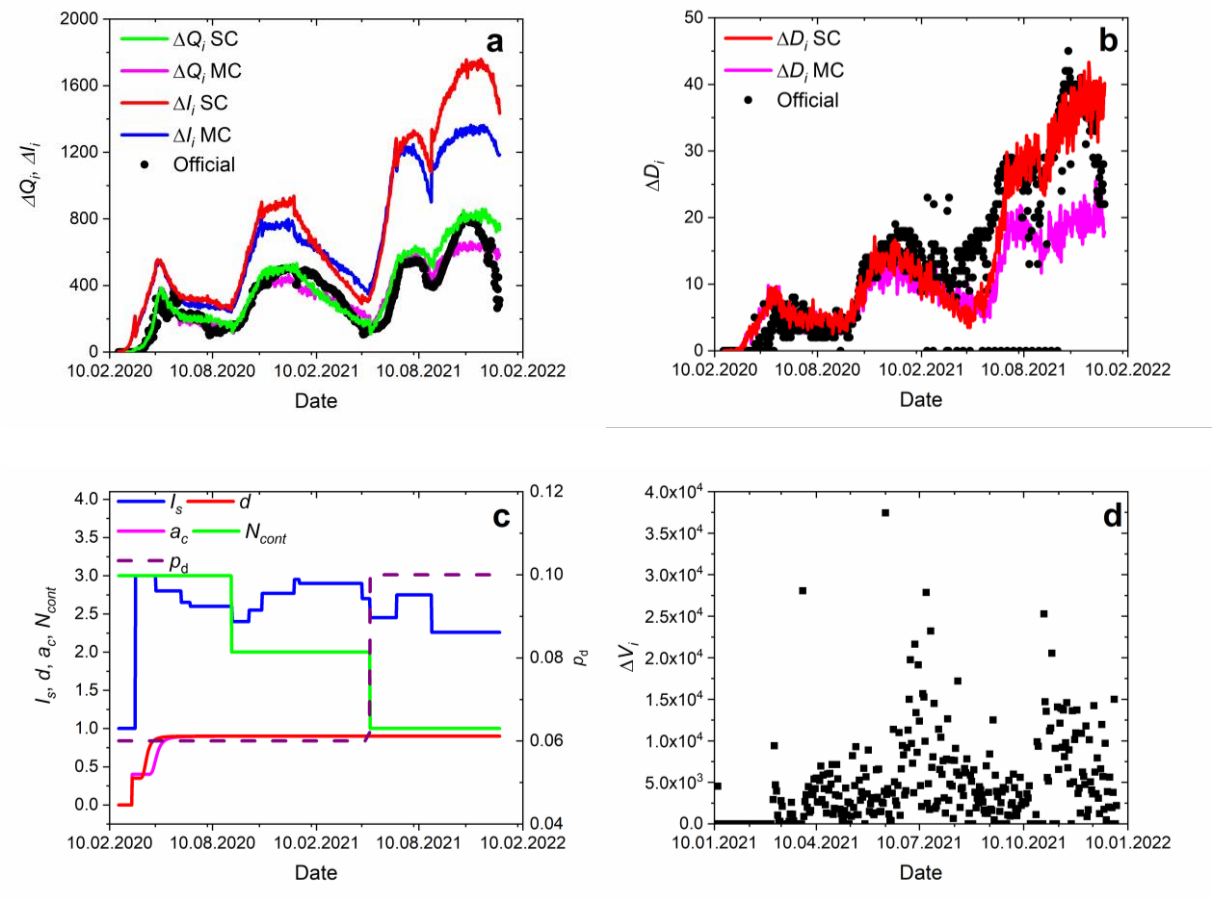


Fig. 2 Daily dynamics of (a) newly revealed (ΔQ_i) and real total number of COVID-19 cases (ΔI_i) and (b) COVID-19 associated deaths (ΔD_i) in Nizhny Novgorod Region calculated in single-center (SC) and multi-central (MC) models along with official data (Official). Simulation parameters: (c) I_s – self-isolation index, d – fraction of tested agents with symptoms, a_c – tests sensitivity, N_{cont} – number of traced contacts, p_d – death probability in critical state, (d) ΔV_i – daily dynamics of vaccinated agents.

$$\widetilde{p_{is}} = \begin{cases} p_{is} \mid \alpha_n^9 = 0 \\ \frac{p_{is}}{20} \mid \alpha_n^9 = 1,\ t_{vac} + T_a \le i < t_{vac} + T_a + T_i \end{cases} \quad (4)$$

2.3 Multicentral Modeling Parameters

Simulation of four waves of COVID-19 spread was performed for Nizhny Novgorod region ($N = 3.3 \cdot 10^6$) and included the days from February 26, 2020 to December 31, 2021. All parameters, including the temporal characteristics of the disease and the prevalence rate, the distribution of agents by age, the probability of death of an agent in critical condition, etc. corresponds to those previously used in modeling the first two waves of the spread of COVID-19 [19], while for the 3rd and 4th waves an empirical selection of parameters was performed. The number of cities and districts in the region n_c is chosen to be 20 during simulation (smaller administratively distinguished districts are combined with neighboring larger ones). Fig. 1 shows the population of selected cities and districts of the Nizhny Novgorod region, as well as their distance from the regional center and a given percentage of commuting migrants in them.

3 Results

Fig. 2 shows the dynamics of the spread of COVID-19 in the Nizhny Novgorod region, calculated within the framework of single- and multi-center agent models, as well as the parameters used in the modeling: self-isolation index (I_s), the proportion of tested agents with symptoms of the disease (d), test sensitivity (a_c), the number of tested contact agents (N_{cont}), the probability of death of an agent in critical condition (p_d). Similar to Ref. [19], we simulate daily dynamics of daily newly revealed COVID-19 cases (ΔQ_i) which gave the positive test result on a certain day, total number of daily new cases including those that remain undetected (ΔI_i), and daily lethal COVID-19 associated cases (ΔD_i).

As can be seen from Fig. 2, the total number of detected cases of COVID-19 in the region is still in good agreement with official statistics during the movement from a single-center to a multicenter model.

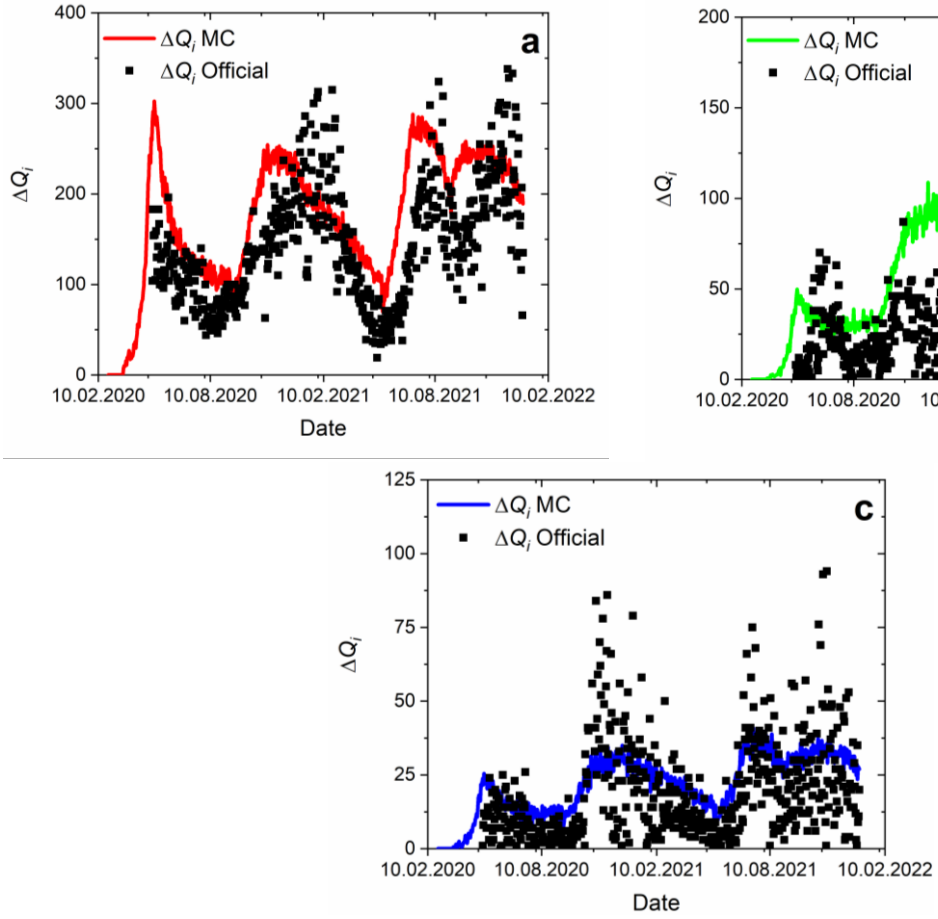


Fig. 3 Daily dynamics of newly revealed ΔQ_i COVID-19 cases, calculated with multicenter (MC) model for (a) regional center – Nizhny Novgorod, (b) Dzerzhinsk, and (c) Bor. Simulation parameters are similar to those in Figs. 2c, d.

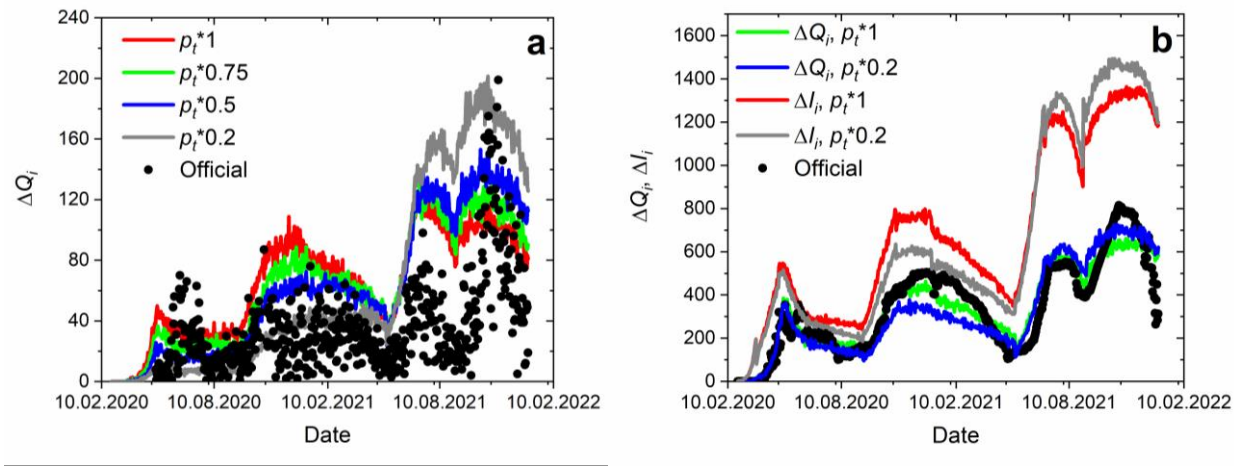


Fig. 4 Daily dynamics of newly revealed ΔQ_i COVID-19 cases, calculated with multicenter model for (a) Dzerzhinsk and (b) Nizhny Novgorod Region with different percentage p_t of pendulum migrants along with official statistics data (Official).

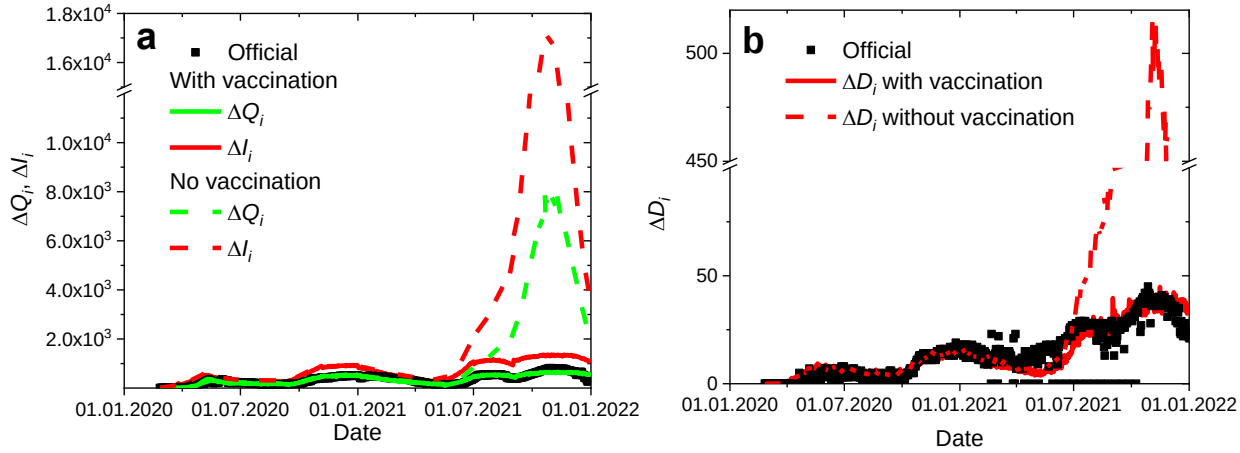


Fig. 5 Daily dynamics of (a) newly revealed (ΔQ_i) and real total number of COVID-19 cases (ΔI_i) and (b) COVID-19 associated deaths (ΔD_i) in Nizhny Novgorod Region calculated with multi-central model with and without accounting for vaccination.

The discrepancies between the curves for single- and multicenter models are due to the fact that within the framework of a single-center model, all agents participating in the modeling are affected from the very beginning, while in the case of a multicenter model, infection begins from the regional center, where the infection enters from outside the system under consideration. The resulting model scenario shows that some of the infected are not detected, and the total number of infections exceeds the number of detected cases by 1.5–3 times, and this ratio increases for later waves.

Fig. 3 shows the dynamics of the spread of COVID-19 in Nizhny Novgorod (regional center), as well as the cities of Dzerzhinsk and Bor, calculated within the multicenter model.

As can be seen from Fig. 3, during the first wave of the spread of COVID-19 (spring-summer 2020), the dynamics of newly detected cases is determined mainly by Nizhny Novgorod (the regional center), while the curves for regional cities show a characteristic peak around May. During the second wave (autumn 2020–winter 2021), the self-isolation index does not reach the values of the first wave, and therefore there is a significant increase in new cases detected in the regions of the region, and the difference between them becomes quite significant. A similar trend can be traced in the case of the 3rd and 4th waves (spring 2021–December 2021).

It should be noted that the difference between the official statistics and simulated data for new cases for certain districts and cities of the Nizhny Novgorod region was not a minimization parameter of the model, but the comparison shows a fairly good agreement between simulated and official data.

Fig. 4 presents the results obtained in multicenter model with a variation in the percentage of pendulum migrants. The distribution of the percentage of pendulum migrants in Fig. 1 is taken as the initial one; the caption to Fig. 4 shows the coefficient by which the corresponding values are multiplied.

As can be seen from Fig. 4a, the developed multicenter agent model provides an adequate estimation of the spread of the disease in a particular city in the region. The discrepancy between the simulation results and official statistics is explained by the overestimated number of agents in the pool corresponding to a particular city in the framework of numerical simulation. An increase in the fraction of pendulum migrants in a particular city has a more significant impact during the first wave of the pandemic compared to the second (Fig. 4a), since restrictive measures are relaxed during the second wave (Fig. 2c). At the same time, during the first and second waves of the spread of COVID-19, an increase in the percentage of pendulum migrants expectedly leads to an increase in detected cases of the disease in a particular city, but during the third and fourth waves, an inverse relationship is observed. It is explained by the fact that in the case of a lower percentage of pendulum migrants, a significant part of infection spreading the agents remain in their pools and interact with the agents within it, and not with the rest. At the same time, the total number of newly revealed cases across the region is in good agreement with official statistics for the region, both in the case of the base percentage of commuters and for a much lower percentage (Fig. 4b).

In order to analyze the impact of the vaccination process on the spread of the disease, modeling was performed with parameters corresponding to those presented in Fig. 2c, but without vaccination of agents. The results are presented in Fig. 5 showing the comparison of the daily numbers of total and detected cases in scenarios with and without vaccination.

Fig. 5 clearly demonstrates the effectiveness of vaccination of the population as a preventive measure in the spread of the disease. It is shown that in the absence of vaccination with the same parameters of the model, a sharp increase in the incidence is observed, leading to the formation of herd immunity by the beginning of 2022, however, at the cost of high mortality (a difference of about 9 times compared to the number of deaths during the vaccination of the population). The significant difference between the curves with and without vaccination is due to the greatly relaxed restrictive measures during the third and fourth waves of the spread of COVID-19 and the decrease in the number of contacts traced (Fig. 2c).

4 Conclusion

The paper presents the enhancement of an agent-based model that simulates the COVID-19 spread dynamics using the Monte Carlo method. The developed multicenter model considers a region as a set of separate districts in which agents interact with each other while the mechanism of interaction between districts described through consideration of pendulum migration. The proposed approach made it possible to simulate four waves of the spread of COVID-19 in the Nizhny Novgorod region and demonstrates good agreement with official statistics. In the future, the model can be improved by increasing the number of districts included in the simulation, considering the travel of agents not only from regional cities to the regional center, but also between regional cities itself, and also taking into account the different nature of restrictive measures in the regional cities. For more correct modeling results, precise information about the number of pendulum migrants in specific cities/districts of the region is required.

The developed agent-based model also includes the ability to account for the vaccination process during the spread of infection. The results obtained for the dynamics of newly detected and real total number of COVID-19 cases show that even with a significant weakening of restrictive measures, vaccination of the population can reduce the number of cases and COVID-19–associated deaths by about 9 times, which clearly demonstrates the need for vaccination and its effectiveness.

Disclosures

All authors declare that there is no conflict of interests in this paper.

Acknowledgements

The study is supported by RFBR (project no. 20-51-80004), CNPq (project no. 441016/2020-0), and NSFC (project no. 82161148012).

References

1. T. Carletti, D. Fanelli, and F. Piazza, “COVID-19: The unreasonable effectiveness of simple models,” Chaos, Solitons & Fractals: X 5, 100034 (2020).
2. E. Aviv-Sharon, A. Aharoni, “Generalized logistic growth modeling of the COVID-19 pandemic in Asia,” Infectious Disease Modelling 5, 502–509 (2020).
3. N. T. P. Pang, A. Kamu, M. A. M. Kassim, and C. M. Ho, “Monitoring the impact of Movement Control Order (MCO) in flattening the cummulative daily cases curve of Covid-19 in Malaysia: A generalized logistic growth modeling approach,” Infectious Disease Modelling 6, 898–908 (2021).
4. A. S. Ahmar, E. B. Del Val, “SutteARIMA: Short-term forecasting method, a case: Covid-19 and stock market in Spain,” Science of The Total Environment 729, 138883 (2020).
5. C. Katris, “A time series-based statistical approach for outbreak spread forecasting: Application of COVID-19 in Greece,” Expert Systems with Applications 166, 114077 (2021).

6. W. O. Kermack, A. G. McKendrick, "A contribution to the mathematical theory of epidemics," Proceedings of the Royal Society of London. Series A, Containing Papers of a Mathematical and Physical Character 115(772), 700–721 (1927).
7. S. He, Y. Peng, and K. Sun, "SEIR modeling of the COVID-19 and its dynamics," Nonlinear Dynamics 101(3), 1667–1680 (2020).
8. S. Mwalili, M. Kimathi, V. Ojiambo, D. Gathungu, and R. Mbogo, "SEIR model for COVID-19 dynamics incorporating the environment and social distancing," BMC Research Notes 13(1), 352 (2020).
9. L. López, X. Rodo X, "A modified SEIR model to predict the COVID-19 outbreak in Spain and Italy: simulating control scenarios and multi-scale epidemics," Results in Physics 21, 103746 (2021).
10. F. Ying, N. O'Clery, "Modelling COVID-19 transmission in supermarkets using an agent-based model," Plos One 16(4), e0249821 (2021).
11. Md. S. Shamil, F. Farheen, N. Ibtehaz, I. M. Khan, and M. S. Rahman, "An agent-based modeling of COVID-19: validation, analysis, and recommendations," Cognitive Computation, 1–12 (2021).
12. N. Hoertel, M. Blachier, C. Blanco, M. Olfson, M. Massetti, F. Limosin, and H. Leleu, "Facing the COVID-19 epidemic in NYC: a stochastic agent-based model of various intervention strategies," MedRxiv 20076885, (2020).
13. N. Hoertel, M. Blachier, C. Blanco, M. Olfson, M. Massetti, M. S. Rico, F. Limosin, and H. Leleu, "A stochastic agent-based model of the SARS-CoV-2 epidemic in France," Nature Medicine 26(9), 1417–1421 (2020).
14. G. N. Rykovanov, S. N. Lebedev, O. V. Zatsepin, G. D. Kaminskii, E. V. Karamov, A. A. Romanyukha, A. M. Feigin, and B. N. Chetverushkin, "Agent-based simulation of the COVID-19 epidemic in Russia," Herald of the Russian Academy of Sciences 92(8), 747–755 (2022).
15. H. Tembine, "Covid-19: data-driven mean-field-type game perspective," Games 11(4), 51 (2020).
16. A. M. Hernández-Hernández, R. Huerta-Quintanilla, "Managing school interaction networks during the COVID-19 pandemic: Agent-based modeling for evaluating possible scenarios when students go back to classrooms," Plos One 16(8), e0256363 (2021).
17. L. Kou, X. Wang, Y. Li, X. Guo, and H. Zhang, "A multi-scale agent-based model of infectious disease transmission to assess the impact of vaccination and non-pharmaceutical interventions: The COVID-19 case," Journal of Safety Science and Resilience 2(4), 199–207 (2021).
18. M. Kirillin, E. Sergeeva, A. Khilov, D. Kurakina, and N. Saperkin, "Monte Carlo simulation of the covid-19 spread in early and peak stages in different regions of the Russian Federation using an agent-based modelling," in Saratov Fall Meeting, Chinese-Russian workshop on Biophotonics and Bioimaging-2020 1 (2020).
19. M. Kirillin, A. Khilov, V. Perekatova, E. Sergeeva, D. Kurakina, I. Fiks, N. Saperkin, M. Tang, Y. Zou, E. Macau, and E. Pelinovsky, "Simulation of the first and the second waves of COVID-19 spreading in Russian Federation regions using an agent-based model," Journal of Biomedical Photonics & Engineering 9(1), 010302 (2023).
20. E. Mathieu, H. Ritchie, L. Rodés-Guirao, C. Appel, C. Giattino, J. Hasell, B. Macdonald, S. Dattani, D. Beltekian, E. Ortiz-Ospina, and M. Roser, Coronavirus (COVID-19) Vaccinations, Our World in Data (accessed 30 November 2022). [http://ourworldindata.org/covid-vaccinations?country=RUS].

Intraoperative Optical Diagnostics of Uterine Microcirculation during Myomectomy

Elena Potapova[1*], Nikolai Polenov[2], Karina Zakuraeva[2], Valentina Krutikova[1], Maria Yarmolinskaya[2], and Igor Kogan[2]

[1] Research and Development Center of Biomedical Photonics, Orel State University, 95 Komsomolskaya str., Orel 302026, Russia

[2] FSBSI "The Research Institute of Obstetrics, Gynecology and Reproductology named after D.O. Ott", 3 Mendeleevskaya line, Saint Petersburg 199034, Russia

***e-mail:** potapova_ev_ogu@mail.ru

Abstract. Previous studies have shown that intraoperative optical diagnostics can be used to solve fundamental and applied problems in gynecology. Our article presents results from experimental *in vivo* intraoperative measurements of endogenous fluorescence and blood perfusion in various sections of the uterus, myometrium, endometrium, myomas, and pseudocapsule in female patients undergoing myomectomy. We found that myomas have different blood supply and fluorescence level at wavelength 365 nm depending on their growth intensity and size, most likely due to collagen accumulation in the extracellular matrix and changes in the vascular architecture. The possibility of laser Doppler flowmetry to assess endometrial perfusion is also demonstrated for investigating the effect of myomas of different types on endometrial tissue blood supply. The results obtained can be used to provide a better understanding of pathological processes in uterine leiomyoma, thus helping physicians to choose treatment strategies.
© 2023 Journal of Biomedical Photonics & Engineering.

Keywords: optical methods; fluorescence spectroscopy; laser Doppler flowmetry; gynecology; fibroids; myomectomy.

Paper #5659 received 8 Feb 2023; accepted for publication 6 Mar 2023; published online 16 Mar 2023. doi: 10.18287/JBPE23.09.010307.

1 Introduction

Uterine leiomyoma (LM) ranks second among gynecological pathologies and is the most common benign tumor in both women of reproductive age and perimenopausal women. The incidence of the disease is reported to reach up to 70-80% of woman, depending on the cohort studied and the methods of diagnosis [1–3]. Normally, the vascular network of the uterus has an organized structure, and the myometrium has a large number of capillaries to ensure adequate blood supply during pregnancy [4, 5]. LM is characterized by overgrowth of myometrial smooth muscle cells containing extracellular matrix components (fibronectin, collagen, proteoglycan) [6]. During its growth, the extracellular matrix forms a pseudocapsule around the myoma, which separates it from the normal myometrium [7].

Laparoscopic myomectomy is a surgical treatment for symptomatic LM. Despite uterine LM being one of the most well-studied uterine diseases, and laparoscopic myomectomy being a recognized treatment method, a number of unresolved questions remain. The issues of surgical tactics, including the need to preserve the pseudocapsule when removing the myoma during the laparoscopic intracapsular myomectomy [8], and the development of substantiated medical grounds for myomectomy in women with intramural myomas who are planning pregnancy, remain important [9]. The application of optical technologies, which are currently being successfully introduced in minimally invasive surgery [10–13], may help to solve some fundamental and applied problems in gynecology.

Minimally invasive myomectomy techniques aim to remove LM while preserving healthy uterus. Postoperative vascularization of the myometrium is

crucial for the regeneration of damaged tissue, and the myoma pseudocapsule is hypothesized to play an important role in this process. The removal of the pseudocapsule during myomectomy can lead to a decrease in neuropeptides and nerve fibers, and hence, to poor physiological healing of the myometrium with increased fibrosis due to hypoxia and ischemia [14].

To date, little data have been accumulated on instrumental study of the blood supply in the fibrovascular network surrounding LMs. A. Malvasi et al. examined the structure of a pseudocapsule using electron microscopy and concluded that this anatomical structure contains a neurotransmitter-rich vascular network like that of a neurovascular bundle [15]. Standard transvaginal ultrasound mapping of myomas has demonstrated increased blood flow in the pseudocapsule, which is described as a surrounding ring containing clearly visualized vessels [16, 17]. Additional information about the state of blood microcirculation in the pseudocapsule and surrounding tissues can provide new knowledge about the organization of blood supply in this structure.

The search for new objective criteria for performing myomectomies in patients planning pregnancy is of current interest in practical gynecology. The necessity of surgical treatment of intramural LMs in patients with infertility who are planning pregnancy using assisted reproductive technologies based solely on LM size exceeding 4 cm in the absence of clinical manifestations is a controversial issue [9]. A promising direction in surgical treatment for women of reproductive age is the development of new minimally invasive methods to assess the impact of LM on reproductive function. One indicator of the functional state of the endometrium is whether or not it has an adequate blood supply. Among the instrumental diagnostic methods to study blood flow, there are existing results from Doppler studies of both endometrial and sub-endometrial blood flow in patients with intramural LMs. In particular, 3D power Doppler parameters were observed to be similar in patients with and without small intramural LMs [18].

Optical diagnostic methods provide great opportunities for the study of blood microcirculation and metabolic processes in biological tissues. The method of laser Doppler flowmetry (LDF) is based on measuring the Doppler shift in the spectrum of the reflected laser signal scattered by moving red blood cells. This technology allows one to carry out a dynamic quantitative assessment of perfusion in the microvascular bed of various tissues. In gynecology LDF is recognized as a highly sensitive method for measuring localized endometrial perfusion [19–23]. The use of wavelet transforms to analyze these LDF signals offers broad diagnostic opportunities. This approach helps to evaluate the contribution of individual microvascular bed components to the modulation of blood flow in various physiological and pathological processes [24, 25].

Fluorescence spectroscopy (FS) is based on the excitation of fluorescence in biological tissues by UV or visible light, with subsequent registration of the emitted radiation on a spectrometer (after passing through appropriate filters). FS is widely used to assess the condition of biological tissues in medicine, including gynecology [26, 27]. The most prominent endogenous fluorophores in biological systems are NADH, flavins, collagen and elastin, porphyrin, etc.

Total fluorescence emission contains a lot of diagnostically important information, since it represents the sum of contributions of fluorophore autofluorescence.

In the present study, we used optical techniques of FS and LDF in two separate examinations to demonstrate intraoperative assessments of perfusion and metabolic characteristics of myometrium, myoma, pseudocapsule and endometrium. The first examination was focused on the study of myoma perfusion in women with rapidly growing large-sized LMs and with slowly growing LMs below 5 cm. The second examination evaluated the effect of intramural and intramural-submucosal LMs on endometrial perfusion and metabolic characteristics.

2 Methods and Materials

2.1 The System for Intraoperative Assessment of Perfusion-Metabolic Changes in Biological Tissues

Measurements were performed using a specially designed fiber-optic system (Fig. 1), which implements both FS and LDF methods and includes measurement channels of the diagnostic complex “LAKK-M” (SPE “LAZMA” Ltd, Russia) and a laparoscopic fiber-optic probe (the main units were designed together with SPE “LAZMA” Ltd, Russia) [10]. The probe has a 3 mm diameter rigid part, which provides control and fixation at the analysis point.

To record optical signals, the laparoscopic fiber-optic probe was inserted into the pelvic cavity through the instrumental channel.

In the LDF channel, tissues were probed by laser radiation and subsequent registration of dynamic light scattering at a wavelength of 1064 nm. The LDF 3.2.0.441 program (SPE “LAZMA” Ltd.) was used for frequency analysis of the registered signals. This program implements a continuous wavelet transform using a complex Morlet wavelet as an analyzing wavelet.

In the FS channel, radiation sources with wavelengths of 365 nm and 450 nm, respectively, can be used to excite endogenous fluorescence of biomarkers. Fluorescence spectra across the range of 350–820 nm are then recorded by the spectrometer.

2.2 Study Protocol

The pilot experimental studies were carried out at the Research Institute of Obstetrics, Gynecology and Reproductology named after D.O. Ott (St. Petersburg, Russia), and involved a total of 18 female patients.

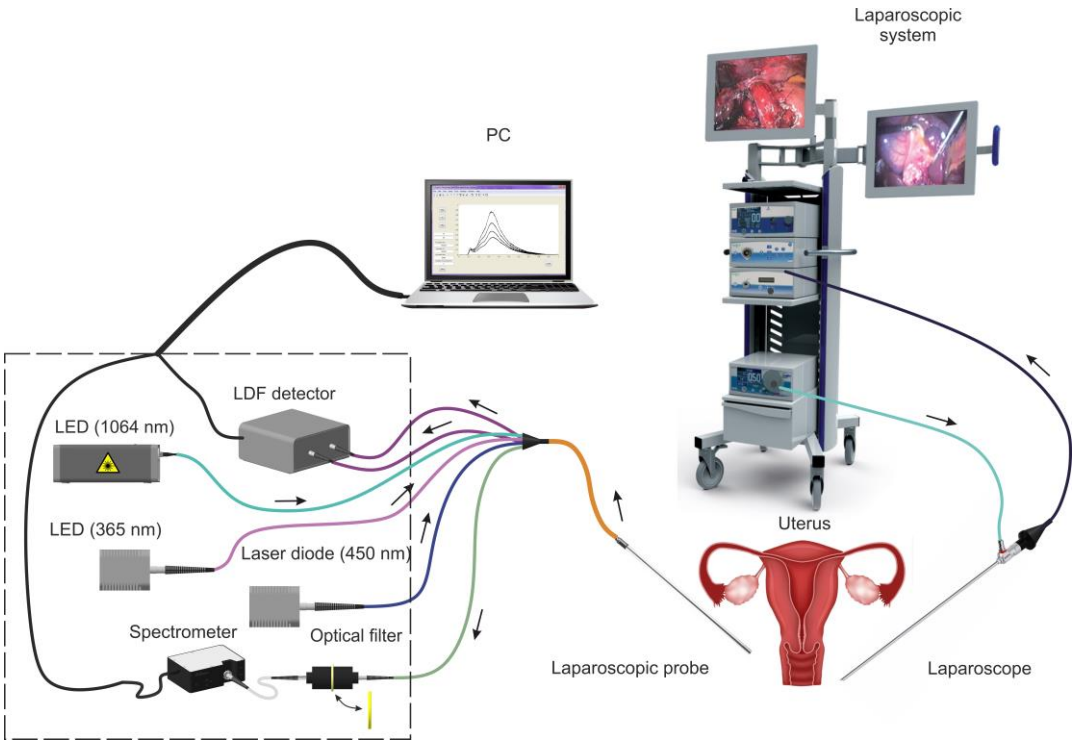


Fig. 1 Schematic of the experimental setup for intraoperative study of perfusion-metabolic changes in biological tissues.



Fig. 2 Monitoring of fiber-optic probe position during intraoperative myometrial perfusion measurement by LDF method.

The studies were performed as an additional diagnostic procedure within a scheduled surgery and were approved by the ethical committee of the Research Institute of Obstetrics, Gynecology and Reproductology named after D. O. Ott (minutes of the meeting No 110, June 10, 2021). The study site was chosen for each woman based on the convenience of the main gynecological surgery.

Participants signed an informed consent indicating their voluntary willingness to participate in the study. LDF and FS signals were recorded in the tissues of the endometrium, myometrium, myoma, and pseudocapsule. The position of the fiber-optic probe was controlled via the monitor on the laparoscopic rack (Fig. 2).

Fig. 3 shows the exemplary records of blood perfusion signal, the corresponding wavelet spectra and fluorescence spectra from the uterine LM.

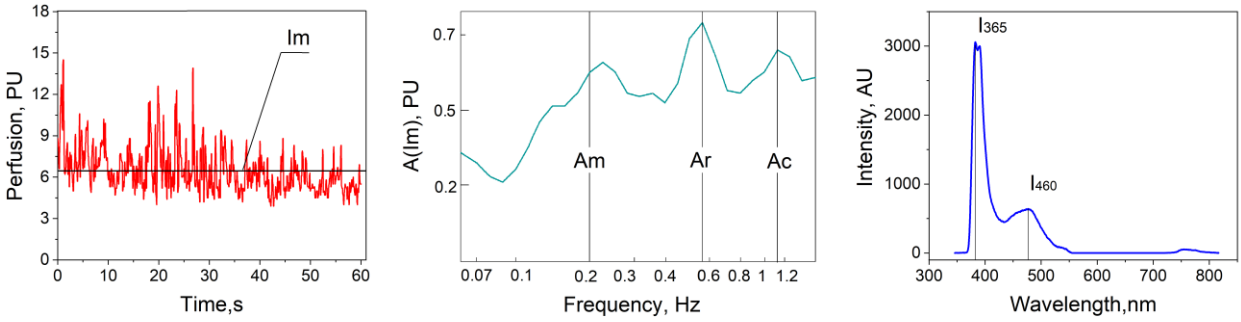
The duration of LDF signal recording was at least 1 min, to enable further selection of 60 s recordings without motion artifacts. Blood microcirculation index (Im, perfusion units, PU) was analyzed during the experimental studies according to the standard technique (Fig. 3a) [11, 25, 28]. Due to the limited duration of LDF recordings, the time-averaged amplitude of blood flow oscillations was estimated by the maximum values in three frequency bands: myogenic (Am) range: 0.047–0.145 Hz, respiratory (Ar) range: 0.2–0.4 Hz, and cardiac (Ac) range: 0.8–2 Hz, respectively (Fig. 3b) [24].

The FS channel was used to record fluorescence spectra excited at a wavelength of 365 nm. Parameters for analysis were the maximum fluorescence amplitudes (I_{365}) in the range of 450–470 nm, normalized to the intensity of backscattered excitation radiation (I_{460}), respectively ($I_{460norm}$), associated with NADH and collagen fluorophores (Fig. 3c) [29].

2.3 Examinations

2.3.1 Examination 1. Study of Perfusion and Metabolic Changes in Myometrium, Myoma and Pseudocapsule in Women with Different Sizes and Intensities of Myoma Growth Rate.

The study involved 8 women of reproductive age with uterine LM diagnosed by pelvic ultrasonography. Pregnant women, peri- and postmenopausal women (cessation of menstruation for > 1 year), women with endometriosis, adenomyosis or other pelvic neoplasms,



(a) (b) (c)

Fig. 3 Exemplary blood perfusion record (a), the corresponding wavelet spectra (b), and fluorescence spectra (c) from the uterine LM.

and patients with pelvic inflammatory diseases were excluded. Two groups were defined based on the medical history: group 1 – women with LMs of large size (6–8 cm) and having rapid growth (more than 4 weeks of conditional pregnancy per year); group 2 – patients with smaller LMs (4–5 cm), abnormal uterine bleeding, growth dynamics not exceeding 1 cm per year. LDF and FS signals were recorded in myometrium, myoma, and pseudocapsule tissues.

2.3.2 Examination 2. Effects of Intramural and Intramural-Submucosal Myomas on Endometrial Perfusion

Twenty patients with myomas of different types were examined. Two groups were identified, based on the location of myomas: group I – 10 patients with one or several intramural-submucosal LMs not exceeding 5 cm in size, type 2–3 according to FIGO (The International Federation of Gynecology and Obstetrics) uterine myoma classification; group II – 10 patients with intramural, intramural-subserosal LMs up to 5 cm in diameter, type 5–6 (FIGO). Exclusion criteria were hypergonadotropic ovarian insufficiency, chronic endometritis, and prior history of endometrial hyperproliferative disease. The studies were performed on the 8–11 days of the menstrual cycle. LDF and FS signals were recorded only in endometrial tissue.

2.4 Statistical Analysis

Statistical analysis was performed using Origin Pro software (OriginLab Corporation). Hemodynamic parameters and fluorescence intensities are shown as the Me(Q1–Q3), where Me is the median, Q1 is the first quartile, Q3 is the third quartile. Given the limited sample size, the nonparametric Mann-Whitney *U*-test was chosen for checking the reliability of statistical differences in the results. The *p*-value of less than 0.05 was considered significant.

3 Results and Discussion

3.1 Examination 1. Study of Perfusion and Metabolic Changes in Myometrium, Myoma and Pseudocapsule in Women with Different Sizes and Intensity of Myoma Growth Rate.

The results are presented in Table 1. Group 1 – women with large myomas of 6–8 cm, with rapid growth (more than 4 weeks of conditional pregnancy per year) are designated as "↑↑growth of myoma"; group 2 – patients with myomas of 4–5 cm, with myoma growth not exceeding 1 cm per year – "↑growth of myoma".

Table 1 Hemodynamic parameters and fluorescence intensities of uterine tissues.

Parameter	Group	Im, PU	Am, PU	Ar, PU	Ac, PU	$I_{460norm}$, AU
Myometrium	↑↑growth of myoma	5.1* (3.4–6.8)	0.54* (0.45–0.73)	0.51* (0.32–0.80)	0.56* (0.39–0.83)	0.49* (0.48–0.49)
	↑growth of myoma	9.3 (9.2–9.3)	1.03 (0.90–1.13)	1.21 (1.12–1.60)	1.22 (1.06–1.27)	0.30 (0.27–0.32)
Myoma	↑↑growth of myoma	3.2* (2.3–3.8)	0.47* (0.36–0.58)	0.39* (0.31–0.42)	0.34* (0.27–0.37)	0.60* (0.49–0.61)
	↑growth of myoma	7.0 (6.4–7.8)	0.76 (0.62–1.03)	0.76 (0.69–0.95)	0.75 (0.69–0.99)	0.25 (0.23–0.27)
Pseudocapsule	↑↑growth of myoma	5.8* (4.9–6.0)	0.64 (0.51–0.78)	0.57* (0.41–0.68)	0.52 (0.38–0.66)	–
	↑growth of myoma	7.9 (7.0–8.2)	0.83 (0.65–0.94)	0.84 (0.63–2.41)	0.76 (0.56–0.81)	7.9 (7.0–8.2)

*$p < 0.05$.

Processing of the data showed that myometrial blood microcirculation was a variable parameter in both groups (5.1 [3.4–6.8] PU and 9.3 [9.2–9.3] PU respectively). However, the level of myometrial perfusion was significantly higher in the group with slow–growing myomas. The high value of myometrial blood microcirculation in group 2 and the amplitudes of myogenic (1.03 [0.90–1.13] PU) and cardiac (1.22 [1.06–1.27] PU) oscillations confirms the assumption that the characteristic feature of uterine blood circulation is the vasomotor nature of blood movement through microvessels. At the same time, intermittent blood flow in the uterine capillaries is primarily due to changes in the tone of precapillary sphincters [30]. The results also show that the mean perfusion measured in the pseudocapsule was higher in the group of "↑growth of myoma" than in the comparison group (5.8 [4.9–6.0] PU vs 7.9 [7.0–8.2] PU). A similar pattern was observed in myomas: 3.2 [2.3–3.8] PU and 7.0 [6.4–7.8] PU, respectively.

Thus, opposite to the expectations that higher perfusion would be observed in the group of patients with rapidly growing myoma, we obtained the opposite result. These findings may be explained as follows. In the presence of triggering factors, the increasing size of the LM may cause deformation or even complete compression of the vessels of the pseudocapsule feeding the LM. Unlike the normal vascular network, which matures and stabilizes rapidly, the blood vessels of myomas have structural and functional characteristics. The vascular network of LMs has a chaotic organization, with tortuosity and increased vascular permeability. This means that once LMs reach a certain size, their blood supply is impaired to some extent, resulting in reduced microcirculation [31]. Further studies including Doppler sonography are needed to clarify the true reasons for the higher level of blood microcirculation in the group with slow-growing LMs.

For additional analysis, a portion of the results from Table 1 were grouped together and presented as a bar chart in Fig. 4.

Fig. 4a demonstrates that the pseudocapsule is better supplied with blood than the myomas in both groups, confirming evidence that this structure is the vascular capsule surrounding the LM and providing its nutrition [7, 32]. An interesting histopathological feature of LMs is the difference in structure of their vascular network compared with the adjacent myometrium. Previous studies have shown that LMs have lower vascular area and microvascular density than adjacent myometrium [33–35]. It was long believed that solid tumors require increased microvascular density to support the growth of the tumor mass. In the present study, no statistical differences were found between the blood microcirculation levels of LMs and the adjacent myometrium, but Fig. 4a shows that the perfusion of myomas is generally lower.

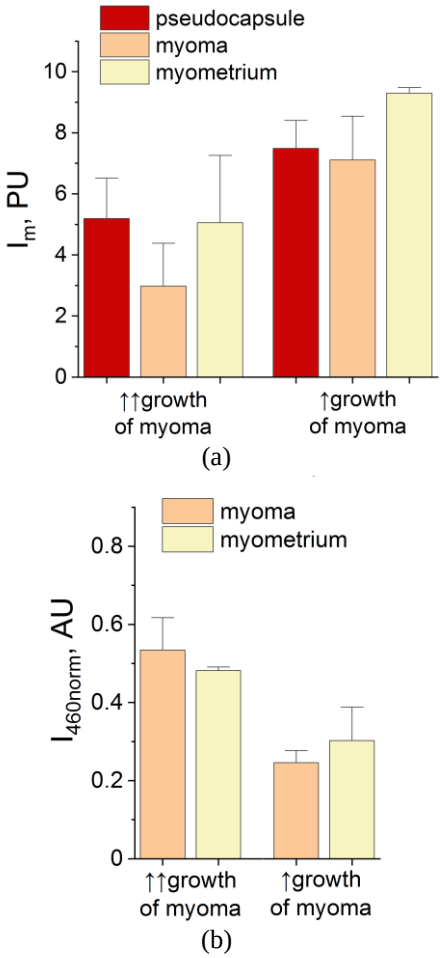


Fig. 4 Indices of microcirculation (a) and fluorescence intensity (b) of uterine tissues in the compared groups.

Of particular interest is the result that blood microcirculation in the pseudocapsule of rapidly growing LMs ("↑↑growth of myoma" group) significantly exceeds the blood supply of the myoma itself (5.8 [4.9–6.0] PU vs 3.2 [2.3–3.8] PU). When analyzing FS channel data, we noticed that $I_{460norm}$ fluorescence signal increased in rapidly growing large LMs along with decreased perfusion compared to the surrounding myometrium (0.60 [0.49–0.61] AU vs 0.49 [0.48–0.49] AU) (Fig. 4b). We associate this observation with the fact that myomas in the rapid growth group probably continue to enlarge as a result of both increased myocyte proliferation and synthesis and deposition of extracellular matrix [36]. Collagen from the extracellular matrix can be present to varying degrees in tumors of the compared groups. It is known that at the late stages of development, collagen can account for 10–50% of tumor mass of myomas, which exceeds the content of collagenous component in myometrium [37, 38]. In addition, there is an observation that insufficient blood supply to the tumor itself develops at this stage and this eventually leads to interstitial ischemia [36]. This also corresponds to the greater decrease in perfusion in the myoma compared to the surrounding pseudocapsule in the group with large LMs and rapid growth.

Table 2 Hemodynamic parameters and endometrial fluorescence intensities depending on myoma type.

Parameter	Im, PU	Am, PU	Ar, PU	Ac, PU	$I_{460norm}$, AU
I group, type 2–3 (FIGO)	3.6* [2.0–5.3]	0.3 [0.3–0.4]	0.2 [0.2–0.4]	0.4 [0.2–0.6]	0.45 [0.29–0.47]
II group, type 5–6 (FIGO)	7.6 [6.0–8.6]	0.4 [0.3–0.7]	0.3 [0.2–0.5]	0.5 [0.3–0.9]	0.26 [0.23–0.34]

*$p < 0.05$.

Improvements in our knowledge of uterine tissue blood microcirculation can play an important role in understanding the role of the pseudocapsule as a distinct anatomical and surgical structure, as well as in understanding tumor growth processes, which will further help to determine the correct treatment tactics for patients with uterine LM.

3.2 Examination 2. Effects of Intramural and Intramural–Submucosal Myomas on Endometrial Perfusion

The results obtained by optical diagnostic methods are summarized in Table 2.

Unfortunately, we cannot compare the endometrial blood flow values given in Table 2 with those measured by LDF in previous studies [19, 20], owing to the differences in probes used and study protocols.

Processing of the obtained data showed a statistically significant decrease of the microcirculation index in the endometrial tissues in the group of patients with type 2–3 LMs (FIGO) of the uterine cavity (3.6 [2.0–5.3] PU vs 7.6 [6.0–8.6] PU). There is a tendency towards decreased oscillation amplitudes across all bands of endometrial microcirculatory flow regulation, however this did not reach statistical significance. Although the LDF method is semi–quantitative and does not give absolute values for blood flow, it can be used to perform a qualitative assessment of endometrial microhemodynamics.

When analyzing FS data, we noticed an increase in the $I_{460norm}$ signal in group I patients compared to group II patients: 0.45 [0.29–0.47] AU vs 0.26 [0.23–0.34] AU. It is known that in the proliferative phase of the menstrual cycle (during which all patients were studied), type VI collagen is abundantly present in the endometrium [39]. We suggest that the increased $I_{460norm}$ signal may be related to abnormal collagen accumulation in the extracellular matrix or to the accumulation of NADH, associated with circulatory insufficiency and the initial stages of hypoxia [40].

Women with unexplained infertility are known to have impaired endometrial perfusion [41], implying that an adequate blood supply to the endometrium is required for implantation. Our results suggest that endometrial blood perfusion in patients with LMs of the uterine cavity is reduced and may be the cause of impaired receptivity. Meanwhile, intramural LMs retain high endometrial tissue perfusion. Thus, optical technologies are promising diagnostic methods for the analysis of endometrial blood supply.

To date, there are conflicting reports that the intramural localization of LM negatively affects fertility. Physicians should have clear criteria to perform myomectomy and to predict the effectiveness of surgical treatment for uterine LMs. Surgery significantly increases the risk of myoma recurrence and has complications associated with uterine scarring. Additional diagnostic information may help in choosing a treatment strategy for LMs, including non–surgical options [9].

4 Conclusion and Limitations

The described experimental studies confirm the possibility of intraoperative tissue diagnostics through optical methods of FS and LDF during myomectomy. The introduction of these methods into endoscopic gynecological surgery seems promising, extending the capabilities of standard laparoscopy by allowing the surgeon to obtain additional information about perfusion and metabolic characteristics of uterine tissues.

These technologies still have some limitations. They are spectroscopic methods providing single–point measurements, which creates a potential source of error. However, this measurement uncertainty can be minimized by standardizing the location at which signals are registered, and by performing multiple measurements to gain average values.

An important limitation of the presented work is the small number of patients included in each sample, especially in Examination 1. The study requires further data collection in order to form clinical guidelines. The article aims to demonstrate the potential of multimodal optical diagnostics during endoscopic procedures in gynecology.

Another limitation of the study was the lack of a control group. The composition of the control group was limited by a number of problems, including ethical ones: (1) it is impossible to perform laparoscopy in completely healthy patients without any medical grounds; (2) comparison with conditionally healthy myometrium in patients undergoing diagnostic laparoscopy for infertility can also be inaccurate, as most of them may be diagnosed with pathological changes in the endometrium, hormonal disorders, or inflammatory diseases of the pelvic organs; (3) if there are no visible myomas, we cannot be sure that the patient does not have adenomyosis, as there are currently no non–invasive diagnostic methods that provide an accurate diagnosis.

The research described is a pilot study. The data obtained during this study indicate the need for its extension. We suggest that further collection of data on the blood supply to the pseudocapsule may provide additional evidence to justify preserving this structure and preferably performing a laparoscopic intracapsular myomectomy. In our work, we also demonstrated that type 5–6 (FIGO) myomas do not affect endometrial microcirculation in the way that type 2–3 (FIGO) myomas do. A subsequent study will look more closely at patients with type 5–6 (FIGO) myomas checked by Doppler sonography. The practical value will lie in the development of more valid medical grounds for myomectomy in this LM localization.

Disclosures

All authors declare that there is no conflict of interests in this paper.

Acknowledgements

The authors acknowledge the support of the Russian Science Foundation under project No. 21-15-00325.

References

1. E. A. Stewart, C. L. Cookson, R. A. Gandolfo, and R. Schulze-Rath, "Epidemiology of uterine fibroids: a systematic review," BJOG: An International Journal of Obstetrics & Gynaecology 124(10), 1501–1512 (2017).
2. E. Giuliani, S. As-Sanie, and E. E. Marsh, "Epidemiology and management of uterine fibroids," International Journal of Gynecology & Obstetrics 149(1), 3–9 (2020).
3. R. Sparic, L. Mirkovic, A. Malvasi, and A. Tinelli, "Epidemiology of uterine myomas: a review," International Journal of Fertility and Sterility 9(4), 424–435 (2016).
4. E. Aitken, A. Khaund, S. A. Hamid, D. Millan, and S. Campbell, "The normal human myometrium has a vascular spatial gradient absent in small fibroids," Human Reproduction 21(10), 2669–2678 (2006).
5. G. Farrer-Brown, J. O. W. Beilby, and M. H. Tarbit, "The blood supply of the uterus: 1. Arterial vasculature," BJOG: An International Journal of Obstetrics & Gynaecology 77(8), 673–681 (1970).
6. M. S. Islam, A. Ciavattini, F. Petraglia, M. Castellucci, and P. Ciarmela, "Extracellular matrix in uterine leiomyoma pathogenesis: a potential target for future therapeutics," Human Reproduction Update 24(1), 59–85 (2018).
7. A. Tinelli, A. Malvasi, "Uterine fibroid pseudocapsule," in Uterine Myoma, Myomectomy and Minimally Invasive Treatments, A. Tinelli, A. Malvasi (Eds.), Springer, Cham, 73–93 (2015). ISBN: 978-3-319-10304-4.
8. A. Tinelli, B. S. Hurst, G. Hudelist, D. A. Tsin, M. Stark, L. Mettler, M. Guido, and A. Malvasi, "Laparoscopic myomectomy focusing on the myoma pseudocapsule: technical and outcome reports," Human Reproduction 27(2), 427–435 (2012).
9. S. Supermaniam, W. L. Thye, "Intramural fibroid and fertility–to operate or not," Gynecology Pelvic Medicine 2, 1–16 (2019).
10. K. Kandurova, V. Dremin, E. Zherebtsov, E. Potapova, A. Alyanov, A. Mamoshin, Y. Ivanov, A. Borsukov, and A. Dunaev, "Fiber–Optic System for Intraoperative Study of Abdominal Organs during Minimally Invasive Surgical Interventions," Applied Sciences 9(2), 217 (2019).
11. E. Zherebtsov, M. Zajnulina, K. Kandurova, E. Potapova, V. Dremin, A. Mamoshin, S. Sokolovski, A. Dunaev, and E. U. Rafailov, "Machine Learning Aided Photonic Diagnostic System for Minimally Invasive Optically Guided Surgery in the Hepatoduodenal Area," Diagnostics 10(11), 873 (2020).
12. E. V. Potapova, E. S. Seryogina, V. V. Dremin, D. D. Stavtsev, I. O. Kozlov, E. A. Zherebtsov, A. V. Mamoshin, Yu. V. Ivanov, and A. V. Dunaev, "Laser speckle contrast imaging of blood microcirculation in pancreatic tissues during laparoscopic interventions," Quantum Electronics 50(1), 33 (2020).
13. E. Potapova, V. Dremin, E. Zherebtsov, A. Mamoshin, and A. Dunaev, "Multimodal Optical Diagnostic in Minimally Invasive Surgery," in Multimodal Optical Diagnostics of Cancer, V. V. Tuchin, J. Popp, and V. P. Zakharov (Eds.), Springer, Cham, 397–424 (2020).
14. A. Tinelli, A. Favilli, R. B. Lasmar, I. Mazzon, S. Gerli, X. Xue, and A. Malvasi, "The importance of pseudocapsule preservation during hysteroscopic myomectomy," European Journal of Obstetrics & Gynecology and Reproductive Biology 243, 179–184 (2019).
15. A. Malvasi, A. Tinelli, C. Cavallotti, M. Morroni, D. A. Tsin, C. Nezhat, M. Stark, and L. Mettler, "Distribution of substance P (SP) and vasoactive intestinal peptide (VIP) in pseudocapsules of uterine fibroids," Peptides 32(2), 327–332 (2011).
16. Y. Sun, L. Zhu, X. Huang, C. Zhou, and X. Zhang, "Immunohistochemical localization of nerve fibers in the pseudocapsule of fibroids," European Journal of Histochemistry 58(2), 2249 (2014).
17. A. C. Fleischer, "Color Doppler sonography of uterine disorders," Ultrasound Quarterly 19(4), 179–189 (2003).
18. E. H. Yu Ng, C. C. W. Chan, O. S. Tang, W. S. B. Yeung, and P. C. Ho, "Endometrial and subendometrial blood flow measured by three–dimensional power Doppler ultrasound in patients with small intramural uterine fibroids during IVF treatment," Human Reproduction 20(2), 501–506 (2005).

19. M. Hickey, G. Krikun, P. Kodaman, F. Schatz, C. Carati, and C. J. Lockwood, "Long–term progestin–only contraceptives result in reduced endometrial blood flow and oxidative stress," The Journal of Clinical Endocrinology & Metabolism 91(9), 3633–3638 (2006).
20. L. Bungum, S. Kullander, and J. M. Maltau, "Laser Doppler flowmetry of human endometrial microvasculature: A preliminary communication," Acta Obstetricia et Gynecologica Scandinavica 75(2), 178–181 (1996).
21. M. Jinno, T. Ozaki, M. Iwashita, Y. Nakamura, A. Kudo, and H. Hirano, "Measurement of endometrial tissue blood flow: a novel way to assess uterine receptivity for implantation," Fertility and Sterility 76(6), 1168–1174 (2001).
22. B. J. Gannon, C. J. Carati, and C. J. Verco, "Endometrial perfusion across the normal human menstrual cycle assessed by laser Doppler fluxmetry," Human Reproduction 12(1), 132–139 (1997).
23. C. J. Verco, C. J. Carati, and B. J. Gannon, "Human endometrial perfusion after tubal occlusion," Human Reproduction 13(2), 445–449 (1998).
24. A. Stefanovska, M. Bracic, and H. D. Kvernmo, "Wavelet analysis of oscillations in the peripheral blood circulation measured by laser Doppler technique," IEEE Transactions on Biomedical Engineering 46(10), 1230–1239 (1999).
25. A. V. Dunaev, V. V. Sidorov, A. I. Krupatkin, I. .E Rafailov, S. G. Palmer, N. A. Stewart, S. G. Sokolovski, and E. U. Rafailov, "Investigating tissue respiration and skin microhaemocirculation under adaptive changes and the synchronization of blood flow and oxygen saturation rhythms," Physiological Measurement 35(4), 607–621 (2014).
26. N. Ramanujam, M. F. Mitchell, A. Mahadevan, S. Thomsen, A. Malpica, T. Wright, N. Atkinson, and R. Richards-Kortum, "Development of a multivariate statistical algorithm to analyze human cervical tissue fluorescence spectra acquired in vivo," Lasers in Surgery and Medicine: The Official Journal of the American Society for Laser Medicine and Surgery, 19(1), 46–62 (1996).
27. M. Lucovnik, R. J. Kuon, and R. E. Garfield, "Assessment of parturition with cervical light–induced fluorescence and uterine electromyography," Computational and Mathematical Methods in Medicine 2013, 165913 (2013).
28. M. A. Filina, E. V. Potapova, I. N. Makovik, E. V. Zharkih, V. V. Dremin, E. A. Zherebtsov, A. V. Dunaev, V. V. Sidorov, A. I. Krupatkin, E. A. Alimicheva, G. I. Masalygina, and V. F. Muradyan, "Functional changes in blood microcirculation in the skin of the foot during heating tests in patients with diabetes mellitus," Human Physiology 43(6), 693–699 (2017).
29. A. V. Dunaev, V. V. Dremin, E. A. Zherebtsov, I. E. Rafailov, K. S. Litvinova, S. G. Palmer, N. A. Stewart, S. G. Sokolovski, and E. U. Rafailov, "Individual variability analysis of fluorescence parameters measured in skin with different levels of nutritive blood flow," Medical Engineering & Physics 37(6), 574–83 (2015).
30. R. H. Kardon, D. B. Farley, Dr. P. M. Heidger Jr., and D. E. van Orden, "Intraarterial cushions of the rat uterine artery: a scanning electron microscope evaluation utilizing vascular casts," The Anatomical Record 203(1), 19–29 (1982).
31. R. Tal, J. H. Segars, "The role of angiogenic factors in fibroid pathogenesis: potential implications for future theray," Human Reproduction Update 20(2), 194–216 (2014).
32. J. A. Walocha, J. A. Litwin, and A. J. Miodoński, "Vascular system of intramural leiomyomata revealed by corrosion casting and scanning electron microscopy," Human Reproduction 18(5), 1088–1093 (2003).
33. R. Casey, P. A. W. Rogers, and B. J. Vollenhoven, "An immunohistochemical analysis of fibroid vasculature," Human Reproduction 15(7), 1469–1475 (2000).
34. C. Poncelet, P. Madelenat, G. Feldmann, F. Walker, and E. Darai, "Expression of von Willebrand's factor, CD34, CD31, and vascular endothelial growth factor in uterine leiomyomas," Fertility and Sterility 78(3), 581–586 (2002).
35. G. Weston, A. C. Trajstman, C. E. Gargett, U. Manuelpillai, B. J. Vollenhoven, and P. A.W. Rogers, "Fibroids display an anti-angiogenic gene expression profile when compared with adjacent myometrium," Molecular Human Reproduction 9(9), 541–549 (2003).
36. G. P. Flake, A. B. Moore, D. Sutton, N. Flagler, N. Clayton, G. E. Kissling, B. W. Hall, J. Horton, D. Walmer, S. J. Robboy, and Darlene Dixon, "The life cycle of the uterine fibroid myocyte," Current Obstetrics and Gynecology Reports 7(2), 97–105 (2018).
37. G. P. Flake, A. B. Moore, N. Flagler, B. Wicker, N. Clayton, G. E. Kissling, S. J. Robboy, and D. Dixon, "The natural history of uterine leiomyomas: morphometric concordance with concepts of interstitial ischemia and inanosis," Obstetrics and Gynecology International 2013, 285103 (2013).
38. V. Aleksandrovych, T. Bereza, M. Sajewicz, J. A Walocha, and K. Gil, "Uterine fibroid: common features of widespread tumor," Folia medica Cracoviensia 55(1), 61-75 (2015).
39. J. D. Aplin, A. K. Charlton, and S. Ayad, "An immunohistochemical study of human endometrial extracellular matrix during the menstrual cycle and first trimester of pregnancy," Cell and Tissue Research 253(1), 231–240 (1988).
40. A. Mayevsky, G. G. Rogatsky, "Mitochondrial function in vivo evaluated by NADH fluorescence: from animal models to human studies," American Journal of Physiology-Cell Physiology 292(2), C615–C640 (2006).
41. N. J. Raine–Fenning, B. K. Campbell, N. R. Kendall, J. S. Clewes, and I. R. Johnson, "Endometrial and subendometrial perfusion are impaired in women with unexplained subfertility," Human Reproduction 19(11), 2605–2614 (2004).

Highly Stable 11-MUA Capped Gold Nanobipyramid for Refractive Index Sensing

Prajna N. Deviprasada and Rajeev K. Sinha*
Department of Atomic and Molecular Physics, LG-1, Academic Block 5, MIT Campus, Manipal Academy of Higher Education, Manipal 576104, Karnataka, India

***e-mail:** rajeev.sinha@manipal.edu

Abstract. Gold nanobipyramids (Au NBPs) are nanostructures with narrow plasmon resonances, which make them suitable for sensing applications. In the present work, Au NBPs of different aspect ratios were synthesized using a seed-mediated growth method by tuning the seed volume. The usual capping molecule CTAB was replaced by 11-mercaptoundecanoic acid (11-MUA), and the nanoparticle stability was studied. The 11-MUA capped NBPs were found to be more stable compared to the CTAB capped NBPs. The bulk refractive index sensitivities of all Au NBPs of CTAB and 11-MUA capped NBPs were measured using sucrose solutions of different weight percentages (0–30%). 11-MUA capped Au NBPs showed better refractive index sensitivity than CTAB capped Au NBPs. The NBPs of aspect ratio 3 showed maximum sensitivity of 353 nm/RIU. © 2023 Journal of Biomedical Photonics & Engineering.

Keywords: localized surface plasmon resonance (LSPR); gold nanobipyramids; refractive index sensing.

Paper #3580 received 13 Jan 2023; revised manuscript received 18 Feb 2023; accepted for publication 23 Feb 2023; published online 24 Mar 2023. doi: 10.18287/JBPE23.09.010308.

1 Introduction

The localized surface plasmon resonance (LSPR) is an optical phenomenon observed in metal nanostructures with dimensions much smaller than the wavelength of light. The phenomenon appears due to the resonant oscillation of the conduction electrons on the surface of nanostructures [1, 2]. The band maxima in the LSPR spectra are extremely sensitive to the refractive index (RI) of the surrounding medium [1, 2]. The RI sensitivity of metal nanostructures forms the basis of many cost-effective LSPR-based biosensors [1, 3]. Anisotropic nanoparticles are more suitable candidates for sensing applications due to their large surface charge polarizability and associated local field enhancement. This enables the LSPR sensing of small molecules to large biomolecules [4–7]. Several metal nanoparticles, such as gold, silver, copper, and platinum, show appreciable LSPR phenomena. However, nanoparticles of gold and silver have absorption bands in the visible spectral regions, making them widely used in sensing applications. Gold nanoparticles are comparatively more stable, biocompatible, and widely used in several biomedical applications [8–11].

Although the higher chemical and structural stability of Au nanostructures over Ag nanostructures make them preferable for LSPR sensing, the higher width of plasmon bands appears to be a limiting factor for their regular use. Among different shapes of gold nanoparticles, gold nanobipyramids (Au NBPs) shows narrow width of plasmon bands. Further, the wavelength tunability of the longitudinal plasmon band of Au NBPs is possible in the visible and near-IR spectral region by tuning their length and aspect ratio. The sharp edges in NBPs result in high field enhancement, making them highly suitable for biosensing applications [12, 13]. In the recent past, an appreciable amount of work has been performed on the synthesis of gold nanobipyramids. The bi-pyramidal shape of Au nanoparticles was first reported by Jana et al. [14]. Later, Liu and co-workers developed a synthesis method using CTAB as a surfactant [15]. Other than CTAB, capping agents like PVP [16], CTBAB [17], and sodium oleate as secondary surfactant [18] were also used to synthesize NBPs.

In the recent past, we have worked on the synthesis and evaluation of refractive index (RI) sensitivity of silver [19–22] and gold nanostructures [23]. In

continuation, here we report the synthesis and RI sensitivity of Au nanobipyramids. The replacement of cetyltrimethylammonium bromide (CTAB) in CTAB capped Au NBPs by 11-mercaptoundecanoic acid (11-MUA) is performed to improve the stability of the Au NBPs. The RI sensitivity of CTAB and 11-MUA capped Au NBPs were investigated using various concentrations of sucrose. Compared to nanosphere and nanorods, nanobipyramid shows better sensitivity and higher figure-of-merit, making them more suitable for LSPR-based sensing applications.

2 Materials and Methods

For the synthesis and conjugation of gold nanobipyramids, hydrogen tetrachloroaurate (III) hydrate ($HAuCl_4 \bullet 3H_2O$), cetyltrimethylammonium chloride (CTAC), cetyltrimethylammonium bromide (CTAB), 11-mercaptoundecanoic acid (11-MUA), nitric acid (HNO_3), silver nitrate ($AgNO_3$), and 8-hydroquinoline (HQL) were procured from Sigma Aldrich. L–ascorbic acid (AA) and sodium borohydride ($NaBH_4$) were purchased from Loba Chemie Pvt Ltd. and Spectrochem, respectively. All the chemicals were used as received.

3 Experimental Methods

3.1 Synthesis of Gold NBPs

Au NBPs were synthesized following the seed-mediated method reported earlier by Chateau et al. [24]. For the preparation of seed nanoparticles, 80 μL of 25 mM $HAuCl_4$ and 72 μL of 0.25 M HNO_3 were added to 8mL of 66 mM CTAC. The mixture was stirred at 1000 rpm for a few minutes, and 100 μL of 50 mM $NaBH_4$ in NaOH was added. The solution colour was changed to brownish orange. After one minute of stirring, 60 μL of 0.1 M citric acid was added, and the seed solution was heated at 85 ºC for 1 h in a water bath.

The growth solution was prepared using 20 mL of 46.5 mM CTAB, 200 μL of 25 mM $HAuCl_4$, 165 μL of 5 mM $AgNO_3$, and 255 μL of 0.4 M ethanoic HQL. Seed solutions of varying volumes (0.2, 1, and 1.6 mL) were added in three 25 mL glass beakers. Then, 20 mL of growth solution was added to each beaker and placed in a hot-air oven set at 85 ºC for 10 min.

3.2 Functionalization of Au NBP with 11-Mercaptoundecanoic Acid

The functionalization of NBPs was performed using the sodium borohydride method reported earlier [25]. Before functionalization, the excess precursors and other reagents were removed from the NBPs by centrifuging the colloidal solution at 8000 rpm for 15 min. The yellow supernatant was discarded, and the residue was re-dispersed in 10 mM CTAB solution. For functionalization, 1.5 mL of 100 mM $NaBH_4$ was added to 15 mL of CTAB-capped NBPs. The solution was kept undisturbed for one hour, and 800 μL of 10 mM 11 MUA was added. After overnight incubation, the excess of 11 MUA was removed from the colloidal solution through centrifugation at 8000 rpm for 12 min. The supernatant was discarded, and the NBPs were re-dispersed in water.

3.3 Characterization of Au Nanobipyramids

The synthesized Au NBPs were characterized using UV-Visible absorption spectroscopy and Field emission scanning electron microscopy (FESEM). The absorption spectra were recorded using our lab-built setup, explained elsewhere [20]. The FESEM images of Au NBPs were recorded in Carl Zeiss Gemini SEM 300 instrument. The FESEM samples were prepared by immobilizing the NBPs on a glass coverslip using (3-Aminopropyl) trimethoxysilane (APTMS). The aspect ratio of NBPs were calculated using ImageJ software [26].

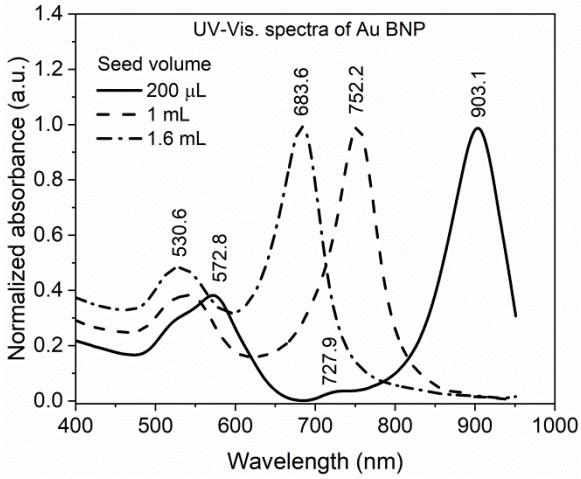


Fig. 1 Normalized absorption spectra of Au NBPs synthesized with different seed volumes.

4 Results and Discussions

4.1 Spectroscopic and Morphological Characterization of Au NBP

The NBPs are assumed as two pentagonal twinned bipyramids connected base to base. This structure forms due to the controlled growth of penta-twinned CTAC-capped seed particles in the growth solution. The growth solution is made up of gold precursor, stabilizing agent as CTAB, and shape directing agent as silver nitrate. The adsorption of silver as silver bromide on the surface of gold seeds leads to the anisotropic growth. The HQL as a mild reducing agent, reduces the reaction rate in the growth solution and favors the formation of the bipyramid structure of nanoparticles [27, 28].

The gold NBPs synthesized by the seed-mediated growth method [24] were characterized by UV-Vis spectroscopy using the lab-built setup [20]. The extinction spectra of Au NBP synthesized using seed volumes 200 μL, 1, and 1.6 mL are shown in Fig. 1.

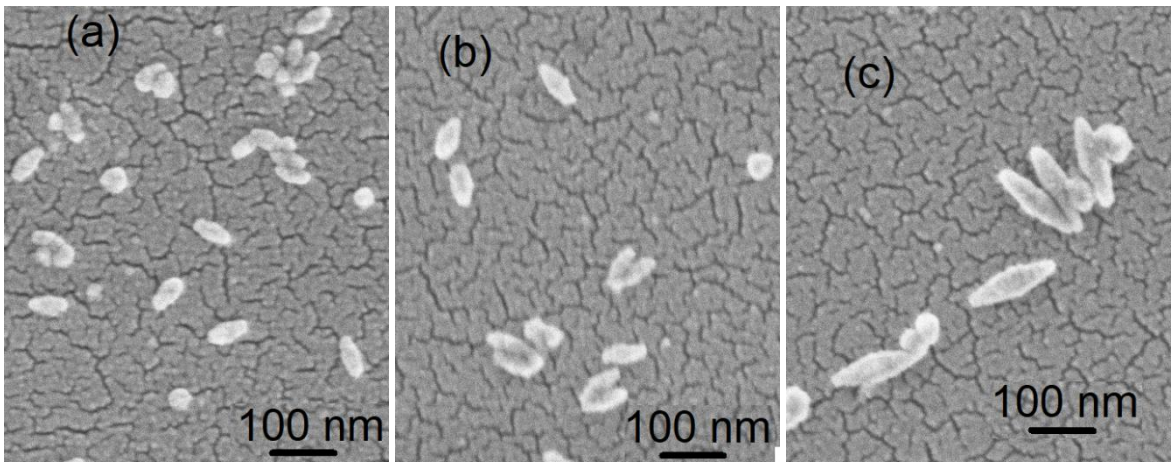


Fig. 2 FESEM images of 11-MUA capped gold nanobipyramids synthesized using (a) 1.6, (b) 1.0, and (c) 0.2 mL of seed volume.

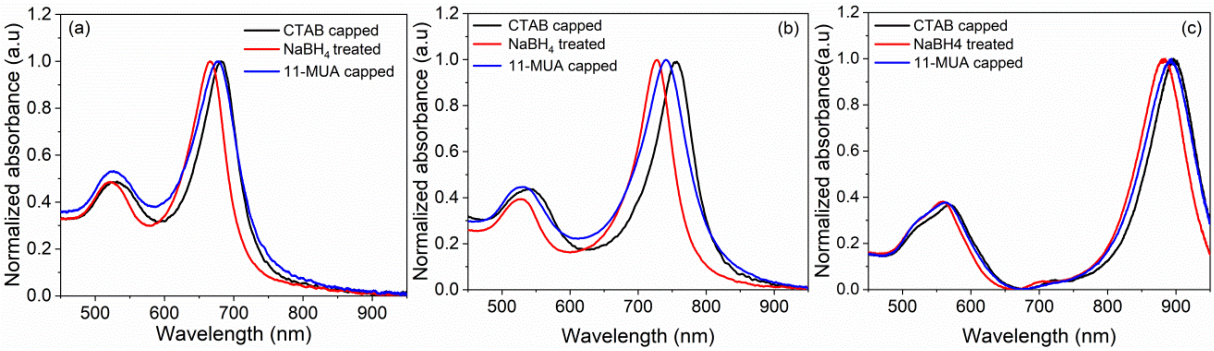


Fig. 3 Absorption spectra of NBPs as synthesized, after $NaBH_4$ treatment and after 11-MUA capping synthesized using (a) 1.6, (b) 1.0, and (c) 0.2 mL seed volume.

As it can be seen in the figure, for all three NBPs, two prominent features were observed, a transverse plasmonic band due to the oscillation of electrons along the short axis and a longitudinal plasmonic band due to the oscillation of electrons along the long axis [17]. The longitudinal plasmon band was observed towards the higher wavelength, and the transverse plasmon band towards the shorter wavelength. For seed volumes 200 µL, 1, and 1.6 mL, longitudinal plasmon bands appear at 903, 752, and 684 nm, respectively, whereas transverse band maxima were observed at the same position at 530.6 nm. The position of the longitudinal plasmon band towards longer wavelength signifies a higher length and aspect ratio of the NBP. Therefore, decreased seed volume resulted in longer NBP with a higher aspect ratio. An increase in the seed volume causes less availability of Au^{3+} ions per seed, resulting in a lower overall aspect ratio of NBPs [29]. The lower aspect ratio is responsible for the observed blue shifts in the longitudinal band position with an increase in the seed volume. For seed volume of 200 µL, two additional bands were seen at 572.8 and 727.9 nm. In a recent work, it is reported that as the length of NBP increases, the multipoles start appearing in the extinction spectrum [30]. The additional band observed at 572.8 nm could be due to the multipolar plasmon resonances, whereas the band at 727.9 nm could be due to a small number of by-products, such as gold nanorods [17].

The FESEM images of synthesized Au NBP are shown in Fig. 2. For imaging purpose, the NBPs were immobilized on a glass coverslip using 3-Aminopropyltrimethoxysilane (APTMS). As seen from the FESEM images, at 1.6 mL of seed volume, nanorice-shaped particles were formed (Fig. 2(a)). The bipyramidal shape of nanoparticles was improved by lowering the seed volume. More elongated bipyramids are formed for 200 µL seed volume, as shown in Fig. 2(c). The aspect ratios of these NBPs were calculated using ImageJ software, and the obtained aspect ratios were 2.0, 2.4, and 3, respectively.

4.2 Surface Functionalization and Stability of NBPs

Although CTAB acts as a stabilizing agent for the synthesized Au NBPs, a considerable blue shift in their longitudinal peaks was observed with time. Also, the

core of the nanoparticle is unapproachable for any biomolecular interactions due to the thick CTAB bilayers on the Au NBPs surface [31]. Therefore, CTAB must be replaced with suitable stabilizing agents which can retain the shape of the NBPs for a long time and make them more suitable for bioconjugation. The ligand exchange process using alkanethiol is a widely used method for the surface functionalization of nanoparticles [32]. While the alkanethiol, 11-MUA in present case, interacts with the NBPs through -SH head group, which has a strong affinity towards gold [13], the terminal carboxylic group (-COOH) can be modified using EDC/NHS chemistry [29] for bioconjugation.

The surface functionalization of Au NBPs by 11-MUA was performed using the sodium borohydride method reported by He et al. for the Au nanorods [25]. In the process, the CTAB-capped NBPs were treated with 50 mM $NaBH_4$. The absorption spectra of NBPs were recorded after 1 h and it is shown in Fig. 3(a–c). As can be seen, the addition of sodium borohydride shifts the longitudinal plasmon bands towards a lower wavelength. This could be due to a change in the refractive index at the nanoparticle surface appearing due to the replacement of CTAB by hydride ions [25]. The $NaBH_4$ modified NBPs were treated with 11-MUA followed by the investigation of absorption spectra. The addition of 11-MUA shifts the longitudinal bands towards a higher wavelength.

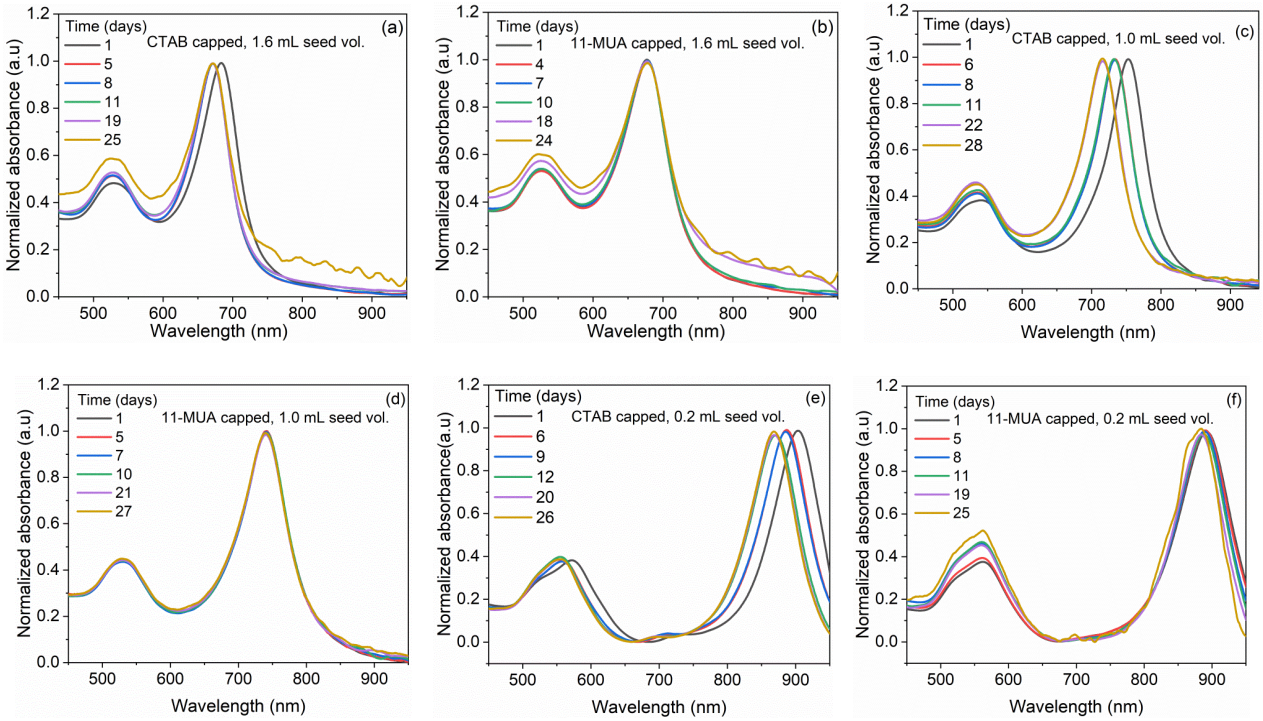


Fig. 4 LSPR band maxima of NBPs recorded on different days: CTAB capped NBPs synthesized using (a) 1.6, (c) 1, and (e) 0.2 mL of seed volume, and 11-MUA capped NBPs synthesized using (b) 1.6, (d) 1, and (f) 0.2 mL of seed volume.

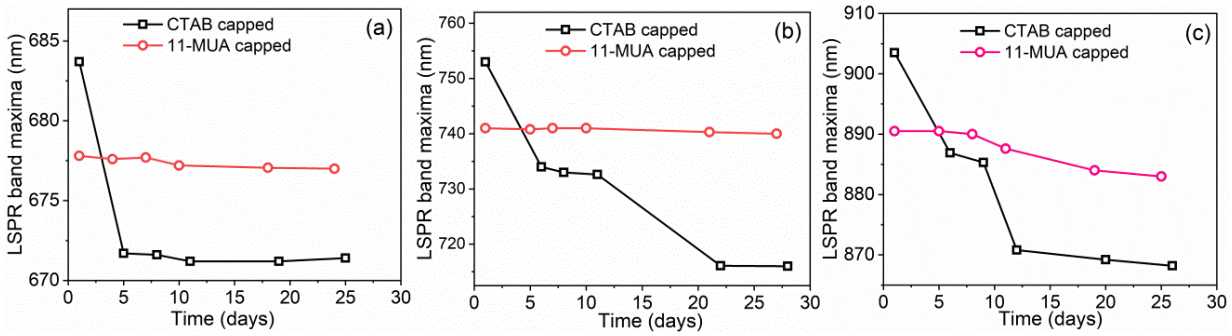


Fig. 5 Stability of CTAB capped, and 11-MUA capped Au NBPs with time synthesized using (a) 1.6 mL, (b) 1.0 mL, and (c) 0.2 mL of seed solution.

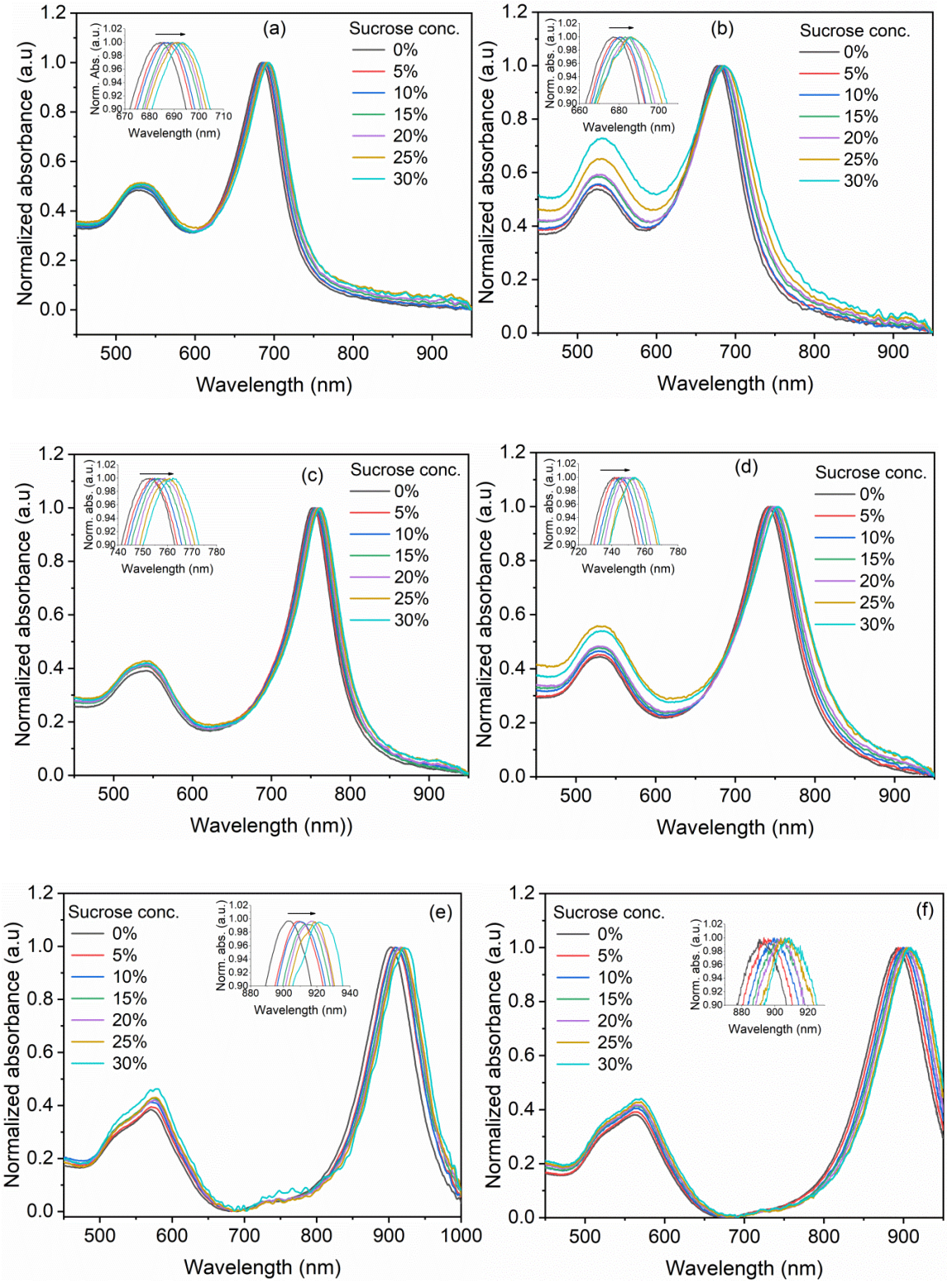


Fig. 6 LSPR absorption spectra of NBPs at different refractive indices of the medium (a), (c), and (e): CTAB capped NBPs synthesized using (a) 1.6, (c) 1.0, and (e) 0.2 mL seed volume; 11-MUA capped NBPs synthesized using (b) 1.6, (d) 1.0, and (f) 0.2 mL seed volume.

After overnight incubation, the NBPs solution was centrifuged to remove excess 11-MUA, and the absorption spectra were recorded. The redshifts in the longitudinal peaks were observed even after centrifuging, indicating the binding of 11-MUA molecules to the NBP surface. The longitudinal band maximum of as-prepared Au NBP in Fig. 3(a) is at 681 nm, which moved to 666 and 677 nm after $NaBH_4$

treatment and 11-MUA capping, respectively. The corresponding band positions in Fig. 3(b) are 752, 727, and 741 nm, and in Fig. 3(c), are 897, 882, and 892 nm.

The stability of both CTAB-capped and MUA-capped Au NBPs was also investigated. Fig. 4(a–f) shows the absorption spectra of NBPs recorded for more than three weeks, whereas Fig. 5(a–c) shows the variation in the longitudinal band maxima with time. As shown in Fig. 5(a–c), a gradual decrease in the LSPR peak position of CTAB-capped NBPs was observed with time which could be due to the decrease in the longitudinal size of bipyramids. However, in the case of 11-MUA-capped high aspect ratio NBPs, the observed trend is nearly linear. This indicated that the NBPs are highly stable in the presence of 11-MUA.

4.3 Refractive Index Sensitivity of NBPs

The refractive index sensitivity of synthesized Au NBP were investigated with sucrose solutions of varying weight/volume percentages (5–30%). Sucrose is selected as it is a highly water-soluble small molecule that provides the possibility of refractive index modulation of the solution in a controlled manner Fig. 6(a–f) shows the absorption spectra of Au NBPs with the variation of the sucrose concentration. Fig. 6(a, c, e) corresponds to Au NBP capped with CTAB, whereas Fig. 6(b, d, f) corresponds to the NBPs capped with 11-MUA. The inset in Fig. 6(a–f) shows the expanded region of longitudinal plasmon resonance band maxima. It is evident in all the LSPR spectra that the longitudinal plasmon band shifts towards red with an increase in the concentrations of sucrose. This indicates the sensitivity of the Au NBPs toward the refractive index of the surrounding medium.

Fig. 7(a–f) shows the variation of the longitudinal plasmon resonance band maxima with the change in the solution's refractive index. The refractive index values of sucrose were obtained from previously published works [33–35]. The experiment was repeated thrice for each concentration and for all three NBPs to ensure reproducibility and obtain the standard deviation. The experimental data points correspond to the average values of the band maxima position of three trials. The experimental data were fitted linearly to obtain the sensitivity of corresponding Au NBP. It was observed that the RI sensitivity of Au NBPs increases with their length and aspect ratio. Also, the 11-MUA capped NBPs show better sensitivity compared to the CTAB capped Au NBPs, which could be due to the variation in adsorbed layer length on the BPs surface because of the replacement of the CTAB bilayer by a single monolayer of MUA. The figure of merit (FOM) was also calculated using FOM = RIS/FWHM [17], which increases with an increase in the length and aspect ratio of the NBPs. Since the refractive index sensitivity depends on various factors like the refractive index of the medium, the length of adsorbed layer on the nanoparticle surface and the decay length, any change in one of these parameters would change the overall sensitivity of nanoparticles [36].

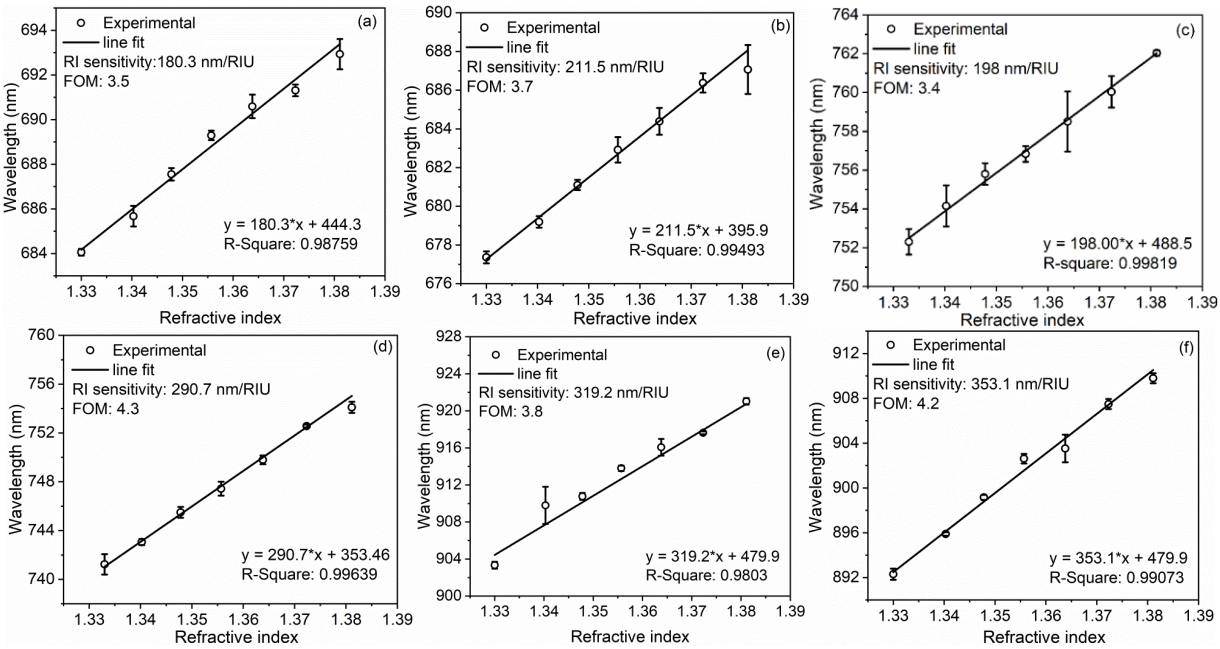


Fig. 7 Variation of longitudinal plasmon band maxima against the refractive index of the medium: CTAB capped NBPs synthesized using (a) 1.6, (b) 1.0, and (c) 0.2 mL seed volume; 11-MUA capped NBPs synthesized using (b) 1.6, (d) 1.0, and (f) 0.2 mL seed volume.

The obtained RI sensitivity of Au NBPs was compared with the RI sensitivity of Au nanospheres and Au nanorods. Table 1 lists the RI sensitivity of these nanostructures obtained in our earlier work as well as reported in other works. It is evident from the table that with comparable sizes, Au NBPs shows better RI sensitivity, which makes them more suitable for the RI sensitivity applications.

Table 1 Comparison of refractive index sensitivity of Au nanosphere, Au nanorods and Au NBPs.

Nanostructures	Size	RI sensitivity	Ref.
Au nanospheres	100 nm	180 nm/RIU	[37]
Au nanorods	2.7 AR	317 ± 8 nm/RIU	[23]
Au nanorods	2.7 AR	196 nm/RIU	[38]
Au nanobipyramids	3.0 AR	353 nm/RIU	This work

5 Conclusions

Gold nanobipyramids of different aspect ratios were synthesized using a seed-mediated growth method where the sizes of nanobipyramids were tuned using different seed solution volumes. The CTAB in CTAB capped Au NBPs was replaced by 11-MUA, which increased the stability of NBPs dramatically. The RI sensitivity of CTAB and 11-MUA capped Au NBPs were studied with different sucrose concentrations in water. It was found that the 11-MUA functionalized NBPs have better RI sensitivity and figure of merit (FOM) compared to the CTAB capped Au NBPs. Further, the RI sensitivity increases with an increase in the aspect ratio of Au NBPs. Refractive index sensitivity of 353 nm/RIU was obtained for NBPs synthesized using 0.2 mL of seed solution with an aspect ratio of 3.

Disclosure

The authors declare no conflict of interest.

Acknowledgments

Financial support from the Department of Science and Technology (DST) India under the project grant number IDP/BDTD/11/2019 is gratefully acknowledged. Prajna N D acknowledges the TMA Pai Ph. D. fellowship from the Manipal Academy of Higher Education (MAHE).

References

1. K. M. Mayer, J. H. Hafner, "Localized surface plasmon resonance sensors," Chemical Reviews 111(6), 3828–3857 (2011).
2. K. A. Willets, R. P. Van Duyne, "Localized surface plasmon resonance spectroscopy and sensing," Annual Review of Physical Chemistry 58, 267–297 (2007).
3. M. Chauhan, V. K. Singh, "Review on recent experimental SPR/LSPR based fiber optic analyte sensors," Optical Fiber Technology 64, 102580 (2021).
4. E. Petryayeva, U. J. Krull, "Localized surface plasmon resonance: Nanostructures, bioassays and biosensing - A review," Analytica Chimica Acta 706(1), 8–24 (2011).
5. H. Chen, L. Shao, K.C. Woo, T. Ming, H.Q. Lin, and J. Wang, "Shape-dependent refractive index sensitivities of gold nanocrystals with the same plasmon resonance wavelength," The Journal of Physical Chemistry C 113(41), 17691–17697 (2009).
6. J. Wang, H. S. Zhou, "Aptamer-based Au nanoparticles-enhanced surface plasmon resonance detection of small molecules," Analytical Chemistry 80(18), 7174–7178 (2008).
7. K. L. Kelly, E. Coronado, L. L. Zhao, and G. C. Schatz, "The optical properties of metal nanoparticles: the influence of size, shape, and dielectric environment," The Journal of Physical Chemistry B 107(3), 668–677 (2003).
8. S. Jung, K. L. Shuford, and S. Park, "Optical property of a colloidal solution of platinum and palladium nanorods: localized surface plasmon resonance," The Journal of Physical Chemistry C 115(39), 19049–19053 (2011).
9. P. Zheng, H. Tang, B. Liu, S. Kasani, L. Hung, and N. Wu, "Origin of strong and narrow localized surface plasmon resonance of copper nanocubes," Nano Research 12, 63–68 (2019).
10. J. Cao, T. Sun, and K. T. V. Grattan, "Gold nanorod-based localized surface plasmon resonance biosensors: A review," Sensors and Actuators B: Chemical 195, 332–351 (2014).
11. H. R. Hegde, S. Chidangil, and R. K. Sinha, "Review of synthesis and sensing applications of anisotropic silver and gold nanostructures," Journal of Vacuum Science & Technology B, Nanotechnology and Microelectronics: Materials, Processing, Measurement, and Phenomena 39(5), 050801 (2021).
12. T. H. Chow, N. Li, X. Bai, X. Zhuo, Lei Shao, and J. Wang, "Gold nanobipyramids: An emerging and versatile type of plasmonic nanoparticles," Accounts of Chemical Research 52(8), 2136–2146 (2019).

13. A. Campu, F. Lerouge, D. Chateau, F. Chaput, P. Baldeck, S. Parola, D. Maniu, A. M. Craciun, A.Vulpoi, S. Astilean, and M. Focsan, "Gold nanobipyramids performing as highly sensitive dual-modal optical immunosensors," Analytical Chemistry 90(14), 8567–8575 (2018).
14. N. R. Jana, L. Gearheart, and C. J. Murphy, "Seed-mediated growth approach for shape-controlled synthesis of spheroidal and rod-like gold nanoparticles using a surfactant template," Advanced Materials 13(18), 1389–1393 (2001).
15. M. Liu, P. Guyot-Sionnest, "Mechanism of silver (I)-assisted growth of gold nanorods and bipyramids," The Journal of Physical Chemistry B 109(47), 22192–22200 (2005).
16. X. Zhang, M. Tsuji, S. Lim, N. Mieyamae, M. Nishio, S. Hikino, and M. Umezu, "Synthesis and growth mechanism of pentagonal bipyramid-shaped gold-rich Au/Ag alloy nanoparticles," Langmuir 23(11) 6372–6376 (2007).
17. H. Chen, X. Kou, Z. Yang, W. Ni, and J. Wang, "Shape-and size-dependent refractive index sensitivity of gold nanoparticles," Langmuir 24(10), 5233–5237(2008).
18. Y. Xu, X. Wang, L. Cheng, Z. Liu, and Q. Zhang, "High-yield synthesis of gold bipyramids for in vivo CT imaging and photothermal cancer therapy with enhanced thermal stability," Chemical Engineering Journal 378, 122025 (2019).
19. H. R. Hegde, S. Chidangil, and R. K. Sinha, "Refractive index sensitivity of triangular Ag nanoplates in solution and on glass substrate," Sensors and Actuators A: Physical 305, 111948 (2020).
20. H. Hegde, C. Santhosh, and R. K. Sinha, "Seed mediated synthesis of highly stable CTAB capped triangular silver nanoplates for LSPR sensing," Materials Research Express 6(10), 105075 (2019).
21. H. R. Hegde, S. Chidangil, and R. K. Sinha, "Refractive index and formaldehyde sensing with silver nanocubes," RSC advances 11(14), 8042–8050(2021).
22. R. K. Sinha, "Surface-enhanced Raman Scattering and Localized Surface Plasmon Resonance Detection of Aldehydes Using 4-ATP Functionalized Ag Nanorods," Plasmonics 18, 241–253 (2022).
23. H. R. Hegde, S. Chidangil, and R. K. Sinha, "Refractive index sensitivity of Au nanostructures in solution and on the substrate," Journal of Materials Science: Materials in Electronics 33(7), 4011–4024 (2022).
24. D. Chateau, A. Desert, F. Lerouge, G. Landaburu, S. Santucci, and S. Parola, "Beyond the Concentration Limitation in the Synthesis of Nanobipyramids and Other Pentatwinned Gold Nanostructures," ACS Applied Materials & Interfaces 11(42), 39068–39076 (2019).
25. J. He, S. Unser, I. Bruzas, R. Cary, Z. Shi, R. Mehra, K. Aron, and L. Sagle, "The facile removal of CTAB from the surface of gold nanorods," Colloids and Surfaces B: Biointerfaces 163, 140–145 (2018).
26. C. A. Schneider, W. S. Rasband, and K. W. Eliceiri, "NIH Image to ImageJ: 25 years of image analysis," Nature Methods 9(7), 671–675 (2012).
27. S. Xu, W. Ouyang, P. Xie, Y. Lin, B. Qiu, Z. Lin, G. Chen, and L. Guo, "Highly Uniform Gold Nanobipyramids for Ultrasensitive Colorimetric Detection of Influenza Virus," Analytical Chemistry 89(3), 1617–1623 (2017).
28. D. Chateau, A. Liotta, F. Vadcard, J. R. G. Navarro, F. Chaput, J. Lermé, F. Lerouge, and S. Parola, "From gold nanobipyramids to nanojavelins for a precise tuning of the plasmon resonance to the infrared wavelengths: experimental and theoretical aspects," Nanoscale 7(5), 1934–1943 (2015).
29. C. Fang, G. Zhao, Y. Xiao, J. Zhao, Z. Zhang, and B. Geng, "Facile Growth of High-Yield Gold Nanobipyramids Induced by Chloroplatinic Acid for High Refractive Index Sensing Properties," Scientific Reports 6(1), 36706 (2016).
30. G. Weng, X. Shen, J. Li, J. Zhu, J. Yang, and J. Zhao, "Multipole plasmon resonance in gold nanobipyramid: Effects of tip shape and size," Physics Letters A 412, 127577 (2021).
31. J. Cao, E. K. Galbraith, T. Sun, and K. T. V. Grattan, "Effective surface modification of gold nanorods for localized surface plasmon resonance-based biosensors," Sensors and Actuators B: Chemical 169, 360–367 (2012).
32. J. Homola, "Present and future of surface plasmon resonance biosensors," Analytical and Bioanalytical Chemistry 377(3), 528–539 (2003).
33. OIML, "Automated Refractometers: Methods and Means of Verification," (2006).
34. D. F. Charles, "Refractive Indices of Sucrose-Water Solutions in the Range from 24 to 53% Sucrose," Analytical Chemistry 37(3), 405–406 (1965).
35. C. F. Snyder, A. T. Hattenburg, "Refractive indices and densities of aqueous solutions of invert sugar," National Bureau of Standards, Washington D. C. (1963).
36. L. Tian, E. Chen, N. Gandra, A. Abbas, and S. Singamaneni, "Gold Nanorods as Plasmonic Nanotransducers: Distance-Dependent Refractive Index Sensitivity," Langmuir 28(50), 17435–17442 (2012).
37. E. Martinsson, B. Sepulveda, P. Chen, A. Elfwing, B. Liedberg, and D. Aili, "Optimizing the refractive index sensitivity of plasmonically coupled gold nanoparticles," Plasmonics 9, 773–780 (2014).
38. L. P. F. Peixoto, J. F. L. Santos, and G. F. S Andrade, "Plasmonic nanobiosensor based on Au nanorods with improved sensitivity: A comparative study for two different configurations," Analytica Chimica Acta 1084, 71–77 (2019).

The Effect of Photobiostimulation by Light Waves in the Blue Range of the Spectrum on Microcirculation Parameters and the Activity of Oxidative Homeostasis Enzymes in the Skin

Vadim V. Astashov[1*], Valentin I. Kozlov[1,2], Vladimir A. Duvanskiy[1,2], Pavel V. Novokreshchenov[1], and Ilya M. Pushkar[1]

[1] Peoples' Friendship University of Russia, 8 Miklukho-Maklaya str., Moscow 117198, Russia

[2] Scientific and Practical Center for Laser Medicine named after O. K. Skobelkin, 40 Studencheskaya str., Moscow 121165, Russia

***e-mail:** vastashov3@gmail.com

Abstract. The study employs laser doppler flowmetry and laser fluorescence spectroscopy to reveal the changes in microcirculation and activity of coenzymes of oxidative metabolism in the finger skin under the influence of photobiostimulation by monochrome incoherent low-intensity electromagnetic radiation with a wavelength of 470 nm. Photobiostimulation with light waves in the blue range has contributed to an increase in hemomicrocirculation during and 15 min after the termination of exposure, while the indicator lymph outflow, on the contrary, decreased during the irradiation period and recovered after its termination. The dynamics of changes within the parameters of blood microcirculation, the lymph flow in microvessels and the indicators of oxidative metabolism showed that the skin microcirculation system is an important acceptor of the photobiostimulating effect of light in the blue range of the spectrum. Photobiostimulation triggers the mechanism of activation of hemomicrocirculation by reducing myogenic vasomotion, thereby increasing the conductivity of cardiogenic biorhythm in the vessels of the microcirculatory bed. With an increase in the level of hemomicrocirculation, photobiostimulation is directly associated with the activation of tissue oxidative metabolism. © 2023 Journal of Biomedical Photonics & Engineering.

Keywords: laser doppler flowmetry; lymph outflow; blood microcirculation; myogenic vasomotion; oxidative metabolism; photobiostimulation with light waves in the blue range of the spectrum.

Paper #3531 received 15 Sept 2022; revised manuscript received 15 Dec 2022; accepted for publication 15 Dec 2022; published online 30 Mar 2023. doi: 10.18287/JBPE23.09.010309.

1 Introduction

One of the priority work areas of the Biomedical Optics technical group of the International Optical Association (OPTICA) is to study the mechanisms by which non-ionizing optical radiation in the visible and near infrared spectral range is absorbed by endogenous chromophores, causing photophysical and photochemical phenomena at various biological scales [1]. Making the basis of light therapy, photobiostimulation (PBS) involves the use of various light sources, including LEDs and broadband light in the visible and infrared spectrum resulting in physiological changes and therapeutic effects.

Human body has photoreceptors tuned to different light frequencies and associated with various cellular reactions. Human skin is the main target of various light waves. Visible radiation of light waves (400–750 nm) penetrates the dermis deeply enough, with a multiple

decrease in intensity every ~1 mm [2]. Part of the blue visible radiation spectrum is reflected from blood vessels and red blood cells moving in them back through the skin, so that the total radiation flux near the skin surface is greater than the incident light [2], which allows it to affect a much larger number of cells compared to the UV range of visible radiation.

For this reason, in recent years, light emission of blue diapason is actively used in dermatology. In particular, a number of studies [3] have shown that blue light has a positive effect on fibroblasts and can be used to treat keloids and fibrosis.

An experimental study focused on burn modeling [4] reports that under the influence of the blue light emitted by the light-emitting-diodes, laboratory rats consumed more food than the rats from the control group, the angiogenesis index increased after 7 days of treatment and the skin of irradiated animals began to reactivate [4].

Research that was performed on melanocyte cell cultures [5] showed that exposure to blue light significantly improved viability, proliferation and migration of melanocytes. Blue light also proved to be able to activate opsins that play an important role in healing skin wounds and restoring human epidermal barrier function [6].

For blue light (400–470 nm), the penetration depth into the tissues is 2 mm, however, taking into account the radiation scattered in the tissues, its penetration depth can reach as far as 2.5 cm. Moreover, since blue light can propagate in an aqueous medium without absorption, it is maximally absorbed by lymph, bile, tendons, and adipose tissue [7, 8].

Nowadays a number of chemical structures are considered to be acceptors of light emission in the blue portion of the spectrum, among which a large group of flavins (such as NAD-H dehydrogenases, succinate dehydrogenases, acyl-CoA dehydrogenases, D-amino acid oxidases, glucose oxidases and the cytochrome system) is considered the final photon acceptor for flavin dehydrogenases. The compounds having porphyrin structures (bilirubin, haemoglobin, protoporphyrin, and porphyrin) are good at absorbing the blue light. Light emission with the wavelength of 420–475 nm is absorbed by a large group of carotenoids (carotene, neurosporine, and carotenoids of cardiac homogenates) that are considered antioxidants [9].

For the in-depth study of PBS, the task is to identify the physiological effects of phototherapy and the mechanisms of involving the microcirculation system, which is directly concerned with ensuring the oxidative metabolism in tissues.

Laser doppler flowmetry (LDF) is widely used among various other methods of both direct and indirect recording microcirculation, including the lymphatic link [10]. The signal recorded during LDF characterizes the blood flow in the microvessels with the tissue volume of about 1 mm^3 [10], while in the lymphatic capillaries and microvessels, the LFD signal characterizes the mobility of lymph and lymphocytes [11].

It is well-known that the metabolic processes in the skin and other tissues are energy-dependent, which makes it possible to use the method of laser fluorescence spectroscopy (LFS) to assess oxidative metabolism. For this purpose, we propose to identify the fluorescence amplitude of the coenzymes nicotinamide adenine dinucleotide (NADH) and the flavinadenine dinucleotide (FAD) [12–14].

The aim of this study is to identify the changes in microcirculation and the activity of coenzymes of oxidative metabolism in the skin of fingers under the influence of photobiostimulation by monochrome incoherent low-intensity electromagnetic radiation with a wavelength of 470 nm.

2 Methods and Materials

The experimental study involved 40 men aged 19 to 28 (the average age is 20.5), conditionally healthy students of the *Medical Institute* of the *Peoples' Friendship University of Russia*, who voluntarily agreed to participate in the study and provided their Informed Consent. Their participation was also approved by the University's Ethics Committee.

The participants underwent transdermal photobiostimulation with electromagnetic radiation of the light range with the wavelength of $\lambda = 470$ nm (the blue spectrum) for 8 min using an autonomous light-emitting bracelet BASI (SPE "Poisk" Ltd, Russia) worn on the wrist region with the radiating matrix on the inner surface of the wrist in contact with skin. the illumination of light-emitting diode was 2000 lx, the power of the emitted blue light by the emitting matrix was 40 mW, the density of radiation on the skin was 4–5 mW/cm^2 (the skin area irradiated with laser diodes was 8 cm^2), the energy of the emitted light during 8 min was 20 J. When considering the time of transdermal (transcutaneous) exposure to blue light, we proceeded from the generally accepted recommendations and conditionally divided the area of influence of the light-emitting-diode matrix into four zones with the tentative exposure time for one zone being 2–5 min [15].

Synchronous registration of blood microcirculation and lymphocirculation indicators was performed using a multi-channel LDF probe, while the activities of redox coenzymes NADH and FAD were recorded by LFS using the Lazma ST device (SPE "LAZMA" Ltd, Russia).

The instrument probe was fixed on the palmar surface of the distal phalanx of the third finger of the left hand to register all the parameters when LDF and LPS were recorded. This was done in the following sequence: 1) before photobiostimulation for 4 min;

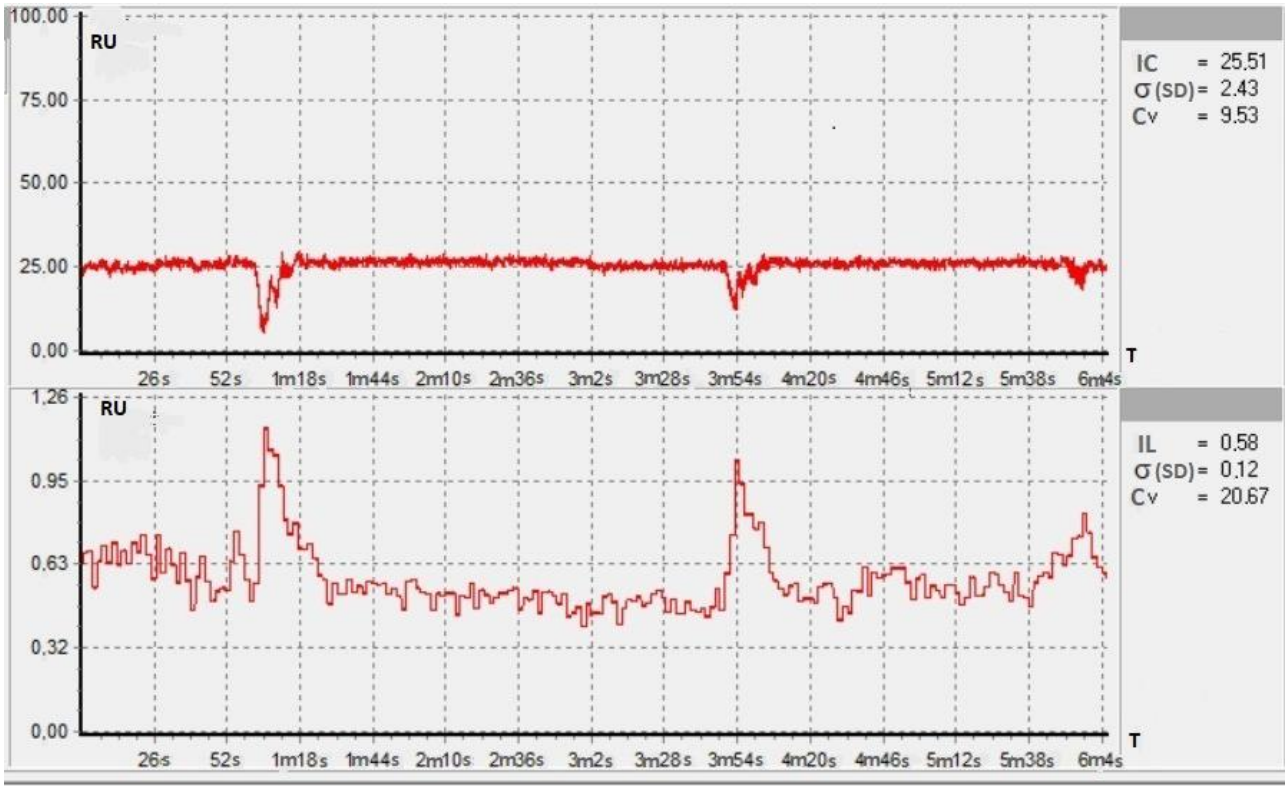
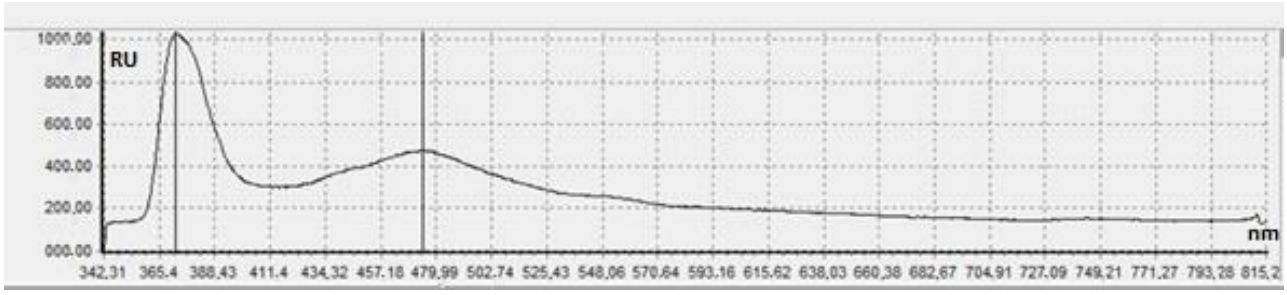
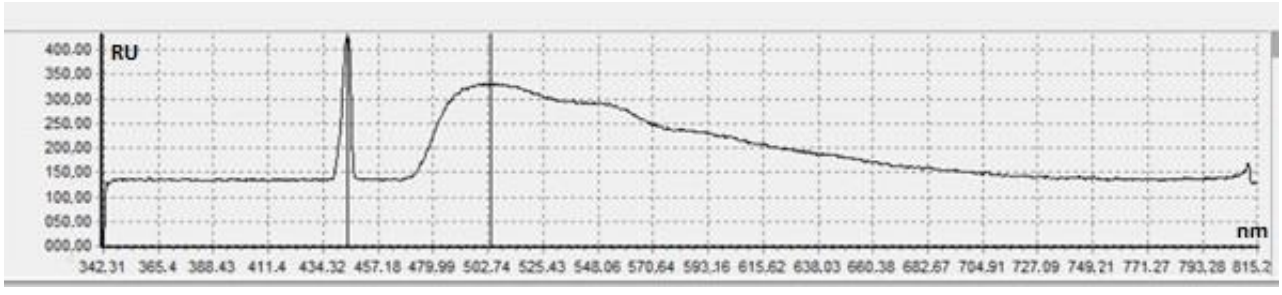


Fig. 1 An example of simultaneously detected diagnostic parameters: synchronous recording of the hemomicrocirculation and lymph flow; the changes are visible during involuntary breath retention (OX axis – recording time, (T); OY axis – relative units, (RU).



(a)



(b)

Fig. 2 An example of simultaneously detected diagnostic parameters: registration using LFS: (a) NADH, (b) FAD (OX axis – wavelength, nm; OY axis – in relative units, RU).

2) during photobiostimulation for 8 min; 3) 15 min after stopping photobiostimulation for 4 min. LDF and LFS were recorded when the test subjects were in the sitting position.

The indicator of blood microcirculation (IC) was determined by the LDF method (in the previous works on LDF, it was designated as PM). It is believed [16], that IC is determined by two factors: the concentration of red

blood cells in the probed tissue volume and their mobility (an averaged erythrocyte rate). IL is proportional to the product of the number of scatterers in the lymph flow by the average speed of their movement [11].

The LDF-gram analysis was used to assess the IC and IL indicators; the level of the flow fluctuation was evaluated by means of SD (standard deviation) or fluxes recorded in relative (perfusion) units (RU); whereas their coefficient of variation (Cv) was evaluated in % (Fig. 1).

The frequency-amplitude analysis of LDF-grams [10, 16–18] defined the contribution of the vasomotion-induced physiologically most significant blood flow fluctuations within the range of 0.1 Hz and its immediate vicinity (0.07–0.15 Hz). The vasomotor biogenic rhythm is secondarily influenced by modulations of neurogenic, respiratory and cardiogenic nature that were determined by their amplitude in the corresponding frequency ranges (A_{NF} neurogenic, A_{MF} myogenic, A_{HF} respiratory, and A_{CF} cardiogenic). The contribution of various biorhythms to the modulation of tissue blood flow was estimated by their power R_i as a percentage of the total power of the spectrum of M fluxmotions:

$$R_i = A_i^2 / M \times 100\%, \quad (1)$$

where $M = A_{NF}^2 + A_{MF}^2 + A_{HF}^2 + A_{CF}^2$.

To assess the oxidative metabolism, the amplitudes of fluorescence of NADH and FAD coenzymes (relative units, RU) were determined by the LFS method, while their ratio was determined by the redox ratio (NADH/FAD) [12, 13, 19] (Fig. 2). The fluorescence of the NADH and FAD coenzymes was excited using a Nichia NVSU233B D4 LED with a wavelength of 365 nm (NADH fluorescence wavelength is in the range of 460–470 nm) and an OSRAM PLT5 450B laser diode with a wavelength of 450 nm (FAD fluorescence maximum is in the range of 510–520 nm) [13]. The relationship between the state of microcirculation and oxidative metabolism in tissue was quantified by the indicator of oxidative metabolism (IOM) equal to IC/NADH+FAD [12].

The obtained data were processed using the methods of variation statistics, the reliability of differences was determined using the Student's criterion; the results were considered reliable at $p < 0.05$.

3 Results and Discussion

The calculated parameters of IC and IL, Cv and SD give an overall assessment of the state of hemomicrocirculation and lymph flow (Table 1). The results of the study indicate that during the time of exposure to light radiation, PBS increases the hemomicrocirculation indicators by an average of 26% compared to the baseline level. 15 min after the cessation of light exposure, the hemomicrocirculation indicators still exceed the baseline level by 22%.

IC (the indicator of hemomicrocirculation) has a complex nature, because it depends on the mobility of red blood cells, their concentration in microvessels and, to a certain extent, on the geometry of blood flow in tissues. Biomicroscopic studies of capillaries and other microvessels in human skin show that the bulk of erythrocytes is concentrated in postcapillary venules [10]. Because of this, approximately 50% of the value of the recorded LDF signal is due to the mobility of erythrocytes in the postcapillary segment of the microcirculatory bed. With ABS, the increase in IC is more likely to be due to increased level of the tissue blood flow. This is what light therapy using the blue range of the spectrum is designed for [7]. At the same time, it is possible that with the acceleration of the transition of erythrocytes from capillaries to microvessels of the postcapillary link, their local hematocrit increases.

The IC is subject to significant temporal and topological variations, which is clearly seen by the dynamics of the flux and SD. The results of the study of hemomicrocirculation show that during PBS these indicators decrease, and in the aftereffect period they are restored to their original values. The data obtained may indicate a decrease in the level of modulation of tissue blood flow during irradiation.

A very weak signal has been recorded from the lymphatic segment of the microcirculatory system, which is due to the low population of lymphatic capillaries and postcapillaries with stetho-reflective elements among which the lymphocytes are the most significant. Synchronous recording of IC and IL clearly shows that blood flow and lymph outflow at the level of the microcirculation system are closely functionally interconnected and are in antiphase.

Table 1 Indicators of hemomicrocirculation.

Parameters	Original value	Photobiostimulation	
		During	After
IC, RU	23.4 ± 2.94	29.4 ± 1.46*	28.1 ± 1.62*
SD, RU	4.01 ± 0.69	2.94 ± 0.40*	3.77 ± 0.62
Cv, %	17 ± 2.3	10 ± 1.4*	13 ± 2.8

* the differences are significant in comparison with the control data at $p < 0.01$.

Table 2 Lymph outflow indicators.

Parameters	Original value	Photobiostimulation	
		During	After
IL, RU	0.7 ± 0.12	0.5 ± 0.05	0.6 ± 0.09
SD, RU	0.14 ± 0.02	0.14 ± 0.01	0.16 ± 0.02*
Cv, %	20 ± 3.3	28 ± 3.8*	27 ± 5.3*

* the differences are significant in comparison with the control data at $p < 0.01$.

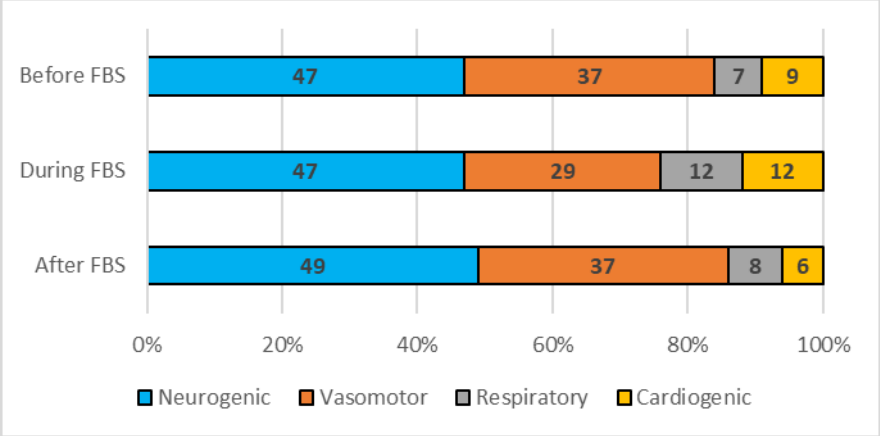


Fig. 3 The ratio of the main rhythmic components of fluxmotions in the LDF-gram by their contribution (in %) to the power of the spectrum and their changes due to PBS.

In PBS, the lymph outflow index, on the contrary, decreased by 19% compared to the baseline level, and although after the PBS it showed some increase, the IL was below the baseline level by 13% (Table 2). It should be noted that the variation of the IL was significantly different from the flux in the blood microvessels. It turned out that as the IL decreases with PBS, the temporal variability of the lymph flow increases markedly. This may be due to the activation of contractility of smooth myocytes in the initial links of lymphatic vessels that starts immediately after lymphatic postcapillaries.

The frequency-amplitude analysis of the LDF-gram is applicable to the assessment of the myogenic mechanism of modulation of tissue blood flow, because it most dynamically reflects the changes in hemomicrocirculation due PBS (Fig. 3). Among the local (within the area of optical sensing) microvascular biorhythms, the dominant rhythm is the myogenic one that accounts for 37% of the total power of the oscillation spectrum of tissue blood flow at the initial (before irradiation) level. Myogenic biorhythm lies in the frequency range of 0.1 Hz and its immediate vicinity. However, it is subject to secondary neurogenic influences that originate outside the microcirculation system but nevertheless have modulating effects on hemomicrocirculation.

During PBS, the activity of the myogenic mechanism somewhat decreases (up to 29% of the total power of the spectrum), which results in the increased conductivity of cardiogenic modulations through the capillary link of the microcirculatory bed. This is due to both an increase in the mobility of red blood cells and an increase in hematocrit in the postcapillary link of the microcirculatory bed. After the PBS is over (in 15 min), the myogenic vasomotion returns to the initial level. As the activity of the myogenic mechanism decreases, the efficiency of fluxmotion decreases by 27% (see Table 1).

Another important consequence of PBS is decreased vascular tone (VT) in the vessels of the microcirculatory bed. Vascular tone can be characterized by means of normalization of the recorded level of fluxmotion by the amplitude of myogenic biorhythm: $VT = COE/A_{MF}$ [10]. In some works [10], normalization according to the microcirculation index (IC) is applied. IC, as noted above, by its nature may have an ambiguous interpretation, since its increase may indicate both an increase in microcirculation due to increased mobility of red blood cells, and its deterioration in cases of increased hematocrit in the vessels of the postcapillary link. Therefore, normalization of the frequency-amplitude parameters of the LDF-gram by IC inevitably leads to an ambiguous interpretation of the LDF results. Our study has revealed that PBS leads to a decreased vascular tone in microvessels within 7% (from 2.9 to 2.7 conl. units), which basically has a decrease in the activity of myogenic vasomotion.

Table 3 Indicators of oxidative metabolism during photobiostimulation.

Indicators	Original value	Photobiostimulation	
		During	After
Amplitude NADH, RU	0.51 ± 0.01	0.48 ± 0.01	0.48 ± 0.01
Amplitude FAD, RU	0.78 ± 0.01	0.74 ± 0.01*	0.73 ± 0.01*
Redox ratio NADH/ FAD, RU	0.6 ± 0.01	0.65 ± 0.01	0.66 ± 0.01
Indicator of oxidative metabolism IC /(NADH+FAD), RU	8.35 ± 0.02	14.02 ± 0.03*	13.01 ± 0.04*

* the differences are significant in comparison with the control data at $p < 0.01$.

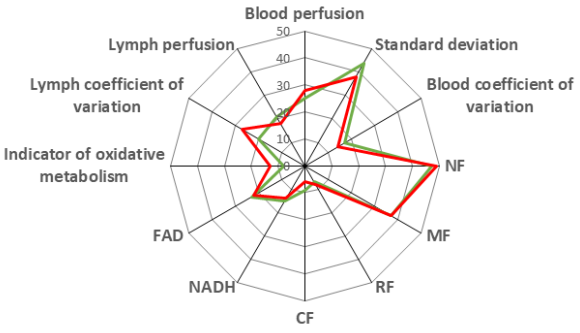


Fig. 4 Synchronous changes in skin microcirculation and oxidative metabolism during photobiostimulation, RU. (Cardiogenic Fluctuations (CF); Respiratory Fluctuations (RF); Myogenic Fluctuations (MF); Neurogenic Fluctuations (NF)).

The structure of temporary fluctuations of lymph flow in microvessels during PBS demonstrates an increased amplitude of myogenic oscillations compared to the baseline level. It is also noted here that the reaction of lymphatic microvessels to PBS is in antiphase with the reaction of blood vessels of the microcirculatory bed. The contour of the functional interaction of blood and lymphatic microvessels in the microcirculation system remains largely unclear. The data on the lymph flow rate relate mainly to the relatively large lymphatic vessels and are principally determined by the reduction of lymphangions. Spontaneous active contractions of lymphangions usually occur with a frequency of 2–3 to 10–18 vibrations/min. In humans, with local anesthesia, the lymphatic vessels of the foot contracted with a frequency of 4–5 in 1 min [20, 21]. The pressure drops that occur during the reduction of lymphangions have a sucking effect on the lymph flow in the lymphatic postcapillaries and capillaries.This means that the mechanisms activating the lymph flow lie outside the microcirculation system and, unfortunately, the possibility of their direct analysis by the LDF method must be considered limited.

Thus, photobiostimulation with light in the blue range of the spectrum activates the processes of microcirculation in its circulatory link. The indicators of lymph flow decrease, which may indicate a redistribution of interstitial fluid in the tissue microdistrict and activation of venous tissue drainage. Our data correspond with the data of other authors [22] examining the skin of mice after being irradiated with a low dose of blue light (< 300 mJ/cm^2), which indicates that irradiation with blue light triggers the synthesis of hydrogen peroxide in T-lymphocytes and enhances their mobility in the skin. These data give reason to believe that T-lymphocytes have photosensitivity in this range of the spectrum. The data we obtained on PBS are also confirmed by the data of a clinical study in which patients with peripheral nerve damage and the presence of neuropathic pain syndrome were exposed to monochrome incoherent low-intensity light radiation of the blue spectrum (470 nm) [23]. Their study showed a pronounced analgesic and decongestant effect as a result of the exposure, which may indicate a change in microcirculation and lymphatic drainage of tissues. Our observations are also consistent with the results of the study [24], which showed that when exposed to incoherent light radiation of red (633 nm, 70 mW/cm^2) and near infrared (830 nm, 55 mW/cm^2) range on the wrist skin for 5 min, arterioles dilated, leading to increased tissue perfusion in healthy people.

The components of the energy metabolism of the cell, which include glycolysis and oxidative phosphorylation, are associated with the processes of cellular respiration and ATP synthesis. The NADH and FAD cofactors act as electron donors and acceptors in ATP formation reactions that are present in the cell in oxidized (NAD^+, FAD) or reduced forms (NADH, $FADH_2$) [25]. Summary data on the dynamics of fluorescence of the NAD and FAD coenzymes, determined by means of LFS, are presented in Table 3.

The obtained results have shown that photobiostimulation causes a decrease in the amplitude of fluorescence of the oxidative NADH and FAD coenzymes, while the amplitude of FAD is significantly reduced to a greater extent. The change in the amplitude of fluorescence of the NADH coenzyme, and hence its concentration, is due to a change in oxidative metabolism in tissues. Our data have shown that an increase in the level of microcirculation triggers a mechanism for increasing the level of oxidative metabolism in tissues (Fig. 4).

Since all indicators are presented in units, for their comparability, a proportionality multiplier is introduced when constructing a diagram for extremely low indicators: ×10 for SD, ×30 for IL, NADH, and FAD.

As reported by Luo et al. [19], decreased amplitude of NADH fluorescence activates the oxidative

metabolism. If NADH is localized mainly in the mitochondria and participates mainly in the energy metabolism of the cell, then FAD is contained both in the cytoplasm and in the mitochondria and is involved in addition to oxidative phosphorylation in various biochemical processes such as glutathione utilization, lipogenesis, lipid peroxidation, synthesis of acetyl coenzyme A, the pentose phosphate cycle, etc., which significantly complicates data analysis [25]. The ratio of the oxidized electron carriers to the reduced ones is characterized by a redox ratio [26]. In our study, the redox ratio in PBS practically does not change, which may indicate the preservation of the processes of glycolysis and oxidative phosphorylation.

4 Conclusion

Synchronous recording of the dynamics of blood microcirculation, lymph flow in microvessels and indicators of oxidative metabolism showed that the microcirculation system in the skin is an important acceptor of the photobiostimulating effect of light in the blue range of the spectrum.

Photobiostimulation triggers the mechanism of activation of microcirculation by reducing myogenic vasomotion, thereby increasing the conductivity of cardiogenic biorhythm in the vessels of the microcirculatory bed and accelerating the movement of red blood cells from capillaries to the postcapillary link. The activation of tissue oxidative metabolism and the subsequent redistribution of interstitial fluid flows in the interstitial space are directly associated with an increase in the level of microcirculation during photobiostimulation.

Disclosures

The authors have no relevant financial interests in this article or potential conflicts of interest to disclose.

References

1. Technical group “Biomedical Optics”, International Optical Association (OPTICA) (accessed on 22 Mar 2023). [https://www.optica.org/en-us/get_involved/technical_groups/bmo/photobiomodulation_(bl)].
2. J. Moan, “Visible light and UV radiation,” Chapter 7 in Radiation at home, outdoors and in the workplace, D. Brune, R. Hellborg, B. Persson, and R. Pääkkönen (Eds.), Scandinavian Science Publisher, 69–85 (2001).
3. A. Cios, M. Ciepielak, Ł. Szyma´nski, A. Lewicka, S. Cierniak, W. Stankiewicz, Mendrycka, and S. Lewicki, “Effect of Different Wavelengths of Laser Irradiation on the Skin Cells,” International Journal of Molecular Sciences 22(5), 24–37 (2021).
4. F. N. J. De Alencar, C. F. W. Nonaka, and M. H. C. de Vasconcelos Catão, “Effect of blue LED on the healing process of third-degree skin burns: Clinical and histological evaluation,” Lasers in Medical Science 34, 721–728 (2019)
5. K. M. Al Ghamdi, A. Kumar, A. E. Ashour, and A. A. Al Ghamdi, “A comparative study of the effects of different low-level lasers on the proliferation, viability, and migration of human melanocytes in Vitro,” Lasers in Medical Science 30, 1541–1551 (2015)
6. I. Castellano-Pellicena, N. E. Uzunbajakava, C. Mignon, B. Raafs, V. A. Botchkarev, and M. J. Thornton, “Does blue light restore human epidermal barrier function via activation of opsin during cutaneous wound healing?” Lasers in Surgery and Medicine 51(4), 370–382 (2018)
7. V. I. Karandashov, E. B. Petukhov, and V. S. Zrodnikov, Phototherapy (light therapy): A Guide for Physicians, N. R. Paleev (Ed.), Medicine, Moscow (2001). [in Russian].
8. N. D. Sorokina, G. V. Selitsky, and E. S. Ilyina, “Neurobiological aspects of photochromotherapy,” Russian Medical Journal 23(1), 46–51 (2017). [in Russian].
9. V. I. Karandashov, “Peculiarities of optic irradiation in the blue range of spectrum and perspectives of its application in practical medicine,” Laser Medicine 17(2), 49–55 (2013). [in Russian].
10. V. I. Kozlov, Capillaroscopy in clinical practice, Prakticheskaya medicina, Moscow (2015). ISBN: 978-5-9881-342-3. [in Russian].
11. V. V. Astashov, V. I. Kozlov, V. V. Sidorov, A. A. Lomshakov, M. V. Uloga, O. A. Zayko, and V. P.Rozhkova, “The state of hemo- and lymphomicrocirculation under normal hemodynamic conditions and in circulatory hypoxia,” Laser Medicine 22(2), 25–28 (2018). [in Russian].
12. A. I. Krupatkin, V. V. Sidorov, Functional diagnostics of the state of microcirculatory tissue systems. Fluctuations, information, non-linearity. Guide for Physicians, 2nd ed., URSS, Moscow (2016). ISBN 978-5-9710-3329-5 [in Russian].
13. V. V. Sidorov, Yu. L. Rybakov, V. M. Gukasov, and G. S. Evtushenko, “A Device for Comprehensive Noninvasive Diagnostics of the Tissue Microcirculation System of Human Skin,” Biomedical Engineering 55(4), 232–235 (2021).
14. A. A. Heikal, “Intracellular coenzymes as natural biomarkers for metabolic activities and mitochondrial anomalies,” Biomarkers in Medicine 4(2), 241–263 (2010).
15. S. V. Moskvin, T. V. Konchugova, and A. A. Khadartsev, “The commonest therapeutic methods for laser irradiation of blood,” Voprosy kurortologii, fizioterapii, i lechebnoi fizicheskoi kultury 94(5), 10–17 (2017). [in Russian].

16. I. Kozlov, V. N. Sakharov, O. A. Gurova, and V. V. Sidorov, "Laser doppler flowmetry assessment of microcirculation in children of 6–7 years old. Regional blood circulation and microcirculation," Regional blood circulation and microcirculation 20(3), 46–53 (2021). [in Russian].
17. M. Intaglietta, "Vasomotion and flowmotion: physiological mechanisms and clinical evidence," Vascular Medicine Review 1, 101–112 (1990).
18. A. R. Pries, T. W. Secomb, "Blood flow in microvascular networks," Chapter 1 in Microcirculation, R. F. Tuma, W. N. Duran, and R. Ley (Eds.), 2nd ed., Academic Press, Amsterdam-Tokyo, 3–36 (2008). ISBN: 978-0-12-374530-9.
19. X. Luo, R. Li, and L.-J. Yan, "Roles of Pyruvate, NADH, and Mitochondrial Complex I in Redox Balance and Imbalance in β Cell Function and Dysfunction," Journal Diabetes Research 2015, 512618 (2015).
20. K. A. Sveshnikov, N. S. Ruseykin, "Lymph velocity conduction in intact and damaged extremity," Modern problems of Science and Education 2, 22–28 (2008). [in Russian].
21. A. A. Egorova, E. A. Avramenko, "Experimental faecal peritonitis alters response to 5-hydroxytryptamine in mesenteric lymphatic vessels," Fundamental and Clinical Medicine 5(3), 35–41 (2020). [in Russian].
22. T. X. Phan, B. Jaruga, S. C. Pingle, B. C. Bandyopadhyay, and G. P. Ahern, "Intrinsic Photosensitivity Enhances Motility of T Lymphocytes," Scientific Reports 6, 39479 (2016).
23. P. I. Guzalov, V.V. Kir'yanova, A. S. Nikishchenkova, and Ts. Yuibo, "The application of photodiode radiation of different wavelengths for the treatment of the acute phase of compressive-ischemic neuropathy of the facial nerve," Russian Journal of the Physical Therapy, Balneotherapy and Rehabilitation 4, 18–23 (2012). [in Russian].
24. L. Gavish, O. Hoffer, N. Rabin, M. Halak, S. Shkilevich, Y. Shayovitz, G. Weizman, O. Haim, B. Gavish, S. D. Gertz, and Z. Ovadia-Blechman, "Microcirculatory Response to Photobiomodulation-Why Some Respond and Others Do Not: A Randomized Controlled Study," Lasers in Surgery and Medicine 52(9), 863–872 (2020).
25. M. M. Lukina, M. V. Shirmanova, T. F. Sergeeva, and E. V. Zagaynova, "Metabolical imaging in the study of oncological processes (review)," Sovremennye Tehnologii v Medicine 8(4), 113–121 (2016).
26. F. J. Corpas, J. B. Barroso, "NADPH-generating dehydrogenases: their role in the mechanism of protection against nitro-oxidative stress induced by adverse environmental conditions," Frontiers in Environmental Science 2, 1–5 (2014).